

1-1-2016

Synthesis and Characterization of Ferrous Nanoparticles and Polymer-Grafted Ferrous Nanoparticles with an Examination of Thermal and Magnetic Properties

Swati Kumari

Follow this and additional works at: <https://scholarsjunction.msstate.edu/td>

Recommended Citation

Kumari, Swati, "Synthesis and Characterization of Ferrous Nanoparticles and Polymer-Grafted Ferrous Nanoparticles with an Examination of Thermal and Magnetic Properties" (2016). *Theses and Dissertations*. 4183.

<https://scholarsjunction.msstate.edu/td/4183>

This Graduate Thesis - Open Access is brought to you for free and open access by the Theses and Dissertations at Scholars Junction. It has been accepted for inclusion in Theses and Dissertations by an authorized administrator of Scholars Junction. For more information, please contact scholcomm@msstate.libanswers.com.

Synthesis and characterization of ferrous nanoparticles and polymer-grafted ferrous nanoparticles with an examination of thermal and magnetic properties

By

Swati Kumari

A Thesis
Submitted to the Faculty of
Mississippi State University
in Partial Fulfillment of the Requirements
for the Degree of Master of Science
in Chemical Engineering
in the Dave C. Swalm School of Chemical Engineering

Mississippi State, Mississippi

August 2016

Copyright by

Swati Kumari

2016

Synthesis and characterization of ferrous nanoparticles and polymer-grafted ferrous nanoparticles with an examination of thermal and magnetic properties

By

Swati Kumari

Approved:

Keisha B. Walters
(Major Professor)

Mohammad Sepehrifar
(Minor Professor)

Santanu Kundu
(Committee Member)

Billy B. Elmore
(Committee Member)

W. Todd French
(Graduate Coordinator)

Jason M. Keith
Dean
Bagley College of Engineering

Name: Swati Kumari

Date of Degree: August 12, 2016

Institution: Mississippi State University

Major Field: Chemical Engineering

Director of Thesis: Dr. Keisha B. Walters

Title of Study: Synthesis and characterization of ferrous nanoparticles and polymer-grafted ferrous nanoparticles with an examination of thermal and magnetic properties

Pages in Study 131

Candidate for Degree of Master of Science

Energy harvesting using ferrofluid in OHP. Characterization of as-synthesized (bare) and surface-modified ferrofluid samples was performed using Fourier transform infrared spectroscopy, dynamic light scattering, X-ray powder diffraction, transmission electron microscopy, and atomic force microscopy. These ferrofluids were tested in a novel oscillating heat pipe set-up was utilized to harvest electricity, demonstrating the concept of ferrofluidic induction. Cobalt-ferrite nanoparticles surface-modified with citric acid demonstrated good magnetic strengths and generated voltages close to those of the as-synthesized ferrofluids while maintaining dispersion.

Surface modification of ferrous nanoparticles with SRP. Thermo responsive polymer poly(N-isopropylacrylamide) was successfully grown from the surface of cobalt-zinc ferrite nanoparticles. A dual responsive block copolymer, pH and thermo responsive comprised of poly(itaconic) acid and poly(N-isopropylacrylamide) was successfully polymerized from the surface of ferrous oxide nanoparticles. These composite having

magnetic properties along with stimulus can be used in applications such as controlled drug delivery and similar biomedical applications.

TABLE OF CONTENTS

LIST OF TABLES	v
LIST OF FIGURES	vi
CHAPTER	
I. INTRODUCTION	1
1.1 Nanotechnology	1
1.2 Ferrofluids	3
1.3 Oscillating Heat Pipe	4
1.4 Stimuli-responsive polymer: An overview	4
1.5 Surface-modification of magnetic nanoparticles for drug delivery applications	6
1.6 Research	7
II. NOVEL ENERGY HARVESTING METHOD BY USING FERROFLUID AS THE WORKING FLUID IN OSCILLATING HEAT PIPES	9
2.1 Abstract	9
2.2 Introduction	10
2.3 Experimental Section	14
2.3.1 Materials	14
2.3.2 Synthesis of cobalt-ferrite (CoFe ₂ O ₄) nanoparticles	14
2.3.3 Surface modification of cobalt-ferrite nanoparticles with stabilizing ligands	15
2.3.4 Characterization	17
2.4 Results and Discussion	18
2.4.1 Need for Surface Modification of MNPs	30
2.5 Conclusions	40
2.6 Future Efforts	41
III. SYNTHESIS AND CHARACTERIZATION OF COBALT ZINC FERRITE NANOCOMPOSITES	42
3.1 Abstract	42
3.2 Introduction	42
3.3 Experimental Section	51

3.3.1	Materials	51
3.3.2	Synthesis of bare cobalt zinc ferrite (CZF) nanoparticles	51
3.3.3	Synthesis of cobalt zinc ferrite (CZF) nanoparticles coated with APTES	52
3.3.4	SI-ATRP polymerization of NIPAM on APTES coated cobalt zinc ferrite nanoparticles	53
3.3.5	Characterization	53
3.4	Results and Discussion	55
3.5	Conclusions	61
IV. SYNTHESIS AND CHARACTERIZATION OF TEMPERATURE AND PH RESPONSIVE NANOCOMPOSITES PIA-b-PNIPAM@Fe ₃ O ₄		
4.1	Abstract	63
4.2	Introduction	64
4.3	Experimental Section	65
4.3.1	Synthesis of APTES modified magnetic nanoparticles	65
4.3.2	Surface-initiated block copolymerization of itaconic acid (IA) and N-isopropylacrylamide (NIPAM)	66
4.4	Characterization	67
4.5	Results and Discussion	68
4.6	Conclusions	71
V. STUDY THE PARTICLE BREAKAGE OF MOSAIC NANOPARTICLES		
5.1	Abstract	73
5.2	Experimental Section	76
5.2.1	Materials	76
5.2.2	Thermal fracture of magnetic nanoparticles with different coatings	76
5.2.3	Characterization	76
5.3	Results and Discussion	77
5.4	Conclusions	81
VI. CONCLUSIONS		
REFERENCES		86
APPENDIX		
A. PROCEDURE AND METHODS UTILIZED FOR CHARACTERIZATION		
A.1	MIRacle-ATR FTIR procedure	112
A.1.1	Clearing water from drip leg	112

A.1.2	Filling liquid nitrogen dewar on MCT detector	112
A.1.3	MIRacle-attenuated total reflectance - FTIR.....	113
A.2	Simultaneous thermogravimetric analysis and differential scanning calorimetry (SDT)	116
A.3	Modulated differential scanning calorimetry (DSC).....	117
A.4	X-Ray photoelectron spectroscopy (XPS).....	119
A.4.1	Sample preparation.....	119
A.4.2	Sample loading into XPS main chamber.....	119
A.4.3	Starting the X-ray source.....	121
A.5	Freeze-pump-thaw	124
A.6	Differential scanning calorimetry (DSC)	125
A.7	Procedure to run <i>in-situ</i> AFM measurements.....	125
A.7.1	Summary.....	125
A.7.1.1	Procedure.....	126
A.7.1.1.1	Equipment startup	126
A.7.1.1.2	Experimental setup.....	126

LIST OF TABLES

2.1	Comparison of average particle diameter for FF-bare and those modified by different ligands.	31
-----	---	----

LIST OF FIGURES

2.1	Schematic showing general OHP experimental setup (Attributed to Gabe Monroe).....	13
2.2	Synthesis of cobalt-ferric (CoFe_2O_4) nanoparticles.	15
2.3	Capping agents used to surface modify cobalt-ferrite nanoparticles.....	16
2.4	Experimental set up of peristaltic pump.....	19
2.5	Measure of electrical energy using ferrofluid with capping agents in OHP	20
2.6	Dimensions of investigated FF-OHP with evaporator, condenser, thermocouples, and harvester locations.....	21
2.7	Representative XRD spectrum of FF-bare nanoparticles.....	22
2.8	FTIR spectra of pre-OHP FF-bare (a) and post-OHP FF-bare (b)	22
2.9	FTIR spectra of FF-bare (a), FF-CIT pre-OHP (b), FF-CIT post-OHP (c) and neat citric acid (d).....	24
2.10	FTIR spectra of FF-bare (a), FF-GLY (b), and neat glycerol (c).....	25
2.11	FTIR spectra of FF-bare (a), FF-OA (b), and neat oleic acid (c).....	26
2.12	FTIR spectra of FF-bare (a), FF-OXA (b), and neat oxalic acid (c).....	27
2.13	FTIR spectra of FF-bare (a), FF-PEG (b), and neat PEG (c).....	28
2.14	FTIR spectra of FF-bare (a), FF-SDS (b), and neat SDS (c).....	29
2.15	FTIR spectra of FF-bare (a), FF-PCA (b), and neat perchloric acid.....	30
2.16	TEM (A), AFM topography (B), MFM phase (C), and AFM phase (D) images for FF-bare.....	33
2.17	TEM (A), AFM topography (B), MFM phase (C), and AFM phase (D) images for FF-CIT	34

2.18	TEM (A), AFM topography (B), MFM phase (C), and AFM phase (D) images for FF-OA	35
2.19	TEM (A), AFM topography (B), MFM phase (C), and AFM phase (D) images for FF-OXA	36
2.20	TEM (A), AFM topography (B), MFM phase (C), and AFM phase (D) images for FF-PCA	37
2.21	TEM (A), AFM topography (B), MFM phase (C), and AFM phase (D) images for FF-PEG	38
2.22	TEM (A), AFM topography (B), MFM phase (C), and AFM phase (D) images for FF-SDS	39
2.23	TEM (A), AFM topography (B), MFM phase (C), and AFM phase (D) images for FF-GLY	40
3.1	Nanomaterial-based strategies for tumor diagnosis, imaging and therapy. ²⁰⁵	44
3.2	Two different lattice sites in magnetite ²²⁸	47
3.3	Schematic depicting a microgel particle in a poor (a) and good (b) solvent, respectively.	49
3.4	Experimental schematic for CZF synthesis	52
3.5	Surface modification of CZF nanoparticle to CZF-APTES	52
3.6	Polymerization of PNIPAM from the surface of CZF-APTES	53
3.7	XRD pattern for CZF (bare) particles	56
3.8	FTIR pattern for CZF (a), CZF-APTES (b), and CZF-APTES@PNIPAM (c)	57
3.9	TEM (A), AFM topography (B), MFM phase (C), and AFM phase (D) images for neat (bare) cobalt zinc ferrite nanoparticles	58
3.10	TEM (A), AFM topography (B), MFM phase (C), and AFM phase (D) images for CZF-APTES	59
3.11	TEM (A), AFM topography (B), MFM phase (C), and AFM phase (D) images for CZF-APTES@PNIPAM	60
3.12	Hydrodynamic diameter temperature dependence of CZF-APTES and CZF-APTES@PNIPAM nanoparticles.	61

4.1	Representative FTIR spectra of APTES@Fe ₃ O ₄ nanoparticles (blue spectrum) and PIA- <i>b</i> -PNIPAM@Fe ₃ O ₄ (red spectrum)	69
4.2	TEM image of Fe ₃ O ₄ @APTES (a), Fe ₃ O ₄ @PIA (b) and Fe ₃ O ₄ @PIA- <i>b</i> -PNIPAM (c,d)	70
4.3	Effective diameter temperature and pH dependence of the Fe ₃ O ₄ @PIA- <i>b</i> -PNIPAM stimuli responsive polymer	71
5.1	Mean diameter shift in amine and chitosan at sub -130 °C.....	78
5.2	Shift in in mean diameter for amine at ≈100 °C. Line represents the corresponding mean effective diameter with shaded band as error with 95% confidence.	79
5.3	Shift in heat flow through amine at ≈107 °C.....	80
5.4	TEM image showing particle aggregation	81
A.1	AFM Icon instrument front view.....	126
A.2	Beam alignment while <i>in-situ</i> measurements are conducted	128

CHAPTER I

INTRODUCTION

1.1 Nanotechnology

Following the vision of the famous physicist Richard Feynman in 1960s and his statement that "(t)here's plenty room at the bottom",¹ a dramatic increase in research of materials at very small length scales, e.g. nanoparticles, has occurred. Nanoparticle synthesis, properties, and applications are broadly investigated on an ever-increasing level, with their applications ranging from health, environment and improvement in quality of life,^{2,3} so much, so that it has revolutionized the biomedical and drug industries.^{2,4}

Nanoparticles can be broadly classified into several major types *viz.* metallic and non-metallic.^{5,6} Nanoparticles have been used for commercial products such as sunscreen lotions, cosmetics, and pharmaceuticals,⁷⁻¹⁴ medical treatment (e.g., magnetic nanoparticles for MRI imaging), catalysis,¹⁵ real-time photoacoustic imaging,¹⁶ oil remediation¹⁷ and waste water treatment.¹⁸ Based on their size scale and large surface area to volume ratio, nanoparticles have been examined as carriers—or vehicles—for a plethora of materials.^{19,20}

Nanoparticles consisting of cores made of iron oxides, etc. are magnetic nanoparticles that can be controlled and targeted to a specific area using magnetic field.²¹ Grafting of a biocompatible polymer from nanoparticles can provide benefits in terms of

shielding from the surrounding environment and functionality by attaching carboxyl groups, biotin, avidin, carbodiimide and other polymer molecule.²²⁻²⁴ These magnetic nanocomposites have major advantages over the normal, non-targeted drug delivery systems including reduction of the associated side effects and the drug dosage. Therefore, addition of polymers on the surface of nanoparticle can enhance its functionality by making it less susceptible to environment.^{25, 26}

Besides providing immunity to the nanoparticles from the surrounding, it can be made target specific by using stimuli responsive polymer (SRP). Stimuli responsiveness is another interesting property of nanocomposites that allows them to respond to changes in environment like pH, temperature, stress and, to applied electric and magnetic field. Moreover, these properties can be tuned by controlling the experimental variable like size, shape, composition and corresponding volume fractions that lead to desirable properties.²⁷ SRPs synthesized at the nano-scale level are called polymersomes.²⁸ However, when polymerized from or attached to the surface of a metal nanoparticle, a hybrid polymer-metal nanocomposites forms with combined properties of its constituents are useful in applications such as prevention of metal corrosion,^{29,30} self-healing materials,³¹⁻³³ and robotic applications.^{24, 25}

Even though nanoparticles and their application have shown tremendous promise, there is some call for caution. The design, utilization, and disposal of nano-scale materials should be carefully considered, as the long-term effects on physiology and environment are still not well understood.^{30, 31} There is an incredible potential to design nano-scale materials, in order to greatly expand fields of study and revolutionize current biomedical and drug industries.

1.2 Ferrofluids

Ferrofluids are comprised of subdomain particles of magnetite or iron oxide material that can become magnetized in the presence of a magnetic field. These unique liquids are being incorporated into many new applications due to the ability to control them at a distance using magnetic fields. Moreover, ferrofluids demonstrate outstanding properties compared to micrometer-sized particles or millimeter-sized particles when it comes to heat transfer since the heat transfer happens on the surface of the particle and since nanoparticles have a large total surface area.³⁸

Ferrofluids consist of a liquid in which particles, often nanoscale in size, are indefinitely suspended with the solvent due to their surface functional groups interacting with it and, their Brownian motion and generally will not settle under standard conditions.³⁹⁻⁴¹ These particles are highly susceptible to magnetic fields, and become magnetized while remaining suspended in their liquid carrier.

Ferrofluidic induction is the process of creating electromagnetic induction by the relative motion of a solenoid and ferrous nanoparticles suspended in a carrier fluid (*i.e.* ferrofluid). The source of ferrofluid motion can vary, but a static bias magnetic field is required to temporarily 'magnetize' the ferrofluid.⁴² Sansom et al. utilized three Fe₃O₄-based ferrofluids with different viscosities and saturation magnetizations. They examined thermo-electric conversion by pumping the fluids through a tube in proximity to an induction coil and a neodymium bias magnet. In this study, ferrofluids were examined as the working fluid and utilized in an oscillating heat pipe (OHP) for energy harvesting purpose. And, it has been shown that the thermal performance and effective thermal conductivity was improved by using ferrofluids instead of water.

1.3 Oscillating Heat Pipe

Conventionally used for longitudinal heat transfer, oscillating heat pipes (OHP) have demonstrated thermal spreading potential.^{23, 24} The serpentine channel structure made from machining bent tubes into flat plate OHP connects heat source (OHP evaporator) and heat sink (OHP condenser) on either ends.^{45, 46} Those complex channel structures can also be produced using modified geometry of channels.^{24, 25} The flat plate OHP's contain capillary sized channels sealed with a cover plate. Creation of vacuum followed by partial filling of working fluid and hermetically sealing is done before OHP operation. A critical temperature difference necessary for initiation and sustaining fluid motion also assures vapor growth due to latent heat transfer.⁴⁸⁻⁵⁰ Non-uniform evaporation causes non-equilibrium pressure field in the OHP evaporator leading to fluid pulsation between the evaporator and condenser. Fluid oscillations less than 20 Hz results in cyclic mechanism favoring high heat transport capability.²⁹⁻³¹ Both latent and sensible heat transfer play a major role in OHP operation. The former one being the driving force and latter accounts for major share of total heat transfer between evaporator and condenser.^{32, 33}

1.4 Stimuli-responsive polymer: An overview

Polymers that respond to external conditions such as light, temperature, pH, ionic strength, mechanical deformations, etc. are known as stimuli responsive polymers (SRP).⁵⁶⁻⁵⁸ They were first studied in the 1980's in the form of PNIPAM gels.^{59, 60} The variables like transition in volume phase, pH responsiveness and temperature changes are explained as a result of interplay between hydrophobic and hydrophilic interactions at the

molecular level.⁶⁰⁻⁶² Other forms of SRPs are block-*co*-polymers in solutions, surface tethered SRPs and cross-linked gels.⁶³⁻⁶⁷

SRPs have been successfully used in a variety of applications such as drug delivery,^{68,69} self-healing materials,^{70,71} cell adhesion,^{72,73} sensors^{74,75} and releasing of encapsulated materials.^{70,71} One such application of SRPs is as an adjunct to the field of nanotechnology. SRPs can be used in combination with nanoparticles for cellular/organ targeting, diagnostics, and delivery vehicles in biological systems due to their size being compatible with cellular uptake, controlled manipulation within and removal from the body, and tunable responsiveness to physical conditions.^{17,50} A large variety of SRPs have been synthesized, characterized, and demonstrated to be responsive to different external triggers.⁷⁹⁻⁸¹ The most common stimuli studied with regards to SRPs are pH and temperature due to their usefulness in triggering the release of drugs from the carrier.⁸²⁻⁸⁴

Thus, SRPs combined with nanoparticles is a promising class of materials. The size can be tailored, multiple functionalities included in the nanocomposite design, the bulk and surface chemistries controlled, aggregation, the stimuli-trigger conditions manipulated, and particle aggregation controlled as well. Due to the vast literature in this subject area, each chapter will include references for the particular SRPs examined, the surface modification methods used for the nanoparticles and/or flat substrates, and prior efforts from the literature, along with the related discussion. Peculiar responses to pH and/or temperature will also be discussed in conjunction with previous findings for the stimuli responsive polymer examined in each chapter of this work.

SRP-grafted-NPs have been examined for a wide range of applications. One highly promising field for these nano-scale materials with tailored chemistries and stimuli

responsive behavior is biomedicine. The stimuli responsive mimics the response of body, such as selective membrane transport,⁸⁵ strain-stiffening,⁸⁶⁻⁸⁸ pH responsiveness,⁸⁹ light sensitiveness⁹⁰ and thermal response.⁹¹⁻⁹³ Furthermore, SRP-grafted-NPs the serves as a general platform to allow researchers to produce nano-scale materials with very controllable properties and the capability for drug delivery, selective uptake and release of a dopant, and site or concentration dependent drug release, binding or releasing using the stimulus.⁹⁴⁻⁹⁷

1.5 Surface-modification of magnetic nanoparticles for drug delivery applications

Nanoparticles, as documented earlier, are currently one of the most published topics for research. While many different inorganic and nanoparticles have been synthesized and characterized with an aim towards new drug delivery devices,⁹⁸⁻¹⁰⁰ few of the researchers did modify the surface of nanoparticles are modified in a controlled fashion with SRP.¹⁰¹⁻¹⁰⁴

Atom transfer radical polymerization (ATRP), a technique for the surface-modification of flat substrates, has also been used to “grow” polymer brushes from the surface of nanoparticles using different types of monomers such as methyl methacrylate,¹⁰⁵ acrylic acid,¹⁰⁶ ethylene glycol,¹⁰⁷ and styrene.¹⁰⁸ Essentially, plethora of literature is available for the surface modification of nanoparticles, to this author’s knowledge there is only few reports in the literature of homogeneous and heterogeneous SRPs covalently bonded coated on the surface of magnetic nanoparticles.¹⁰⁹⁻¹¹⁵ In ATRP systems, reversible termination is used to reduce the steady state concentration of growing radicals and suppress bimolecular radical termination reactions.¹¹⁶ Once a

radical is generated from a dormant initiator, it can either add monomer or deactivate by reacting with a metal complex to regenerate the dormant initiator and a metal in a lower oxidation state.¹¹⁷ The controlled nature of ATRP results from the equilibrium strongly favoring the dormant species.¹¹⁸ Surface initiated ATRP can be applied to nonplanar surfaces such as nanoparticles. In an early example, Huang, et al.¹¹⁹ used ATRP to grow polyacrylamide brushes from n silica gel, and obtained a ~10 nm thick film after 40 hours at 130 °C. Husseman et al.¹²⁰ improved control over the growth of polymer brushes by adding a sacrificial initiator to decrease the concentration of active chains, and therefore reduced chain termination by coupling and disproportionation. Therefore, one of the objectives of this work is to evaluate the synthesis of pH- and thermo-responsive polymers from the surface of magnetic nanoparticles using ATRP.

1.6 Research

In Chapter 2, the goal is to energy harvesting method by using ferrofluid in oscillating heat pipes. Pulsating or cyclic oscillating flow of ferrofluids through a solenoid placed between two magnets was utilized to generate electric power, thereby demonstrating the concept of ferrofluidic induction. To avoid the aggregation of the nanoparticles in the ferrofluid over a long usage periods and through thermal cycling, a variety of ligands were used to modify the nanoparticle surface.

In Chapter 3, the overall goal is to synthesize superparamagnetic cobalt-zinc ferrite (CZF) nanoparticles from aqueous metal salt solutions by co-precipitation using ATRP to grow well-defined polymers from substrates. The research objectives include the synthesis and characterization of various thermo-responsiveness of the

nanocomposites. First, chemical analysis is performed to confirm whether polymerizations are successful or not, and then, the response ability is examined.

In Chapter 4, the synthesis and characterization of homopolymer and block copolymer structures containing N-isopropylacrylamide (NIPAM), itaconic acid (IA), are described. Chemical, physical, and thermal analyses of the bulk block copolymers by FTIR, DLS, and TEM are discussed. The pH and thermo-responsiveness of the modified MNPs is shown.

Chapter 5 attempts to summarize the experiments to impose thermal fatigue were performed, such as reflux heating, hydrothermal heating, modulated differential scanning calorimetry (MDSC), and thermogravimetric analysis (TGA). Conditions yielding particle breakage were recorded for each thermal treatment, and these findings were supported by further testing with dynamic light scattering (DLS) and transmission electron microscopy.

CHAPTER II

NOVEL ENERGY HARVESTING METHOD BY USING FERROFLUID AS THE WORKING FLUID IN OSCILLATING HEAT PIPES

2.1 Abstract

Ferrofluids comprised of ferrous oxide and ferrous cobalt oxide nanoparticles were synthesized and then surface functionalized to achieve stable nanoparticle suspensions while maintaining effective magnetization parameters. Cobalt-ferrite nanoparticles, suspended in water carrier as ferrofluids, were then evaluated as the working fluids in an oscillating heat pipe (OHP). This is done to achieve simultaneous enhanced passive heat transfer and to convert thermal energy to electrical energy. In this novel process, pulsating or cyclic oscillating flow of ferrofluids through a solenoid placed between two magnets was utilized to generate electric power, thereby demonstrating the concept of ferrofluidic induction. To avoid the aggregation of the nanoparticles in the ferrofluid over a long usage periods and through thermal cycling, a variety of ligands were used to modify the nanoparticle surface. Characterization of these samples were performed using ATR-FTIR, dynamic light scattering (DLS), X-ray diffraction (XRD), transmission electron microscopy (TEM), and atomic/magnetic force microscopy (AFM/MFM). Of the surface functionalized cobalt ferrite nanoparticles, those modified by citric acid demonstrated the highest magnetic strength and produced voltages close to

the neat ferrofluid (bare nanoparticles without surface modification) while maintaining dispersion—unlike the bare nanoparticles.

2.2 Introduction

Magnetic nanoparticles have attracted a lot of attention recently due to an increase in their use in wide-ranging applications including magnetic recording, microfluidic devices, bioreactors, storage, catalysis, biotechnology, and biomedical applications such as detection of viruses and toxins.^{121–124} Most commonly magnetic nanoparticles are comprised of iron oxide or magnetite. Magnetic nanoparticles less than 50 nm in diameter suspended in a liquid carrier is defined a ferrofluid. Application of external magnetic field alters the magnetic properties of ferrofluids. Depending upon the nature of the particle materials or the carrier liquids, ferrofluid can have a wide range of physical and magnetic properties. The particles are most commonly magnetite ($\text{FeO}\cdot\text{Fe}_2\text{O}_3$) or hematite ($\gamma\text{-Fe}_2\text{O}_3$). To enhance magnetic performance, alloying elements like Mn, Zn, or Co are included. Depending on the particular application, carrier liquids solvents can be water, mineral oil, organic solvents, etc.¹²⁵ It possess some properties like retention in a magnetic field, levitation of magnetic and non-magnetic objects, micro-magnetics and catalysis associated with small particles, magnetic shielding and effect on electrical parameters, that allows ferrofluid to be used in various engineering applications such as sealing, damping and heat transfer.^{126–130} Thermal agitation and Brownian motion cause the nanoparticles to be dispersed in the liquid carrier unless they aggregate, which leads to settling and ultimately precipitation. To avoid aggregation and settling, nanoparticles are surfaced modified with capping agents, ligands or surfactants which serve to increase the particle-solvent interactions and/or cause charge repulsion to prevent particle-particle

aggregation. The presence of an appropriate surface modifier helps maintain a spacing between the particles so that the attractive energy between adjacent particles is smaller than the disordering energy of their thermal motion, thereby providing colloidal stability.

^{125,131,132}

Ferrofluids can be synthesized via a number of different methods such as reduction in aqueous solution, reduction in reverse micelles, reduction of organometallic precursors with hydrogen under mild conditions, hydrothermal,¹³³ micro-emulsion,¹³⁴ forced hydrolysis, and co-precipitation.¹³⁵ Some drawbacks that occur with most of these methods are poor particle size distribution, particle aggregation, expense, toxicity, and low crystallinity, which restrict their use in certain applications.¹³⁶ In this study, ferrofluids were synthesized using the co-precipitation method due to its simplicity and productivity.¹³⁷⁻¹³⁹

Cobalt ferrite (CoFe_2O_4) was used as the magnetic material nanoparticle in this research due to its strong anisotropy, high coercivity at room temperature, moderate saturation magnetization,¹⁴⁰ and photo-magnetic materials.¹⁴¹⁻¹⁴⁴ CoFe_2O_4 has a wide range of established applications, such as electronics, photo-magnetism, catalysis, ferrofluid, hyperthermia,¹⁴⁵ cancer therapy, and molecular imaging agent in magnetic resonance imaging (MRI).¹⁴⁶⁻¹⁵⁰ While magnetite has been shown to have a slightly higher mass magnetization (magnetic moment per unit mass) of 101 emu/g versus 99 emu/g for cobalt ferrite, cobalt ferrite has the advantage of being more resistant to oxidation than magnetite.¹⁵¹⁻¹⁵³

Oscillating heat pipes (OHP) are dual phase (liquid-gas) heat transfer devices that operate passively and can be used for many different heat transfer applications—from

aerospace to ice cream scoops.^{154–157} OHPs are made using wicking channels that help to drive fluid movement along with a serpentine arrangement of the cylindrical or rectilinear channels that promotes temperature-actuated oscillating (or pulsating) flow.^{158–160} These channels can be made from pre-formed tubing or etched into a flat substrate. OHPs are evacuated and then partially filled with the working fluid. The ratio of OHP liquid volume to total internal volume is known as the filling ratio (ϕ_{FR}). The serpentine channel is designed so that the working fluid is exposed to the temperature source and sink axially, such that there is a temperature difference along the OHP length (Figure 2.1). This design results in vapor expansion on the ‘source’ end with pseudo-harmonic displacement of internal vapors, and vapor condensation on the ‘sink’ end. Unlike traditional heat pipes, pseudo-harmonic displacement, vapor pressure and surface temperatures oscillations in OHPs refill the condensate allowing the cyclic process to continue without the need for a wick structure. Creation of liquid “slugs” and vapor “plugs” in saturated, non-equilibrium conditions by capillary action is one of the most important features of OHPs.¹⁶¹

Ferrofluidic induction has been utilized by researchers in the past for energy harvesting applications and waste heat removal.^{162–168} One novelty of the work presented is the use of oscillating heat pipes along with in-house synthesized ferrofluids. The experimental setup includes two bias magnets and a solenoid core made from copper to allow for voltage generation (Figure 2.1) on one leg of the serpentine tubing. The set-up parameters that could be adjusted include the magnet spacing, the fluid pulse frequency and the ferrofluid particle type, size and surface modification. (Note that the impact of changing the equipment set-up parameters is being examined experimentally and

computationally by two other doctoral graduate students in the research group (Gabe Monroe and Huiyu Wang, respectively). The use of temperature actuated pulsating flows in the OHP along with frequency optimization and electrical and thermal efficiencies enhances the energy harvesting.^{169,170} In order to examine the impact of particle type, size, and surface modification, the study presented in this chapter was performed to examine methods of maximizing the magnetic properties while maintaining dispersion of the ferrofluid nanoparticles. Seven different ligands were tested and the modified particles were characterized using a combination of analytical techniques.

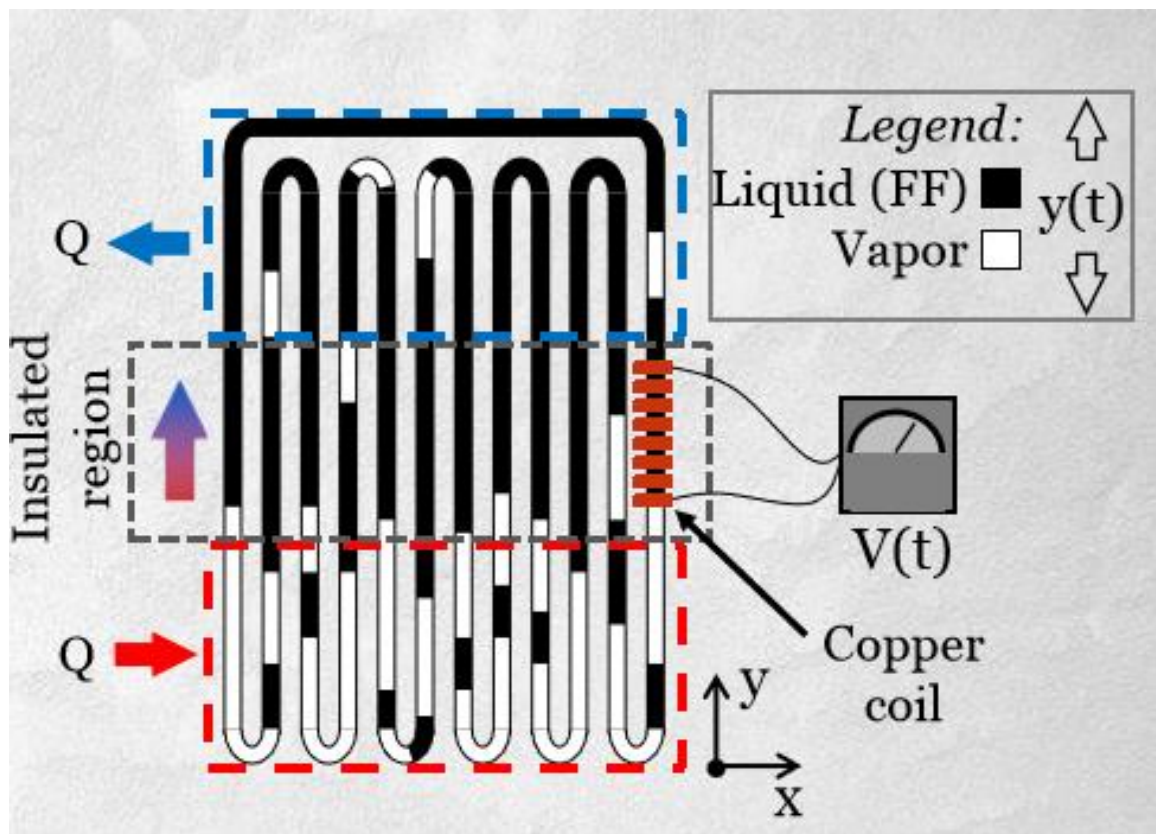


Figure 2.1 Schematic showing general OHP experimental setup (Attributed to Gabe Monroe)

2.3 Experimental Section

2.3.1 Materials

Cobalt-ferrite nanoparticles were synthesized in the Polymer and Surface Engineering Laboratories (PolySEL) at MSU (<http://www.polysel.che.msstate.edu>) using a co-precipitation method in alkaline medium. Iron (III) chloride hexahydrate [FeCl₃.6H₂O] (Sigma-Aldrich, CAS # 10025-77-1, 97%), cobalt (II) chloride hexahydrate [CoCl₂.6H₂O] (Sigma-Aldrich, CAS # 7791-13-1, 98%), sodium hydroxide (Sigma-Aldrich, ≥98%, pellets, anhydrous), oleic acid (Fluka Analytical, CAS # 112-80-1, ≥99%), poly(ethylene glycol) [PEG] solution (Sigma-Aldrich, CAS # 25322-68-3, 40 % (w/w) in H₂O, 8000 MW), perchloric acid (ACS reagent, CAS # 7601-90-3, 70%), citric acid (Sigma-Aldrich, CAS # 77-92-9, ≥99.5%), sodium dodecyl sulfate (Sigma-Aldrich, ≥98.5%), oxalic acid (Fischer, CAS # 6153-56-6, 126.07 MW, ≥99.5%) were used as-received without further purification. Water used in all experiments was purified using Millipore Q (Synergy & Synergy UV water purification system) which provides Type I water quality with a resistivity of 18.2 MΩ cm @ 25 °C.

2.3.2 Synthesis of cobalt-ferrite (CoFe₂O₄) nanoparticles

Solution containing 100 mL of 0.4 M FeCl₃.6H₂O and 100 mL of 0.4 M CoCl₂.6H₂O was added to 250 mL of 3M NaOH aqueous solution under rigorous stirring conditions (constant speed, mechanical stirrer) in a reaction vessel as shown in Figure 2.2. Temperature of the reaction was maintained at 80 °C under a nitrogen purge. Precipitation and suspension color change—from the initial brown color to dark brown—was noted immediately as the iron and cobalt chloride solution was added dropwise to the alkaline aqueous solution. This reaction was allowed to proceed for two hours after which

the nitrogen was cut off and solution was allowed to cool to room temperature. The ferrofluid was washed repeatedly by holding the cobalt-ferrite (CoFe_2O_4) nanoparticles to the side of the glassware with a 2T magnet, removing the solvent, releasing the nanoparticles, mixing in clean (deionized and filtered) water, and then repeating these washing steps a minimum of three times. The ‘washed’ samples were then dried at $80\text{ }^\circ\text{C}$ for 3 hours.^{171–174}

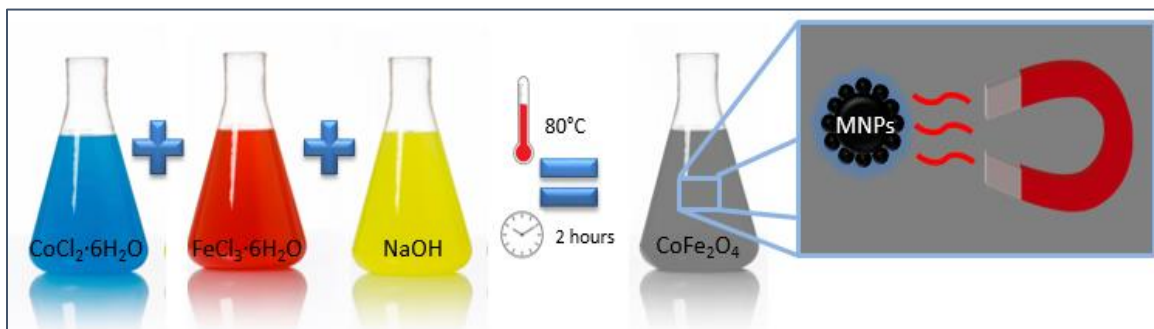
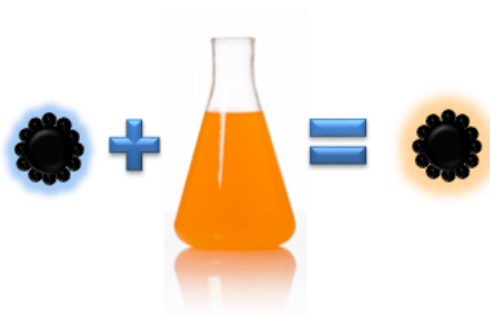


Figure 2.2 Synthesis of cobalt-ferrite (CoFe_2O_4) nanoparticles.

2.3.3 Surface modification of cobalt-ferrite nanoparticles with stabilizing ligands

After being dried, the bare (unmodified) cobalt-ferrite nanoparticle samples were modified with one of six different ligands (capping agents) to determine their effect on the magnetic characteristics and stability of the nanoparticle suspensions. Aqueous solution containing capping agent (50 mL, 0.1 M) was added to the nanoparticles and stirred for an hour using a magnetic stirrer. Then, the solution was washed three times (using deionized water and a 2T magnet to hold the magnetic nanoparticles (MNPs) in place) in order to remove excess (non-adsorbed) capping agent. Physical adsorption occurs quickly and, is often mono-molecular (unimolecular) layer or may be of 2-3 layers

thick (multi-molecular). As physical adsorption takes place on the pores of adsorbent, it begins as a monolayer. It can then become multi-layer, and then, if the pores are close to the size of the molecules, more adsorption occurs until the pores are filled with adsorbate.^{175,176} Accordingly, the maximum capacity of a porous adsorbent can be more related to the pore volume than to the surface area. In contrast, chemisorption involves the formation of chemical bonds between the adsorbate and adsorbent, and is typically a monolayer. It releases, comparatively higher heat energy, much larger than the heat of condensation of adsorbate. Most commercial adsorbents rely on physical adsorption; while catalysis relies on chemisorption. In the present work we used ligands that are chemically adsorbed via co-precipitation. Figure 2.3 shows the different capping agents (ligands) used.¹⁷⁷⁻¹⁷⁹



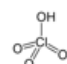

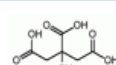
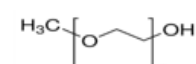
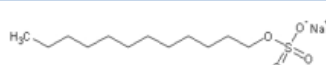
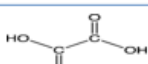
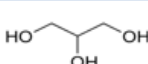
Capping Agents	Structure
Perchloric Acid	
Oleic Acid	
Citric Acid	
Poly(ethylene glycol)	
Sodium dodecyl sulfate	
Oxalic Acid	
Glycerol	

Figure 2.3 Capping agents used to surface modify cobalt-ferrite nanoparticles.

2.3.4 Characterization

Characterization of the neat (bare) and surface modified nanoparticles was performed using a number of different techniques: X-ray diffraction analysis (XRD), attenuated total reflection Fourier transform infrared spectroscopy (ATR-FTIR), dynamic light scattering (DLS), transmission electron microscopy (TEM), and magnetic force microscopy (MFM).

Structural characterization of the nanoparticles was performed by X-ray diffraction (XRD) using a Rigaku Ultima III X-ray diffractometer. Diffraction patterns were collected from the samples over a 2θ range of 10 to 80 degrees at ambient temperature.

ATR-FTIR (attenuated total reflection Fourier transform infrared) spectroscopy was used to confirm attachment of the capping agent. To perform this analysis, a Miracle-ATR accessory (Pike Technology) with a diamond-ZnSe crystal was used in a Nicolet 6700 FTIR spectrophotometer (Thermo Electron Corporation). The FTIR instrument was configured with a deuterated triglycine sulfate (DTGS) detector, KBr beamsplitter and a minimum of 256 scans were collected per sample. To prepare the samples, a droplet of the magnetic nanoparticle solution was placed on the crystal and the solvent allowed to evaporate yielding a thin film of nanoparticles on the crystal prior to scanning.

To measure particle sizes and particle size distributions, dynamic light scattering (DLS) analysis was performed using a ZetaPALS analyzer (Brookhaven Instruments Corporation) with a laser wavelength of 659 nm at an angle of 90 degrees and the Brookhaven software (v2.0). Sample preparation involved two steps, sonication for 2 minutes followed by stabilization in the cuvette for 3 minutes. A minimum of ten

measurements (5 minutes per measurement) were collected per sample in order to determine the mean particle diameter and 95% confidence interval.

A JEOL 2100 200 kV transmission electron microscope (TEM) was utilized to characterize the morphology and size of nanoparticles. Samples preparation included dispersion in DI water, sonication in ultrasonic bath for 5 minutes, and deposition on a carbon Formvar Cu grid (Electron Microscopy Science). Samples were then dried before imaging.

Atomic and magnetic force microscopy (AFM / MFM) were conducted on the nanoparticle samples using a Dimension Icon Veeco-Bruker operated in tapping mode and ScanAsyst model was used to collect data. Samples were prepared by drying overnight on the glass slides. MESP probes from Veeco (77.69 kHz resonant constant, 60 kHz drive frequency) were utilized with a 100 nm lift scan height for all measurements to be consistent. Images were collected at a minimum of three different spots for each samples to make sure collected images were consistent across the sample.

2.4 Results and Discussion

In previous study done by the PolySEL group for energy harvesting via ferrofluidic induction,¹⁸⁰ commercially available nanoparticles (FF-SPIE named for convention) were utilized. Though a measurable voltage was produced in a solenoid via circulated ferrofluid, it was also observed that the core-shell surrounding the mosaic nanopartilces broke which caused aggregation and eventually decreasing magnetization of the ferrofluid leading to lower energy harvesting. To avoid this, in-house ferrofluid was synthesized via co-precipitation. Still there was aggregation of bare cobalt-ferrite nanoparticles observed over the time as discussed later. In order to overcome these

different ligands were utilized so that the bare cobalt-ferrite nanoparticles tend to stay suspended in the carrier fluid and at the same time the motivation behind this work was to ensure as much energy as possible. Initially all the ferrofluids with different ligands were charged to a pump loop set up (Figure 2.4) to compare with the previous work¹⁸⁰ published. The pump loop set-up allows for the effect of the magnetic ferrofluid ‘slug’ on solenoid-based electrical energy generation to be evaluated without the simultaneous phase change that occurs in the OHP.

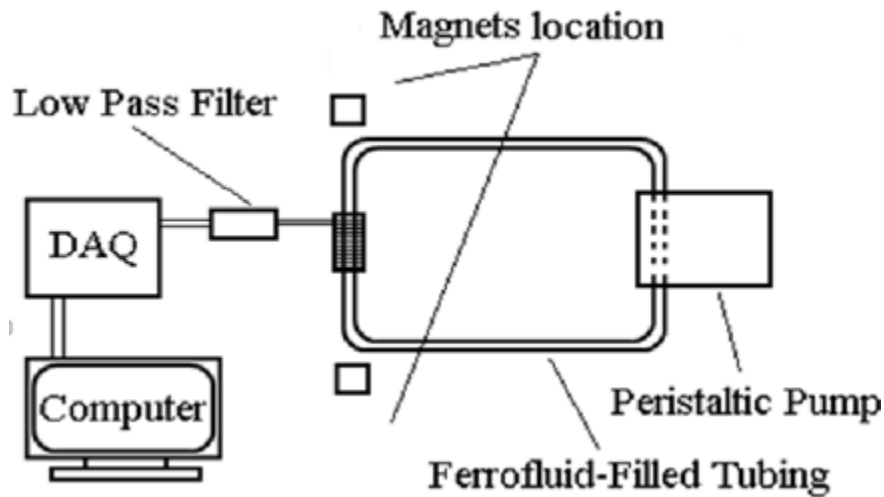


Figure 2.4 Experimental set up of peristaltic pump.

For consistency, bare neat (bare) CoFe_2O_4 ferrofluid have been named as FF-bare, citric acid coated CoFe_2O_4 as FF-CIT, perchloric acid coated CoFe_2O_4 as FF-PCA, oleic acid coated CoFe_2O_4 as FF-OA, oxalic acid coated CoFe_2O_4 as FF-OXA, poly(ethylene) glycol coated CoFe_2O_4 as FF-PEG, sodium dodecyl sulfate coated CoFe_2O_4 as FF-SDS and glycerol coated CoFe_2O_4 as FF-GLY. The test was run one time per MNP sample.

This initial investigation of the MNP magnetic properties allowed us to investigate which

ferrofluids gives higher maximum voltages. The preliminary result showed that the FF-bare generated 0.08 mV larger and FF-CIT generated 0.06 mV larger energy output than the FF-SPIE (0.03 mV) as shown in the Figure 2.5. Owing to higher energy output these were charged to OHP set up shown in Figure 2.6. In this section, characterization of all the seven ferrofluids with different surfactant has been discussed before charging to pump-loop set up. And, only FF-bare and FF-CIT has been characterized pre and post OHP set up to better understand the changes associated after cyclic oscillation of ferrofluids.

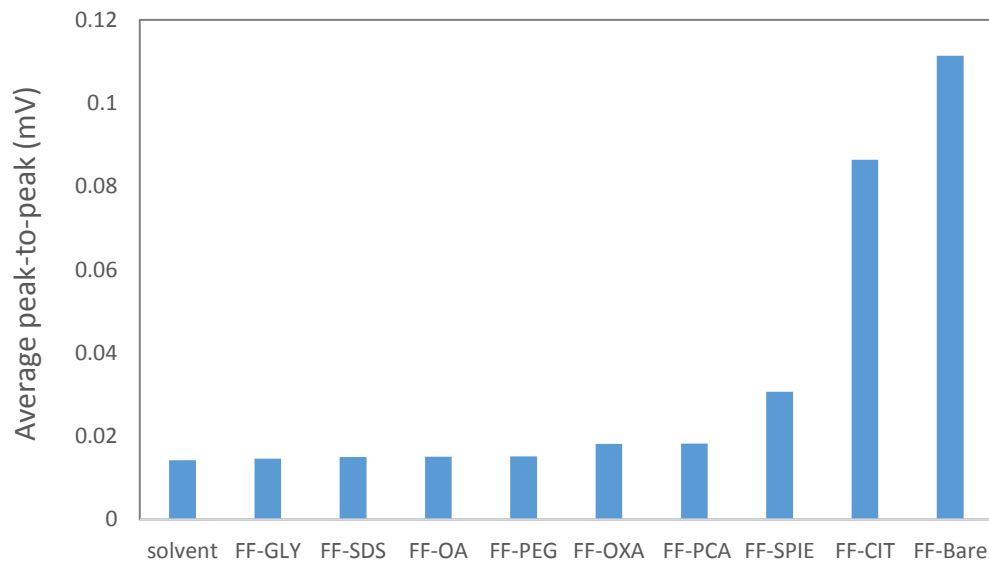


Figure 2.5 Measure of electrical energy using ferrofluid with capping agents in OHP

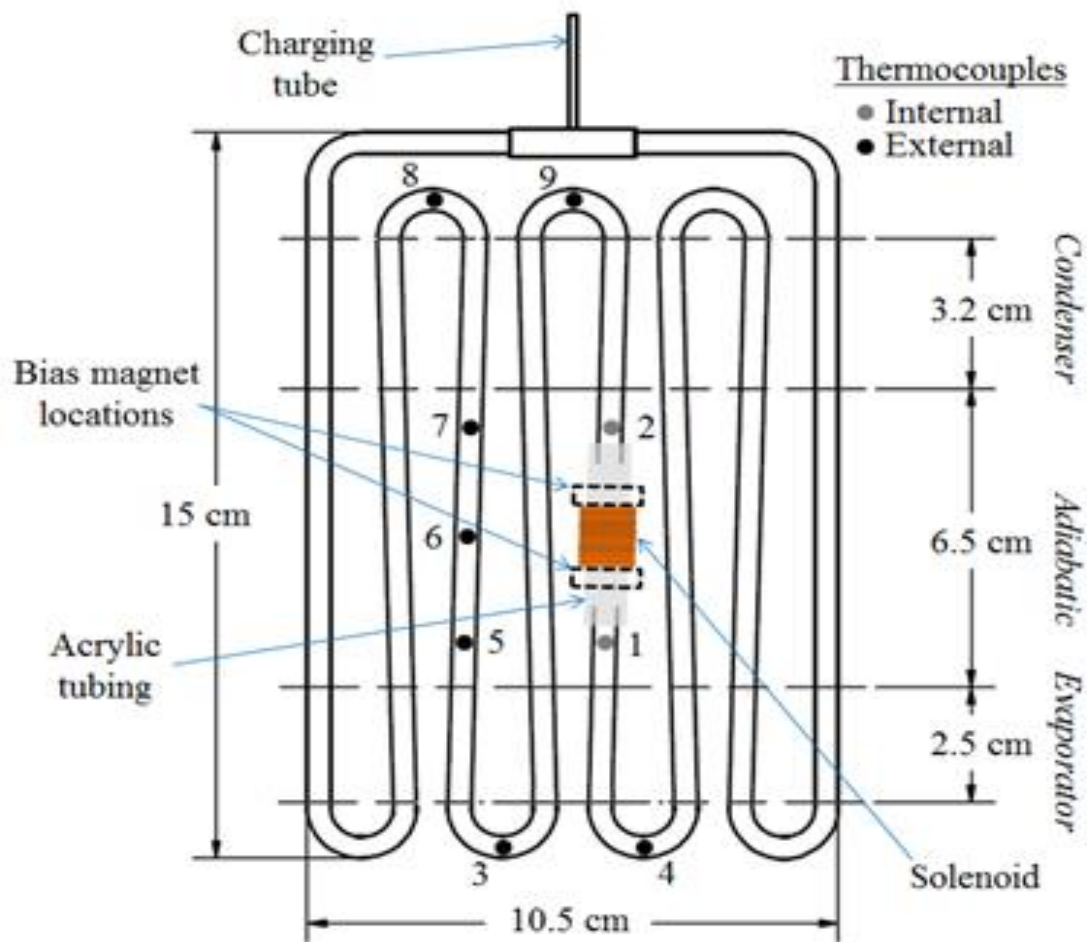


Figure 2.6 Dimensions of investigated FF-OHP with evaporator, condenser, thermocouples, and harvester locations

XRD patterns for the FF-bare was compared with the standard powder diffraction pattern for cubic CoFe_2O_4 (Joint Committee on Powder Diffraction Standards (JCPDS) Card No. 22-1086). The major peaks corresponding to (311), (400), (511), and (422) were identified and confirmed the presence of cobalt ferrite nanoparticles as shown in Figure 2.4.^{181,182} The sharp diffraction peaks and high intensity indicate the good crystallinity of the as-prepared CoFe_2O_4 sample. All samples exhibit similar diffraction peaks which correspond to the cubic inverse spinel type lattice of CoFe_2O_4 .¹⁴

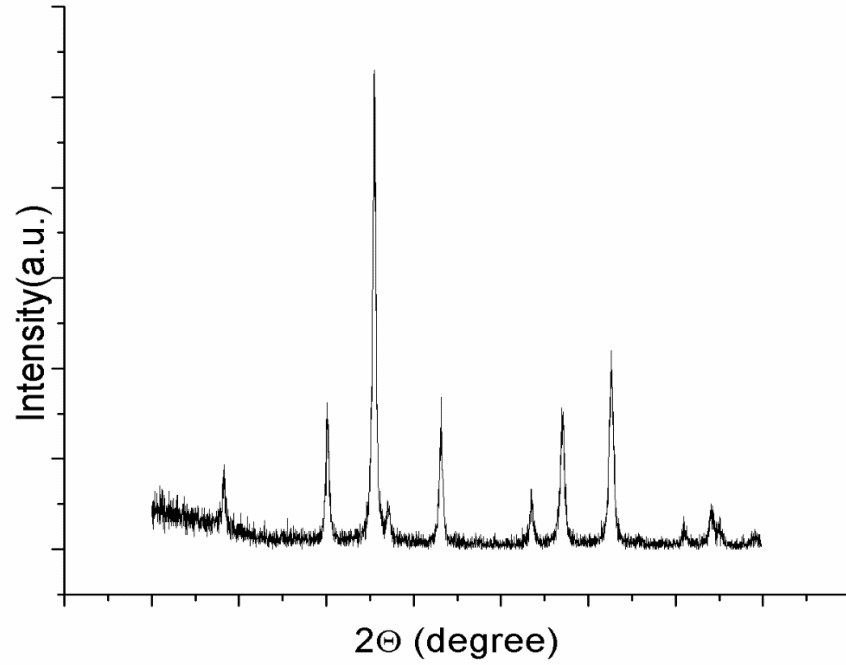


Figure 2.7 Representative XRD spectrum of FF-bare nanoparticles

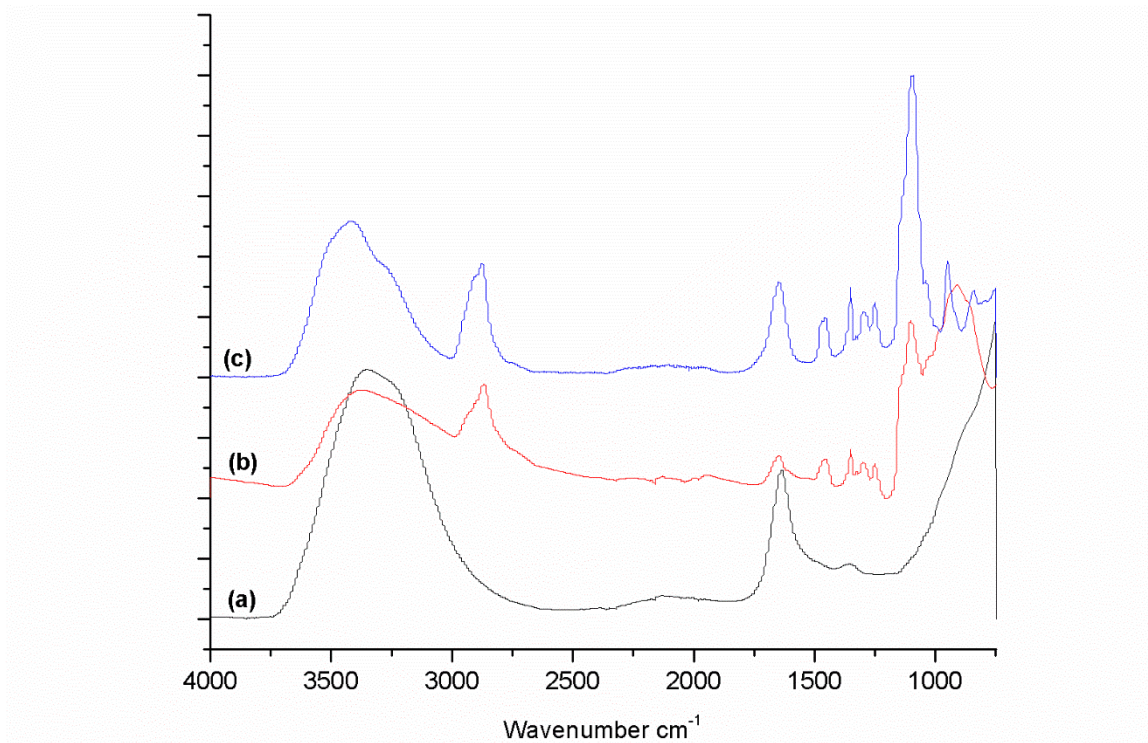


Figure 2.8 FTIR spectra of pre-OHP FF-bare (a) and post-OHP FF-bare (b)

FTIR spectra of pre and post OHP set up FF- bare is shown in the Figure 2.8. There is not much difference between the peaks suggesting no alteration in the functional groups attached to FF-bare. To confirm the presence of the surface modifiers on the FF-bare, FTIR spectra were collected. Figure 2.9 shows a representative FTIR spectra for FF-bare, FF-CIT and citric acid (neat). The absorption bands for pure CA are resolved, but those of the MNP-CA are broad and few. An intense band at 3348 cm^{-1} proposes the presence of nondissociated OH groups of citric acid. The peak at 1656 cm^{-1} may be assigned to the symmetric stretching of OH from COOH group, displaying the binding of a citric acid radical to the magnetic surface. The 1755 cm^{-1} peak of CA, attributable to the C=O vibration from the COOH group of CA. This peak shifts to an intense band at about 1656 cm^{-1} for FF-CIT, displaying the binding of a CA radical to the surface of CoFe_2O_4 nanoparticles by chemisorption of carboxylate (citrate) ions.¹⁸³ Carboxylate groups of CIT form complexes with Fe atoms on the surface representing partial single bond character to the C=O bond.

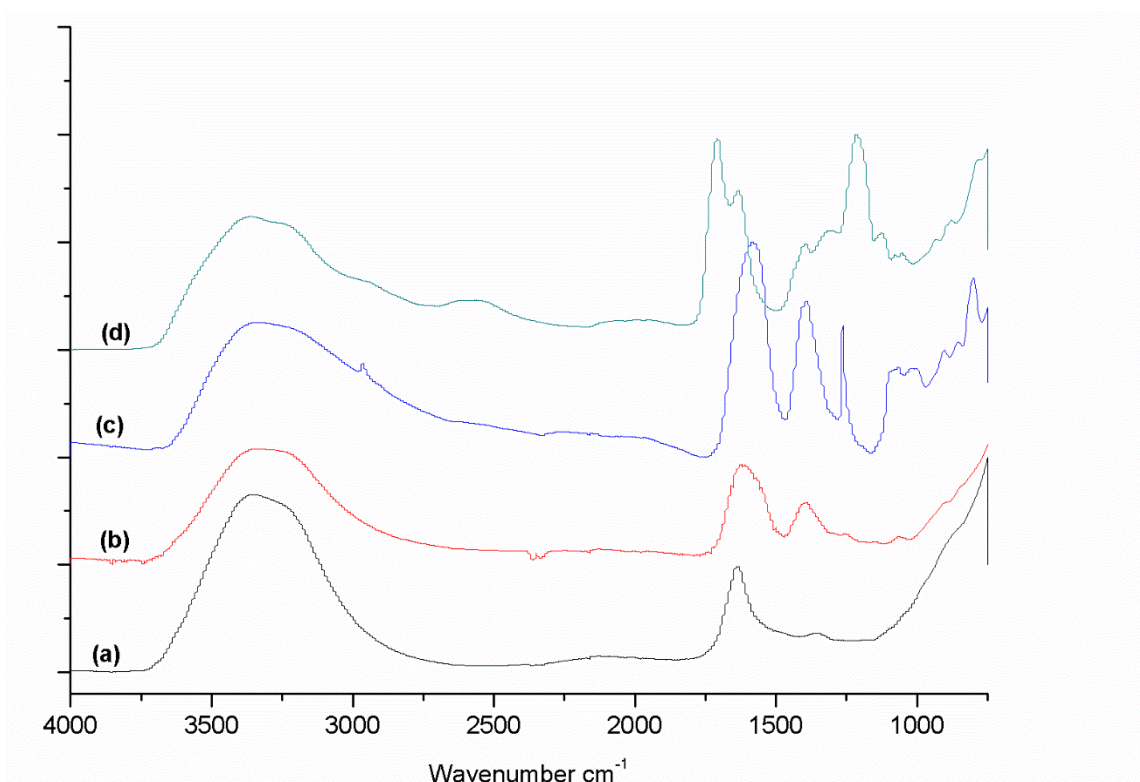


Figure 2.9 FTIR spectra of FF-bare (a), FF-CIT pre-OHP (b), FF-CIT post-OHP (c) and neat citric acid (d)

The FTIR spectra for FF-bare, FF-GLY and glycerol (neat) is shown in Figure 2.10. It is evident that glycerol is detectable through ATR-FTIR where absorbance of peak at range (1500–1200) cm^{-1} indicates glycerol moiety.^{184,185} These peaks are assigned to overlapping of C–H in planes and O–H bending in the glycerol molecule. The O–H bending is further supported by the –OH stretching at peak range of (3500–3000) cm^{-1} . The occurrence of O–H vibration from 2-hydroxyethyl chain at broad peaks about 3242 cm^{-1} indicates presence of –OH functional group. Besides, peak observation from range (2937–2881) cm^{-1} further specifies presence of glycerol. The two peaks observed are due to CH_2 and CH vibration of the O-methylene and O-methylidyne groups.

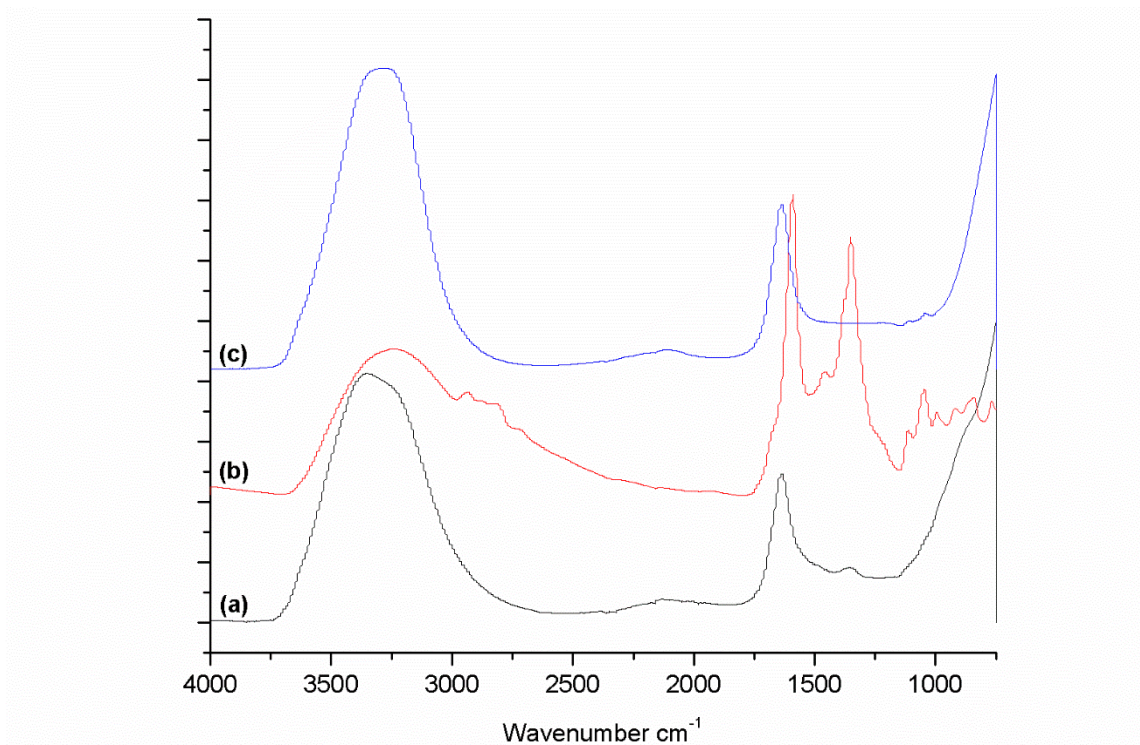


Figure 2.10 FTIR spectra of FF-bare (a), FF-GLY (b), and neat glycerol (c).

For oleic acid coated neat cobalt ferrite nanoparticles peaks at $\sim 2922\text{ cm}^{-1}$ and 2853 cm^{-1} can be observed and is a characteristic band for the asymmetric and symmetric C-H stretches, respectively, of the CH_2 group, that is expected from oleic acid (Figure 2.11).¹⁸⁶ The peak located at 1708 cm^{-1} indicates the presence of the C=O group of carboxyl functional group, and the peak at 1463 cm^{-1} is caused due to C-C vibrations. Vibrational bands corresponding to the C-O and CH=CH groups were observed at 1282 cm^{-1} and 722 cm^{-1} , respectively.¹⁸⁷

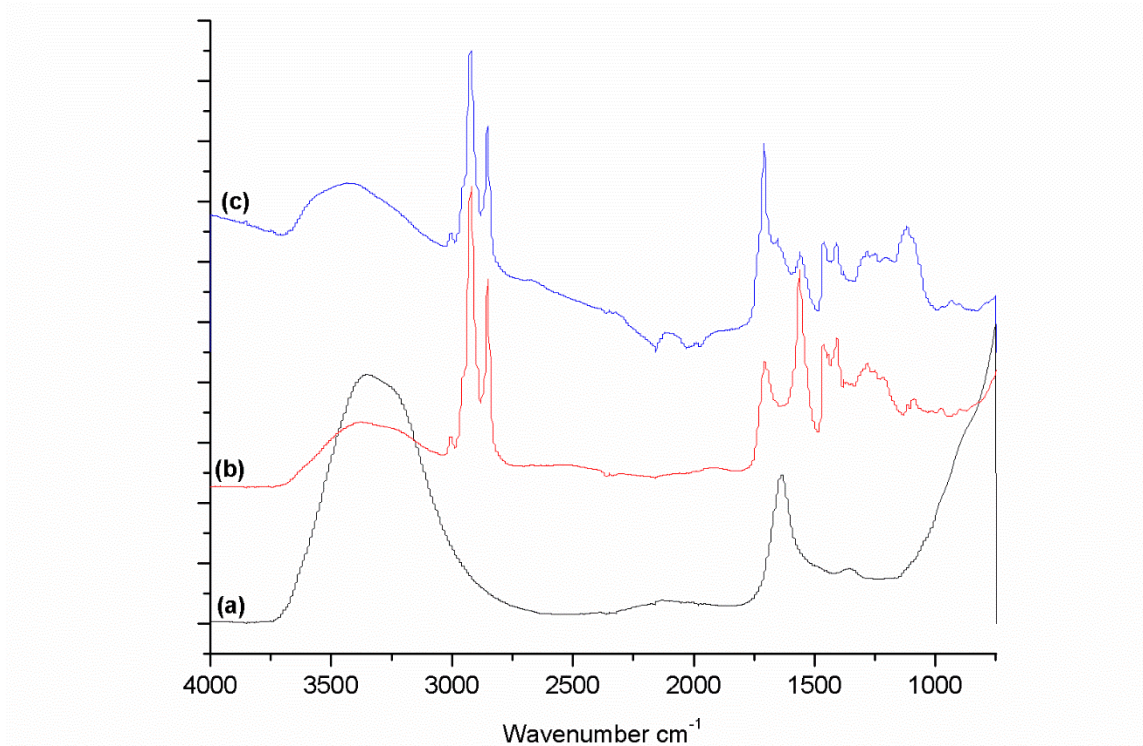


Figure 2.11 FTIR spectra of FF-bare (a), FF-OA (b), and neat oleic acid (c).

Figure 2.12 contains the FTIR spectra FF-bare, FF-OXA and oxalic acid (neat). Band characteristics of the spectrum includes: peaks in the region from 1600 cm^{-1} to 1800 cm^{-1} attributed to carbonyl stretching vibrations; 1639 cm^{-1} peak due to asymmetric O-C=O stretching; 1306 cm^{-1} peak corresponding to C-O symmetric stretching; and 1424 cm^{-1} peak from the symmetric stretching modes of C-O, C-C and O-C=O bonds.¹⁸⁸

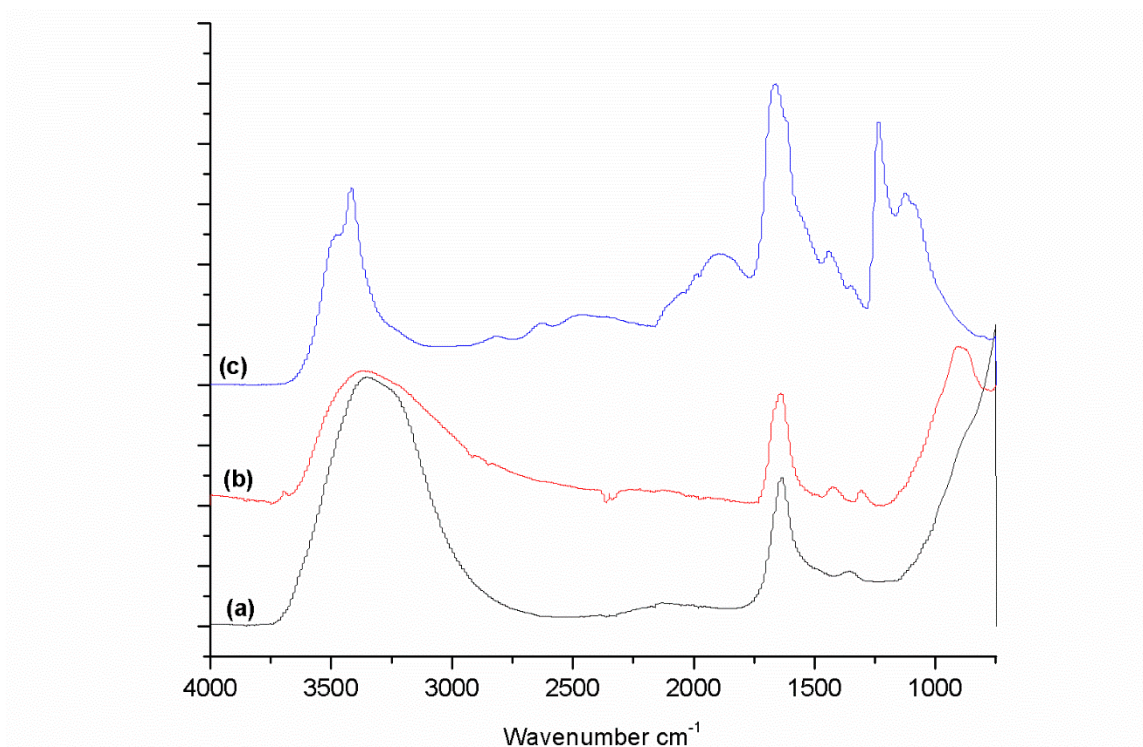


Figure 2.12 FTIR spectra of FF-bare (a), FF-OXA (b), and neat oxalic acid (c).

An FTIR spectra of ferrofluid with PEG capping agent is displayed in Figure 2.13. C-O-C bonds correspond to the narrow intensity peaks around 1099 cm^{-1} whereas spectrum from $\sim 3200\text{ cm}^{-1}$ to 3700 cm^{-1} contain peaks due to O-H stretching. C-H stretching in CH_2 groups resulted in an absorption peak at 2868 cm^{-1} .^{189,190}

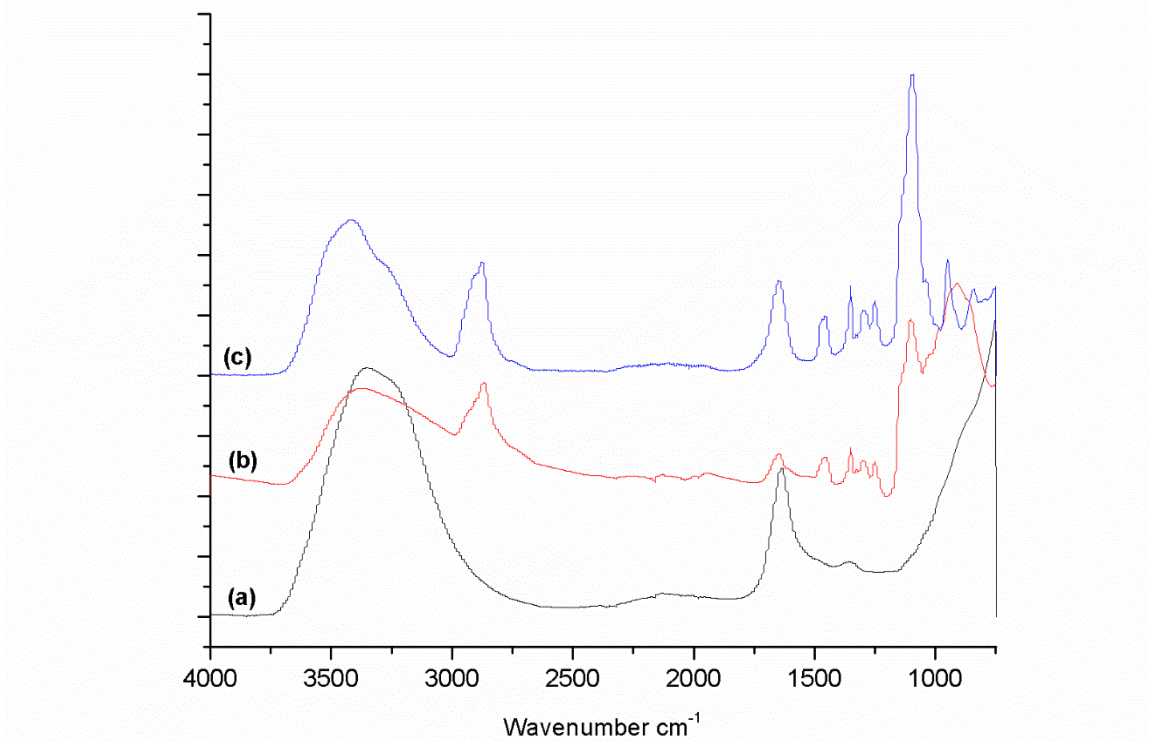


Figure 2.13 FTIR spectra of FF-bare (a), FF-PEG (b), and neat PEG (c).

FTIR spectra for SDS-coated CoFe_2O_4 nanoparticles, neat ferrofluid as well as neat SDS are shown in Figure 2.14. Peaks in the $2850\text{--}2950\text{ cm}^{-1}$ region are due to alkane C-H bonds from the aliphatic content.^{72,73} The region from 1210 cm^{-1} to 1240 cm^{-1} displays peaks for the stretching vibration of the C=O group combined with the N-H group due to the sulfate group in SDS. Hydroxyl group effect is seen in the form of peak around 3300 cm^{-1} .

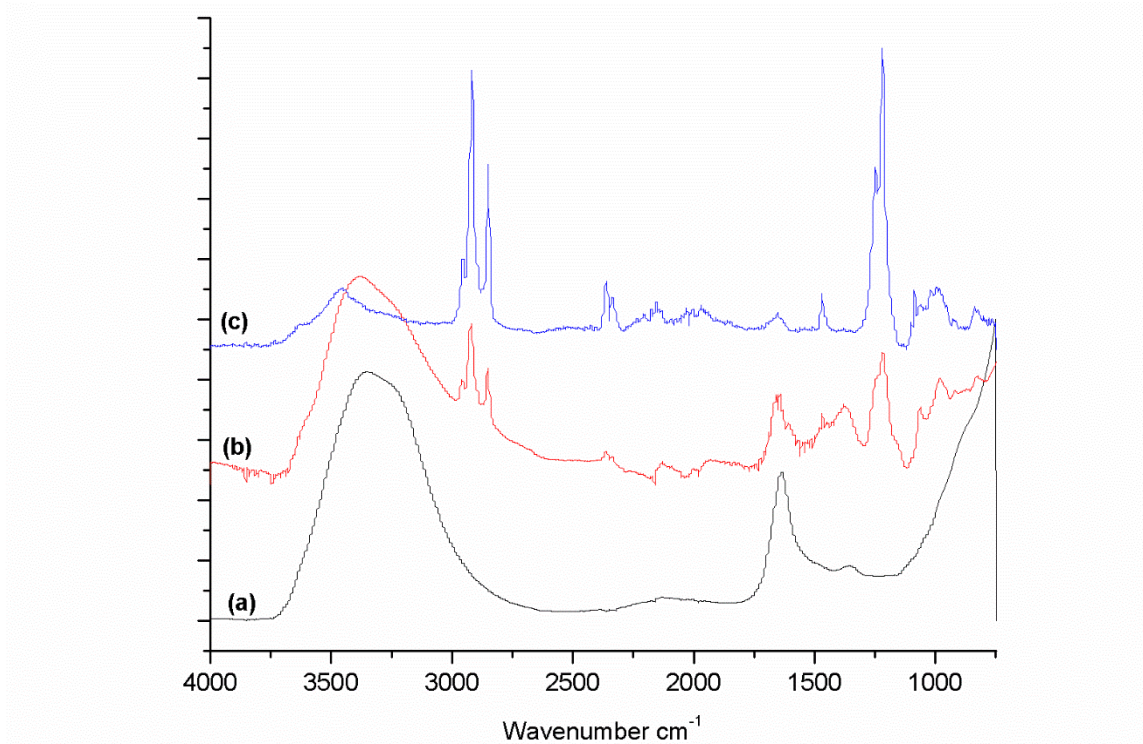


Figure 2.14 FTIR spectra of FF-bare (a), FF-SDS (b), and neat SDS (c).

The broad band around 3400 cm^{-1} were attributed to the asymmetric stretching whereas bands at 1110 cm^{-1} is due to the symmetric stretching and rocking vibrations of HClO_4 .^{193,194} These peaks confirms the attachment of perchloric acid to FF-bare.

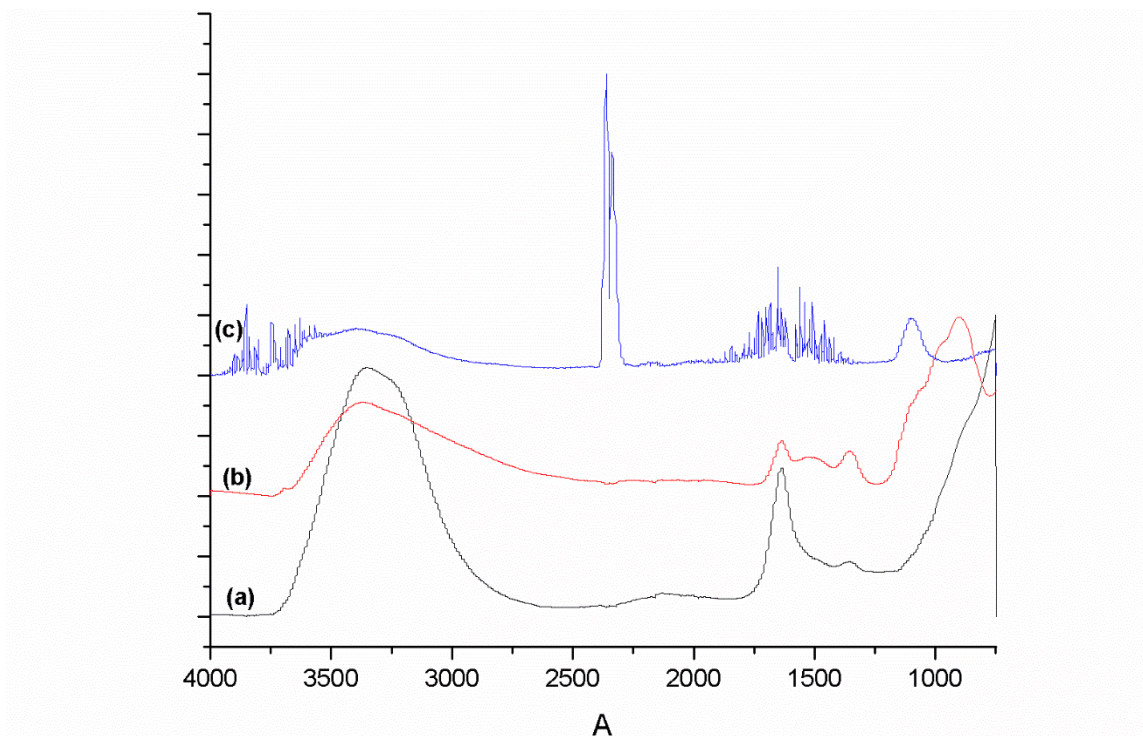


Figure 2.15 FTIR spectra of FF-bare (a), FF-PCA (b), and neat perchloric acid.

2.4.1 Need for Surface Modification of MNPs

The average effective diameter measured just after the FF-bare was synthesized, was 123.6 nm +/- 5.5 nm. It was noted that after about three months, these same FF-bare nanoparticles had aggregated and the average diameter had increased to 1877 nm +/- 119 nm. In order to avoid this agglomeration, bare cobalt-ferrite nanoparticles were coated with different ligands and their corresponding size is shown in the Table 2.1.

Table 2.1 Comparison of average particle diameter for FF-bare and those modified by different ligands.

Sample – Surface Modifier	Effective diameter (nm)	Δ Thickness (nm) +/- 95%CI
FF - bare	123 ± 5	---
FF – CA (pre-OHP)	142 ± 3	18 ± 6
FF – CA (post-OHP)	174.72±2.9	51.1± 6.2
FF – PCA	200.9 ± 10.3	77.3 ± 11.6
FF – OA	221.4 ± 8.0	97.8 ± 9.7
FF – PEG	250.6 ± 8.4	127.0 ± 10.0
FF – SDS	296.9 ± 6.0	173.3 ± 8.1
FF – GLY	703.0 ± 26.4	579.4 ± 26.9
FF – OXA	896.2 ± 21.3	772.6 ± 22.0

Another technique utilized to determine the morphology and magnetic property change was AFM/MFM. The height imaging determines the topography and assists with understanding the particle morphology and particle-particle interactions. Additionally, MFM shows magnetization points on the nano- and micro-scales for the bare and surface modified nanoparticles using different ligands. Height sensor, phase image, and magnetic phase for all of the ferrofluid samples are shown in Figures 2.13-2.21 b,c,d. TEM imaging was also used to help examine the primary particle size and morphology as shown in Figure 2.13a. Once the samples were allowed to dry, aggregation naturally occurs. Particle sizes measured using DLS was confirmed by TEM imaging. TEM image of FF-bare shows size to be a little larger about 200 nm instead of 123 nm observed by DLS. Size calculated for FF-CIT shows consistency with DLS measurement i.e., about 150 nm. Magnetic phase image of FF-bare shows higher magnetic response than FF-CIT which can be due to the fact that all the nanoparticles had separate spin but due to agglomeration overtime, ligands need to be used. FF-oleic acid formed a slimy layer due to the hydrophobic tail hanging away from water and a very light intensity image was

captured. The AFM for FF-OA was also shown with lots of undulations. It suggests a rough surface modification and not a favorable ferrofluid surfactant when water is used as a carrier, possibly that was the reason for such low voltage generation in pump loop set up. The largest size measured by DLS was of FF-OXA which is ~800 nm and the corresponding TEM image shows aggregated large particle in shape of rods and spheres about the same size. Due to the bulky group attached to FF-bare of oxalic acid, the magnetic phase shows less intensity depicting loss of magnetization which corroborates to the same type behavior as observed in pump loop findings as shown in Figure 2.4. There was no correlation of DLS measurement to TEM image for FF-PCA, since DLS gives ~ 200 nm size where as in TEM image it is a little less than 100 nm. Even the surface image captured by AFM is almost flat and the magnetic phase intensity is also low. Though FF-PEG shows hydrodynamic size of ~ 250 nm but looking at the morphology through TEM it shows very small nanoparticles about 2-3 nm linked linked chains. Both, the DLS and TEM image almost match for FF-SDS. Though, FF-SDS did not generated much energy out of the pump loop set up but shows strong magnetic domains suggesting that there has not been a significant loss of magnetic property. It can be assumed that the long chain of SDS might be interfering in oscillations. As, the large size was observed by DLS, similarly TEM shows large aggregates of FF-GLY.

AFM images of all of the ferrofluid samples showed a decrease in magnetic phase versus the neat (unmodified) cobalt-ferrite nanoparticles. Among all ligands tested, the citric acid modified ferrofluids showed dispersed nanoparticles and also a strong magnetic phase signal. These data combined with the high voltage outputs measured for

these samples, compared to the bare samples, suggests that citric acid does help stabilize the nanoparticles but does not significantly decrease magnetic properties.

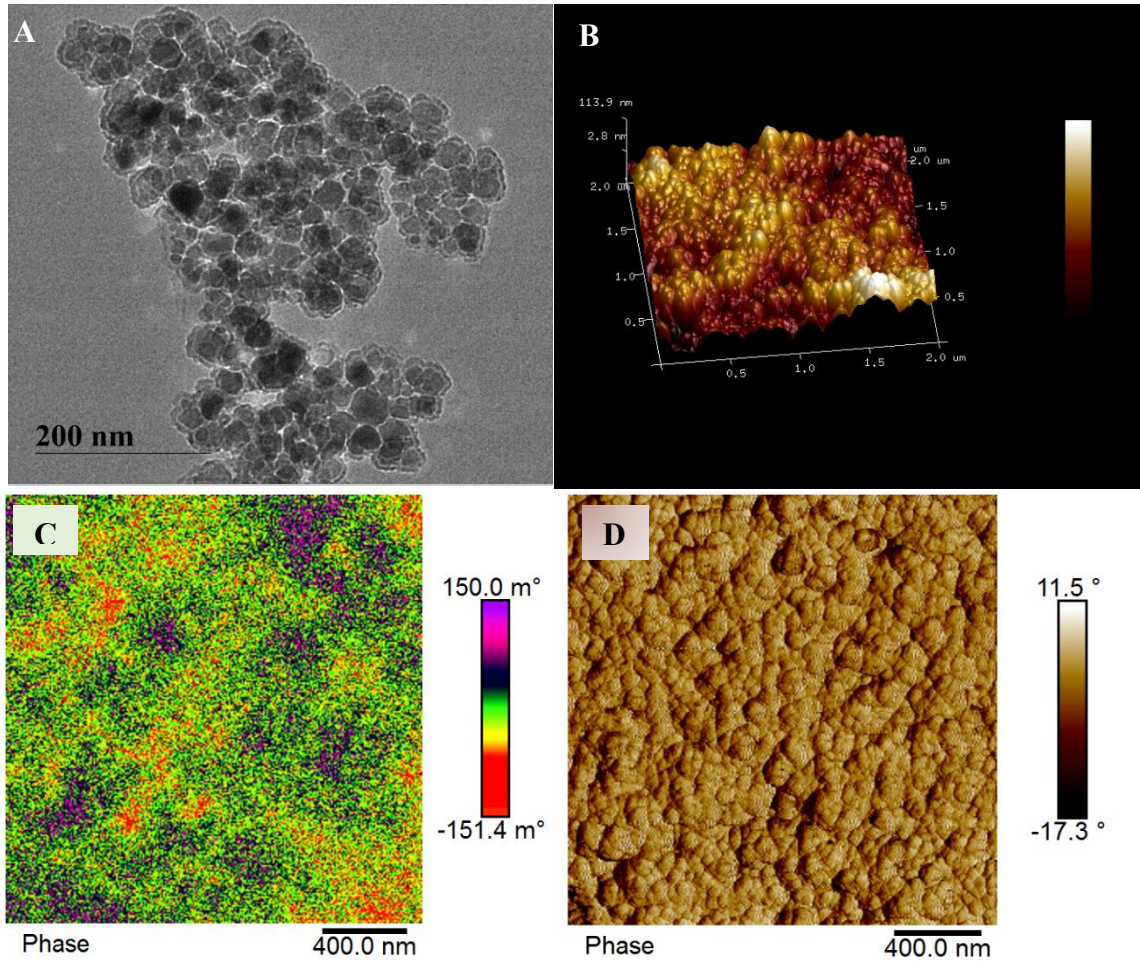


Figure 2.16 TEM (A), AFM topography (B), MFM phase (C), and AFM phase (D) images for FF-bare

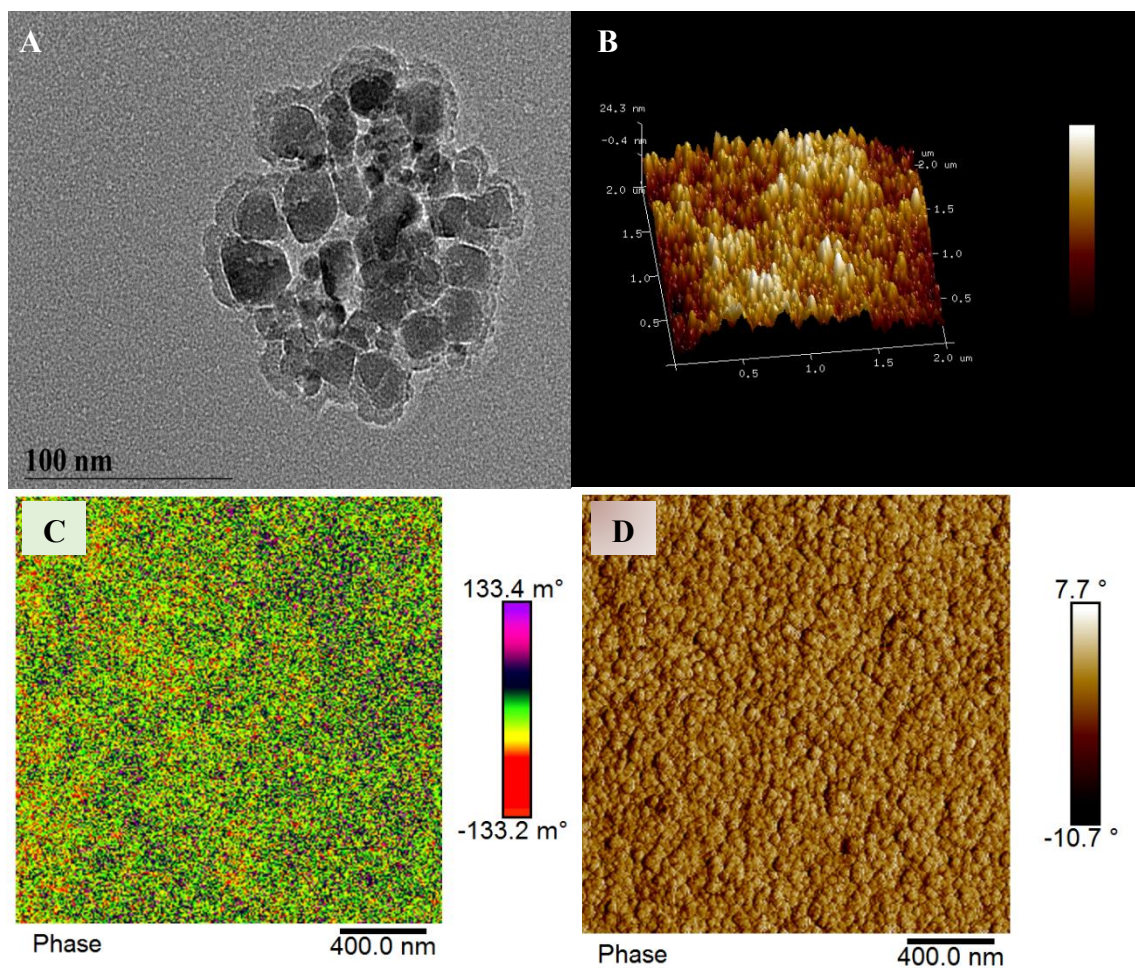


Figure 2.17 TEM (A), AFM topography (B), MFM phase (C), and AFM phase (D) images for FF-CIT

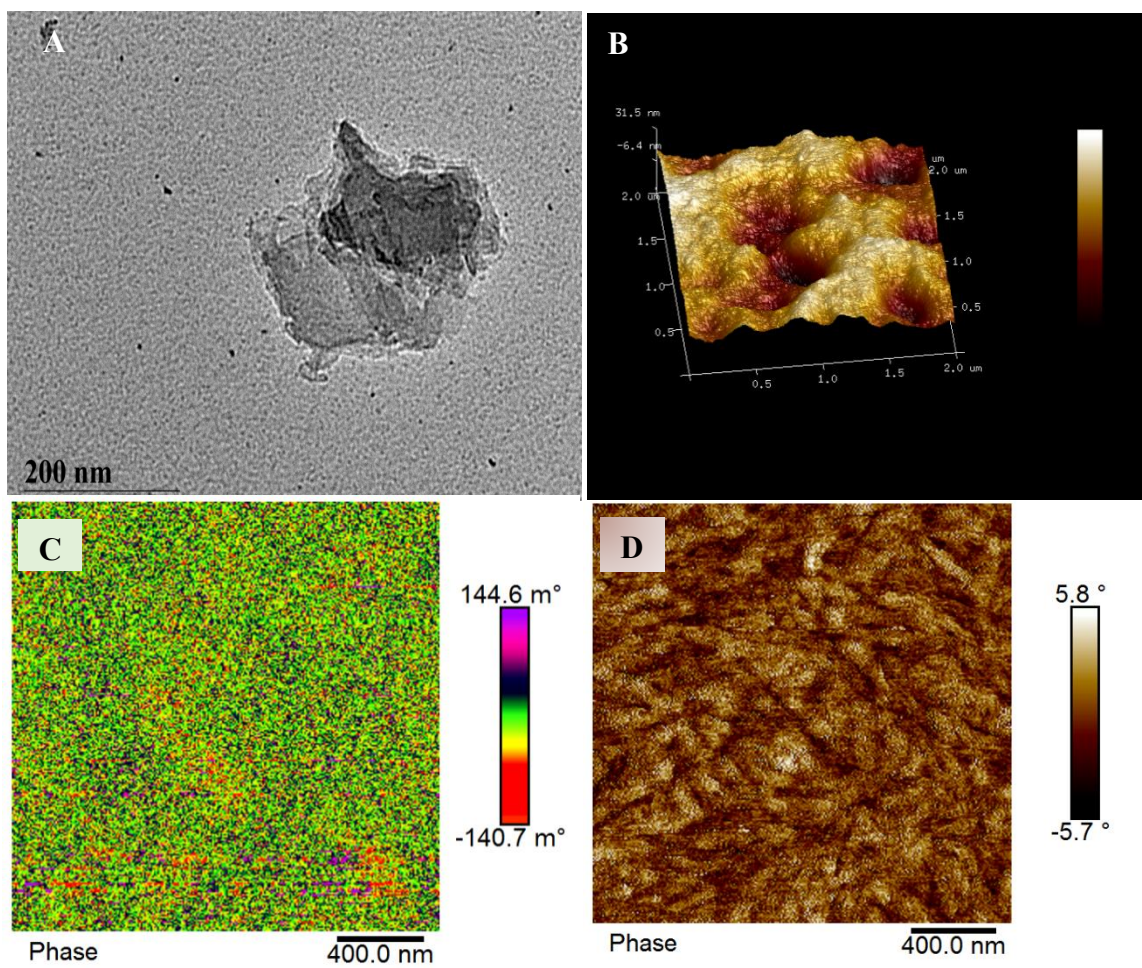


Figure 2.18 TEM (A), AFM topography (B), MFM phase (C), and AFM phase (D) images for FF-OA

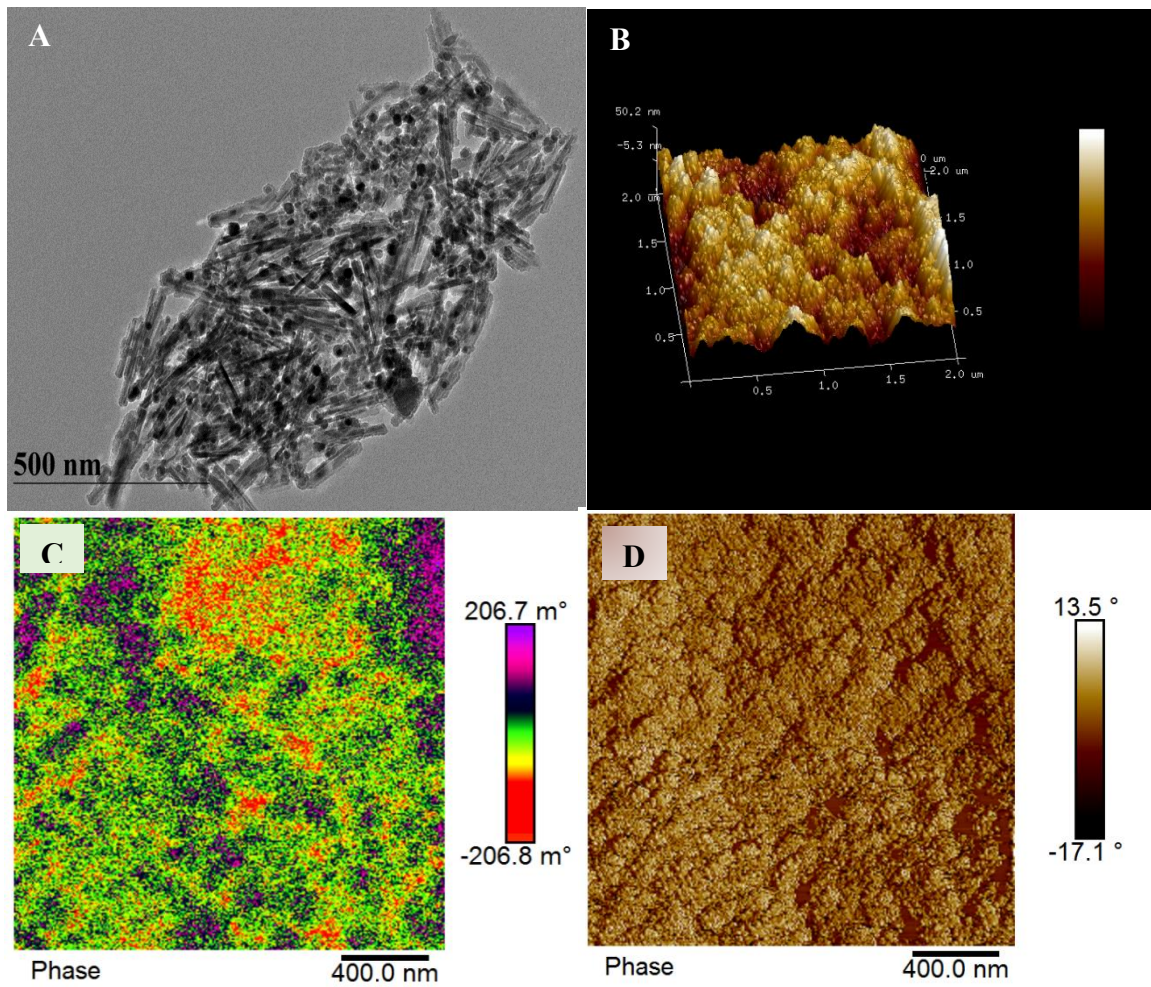


Figure 2.19 TEM (A), AFM topography (B), MFM phase (C), and AFM phase (D) images for FF-OXA

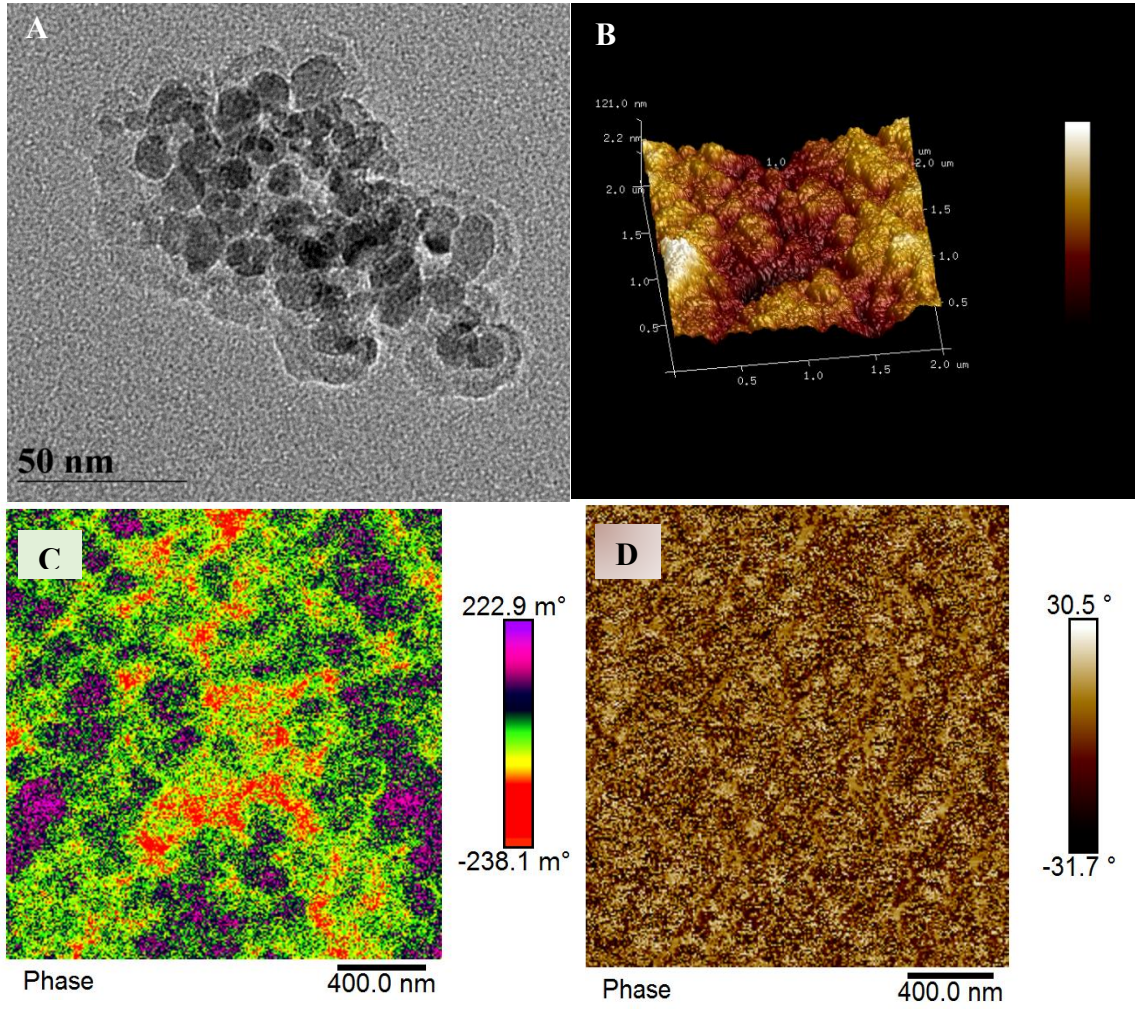


Figure 2.20 TEM (A), AFM topography (B), MFM phase (C), and AFM phase (D) images for FF-PCA

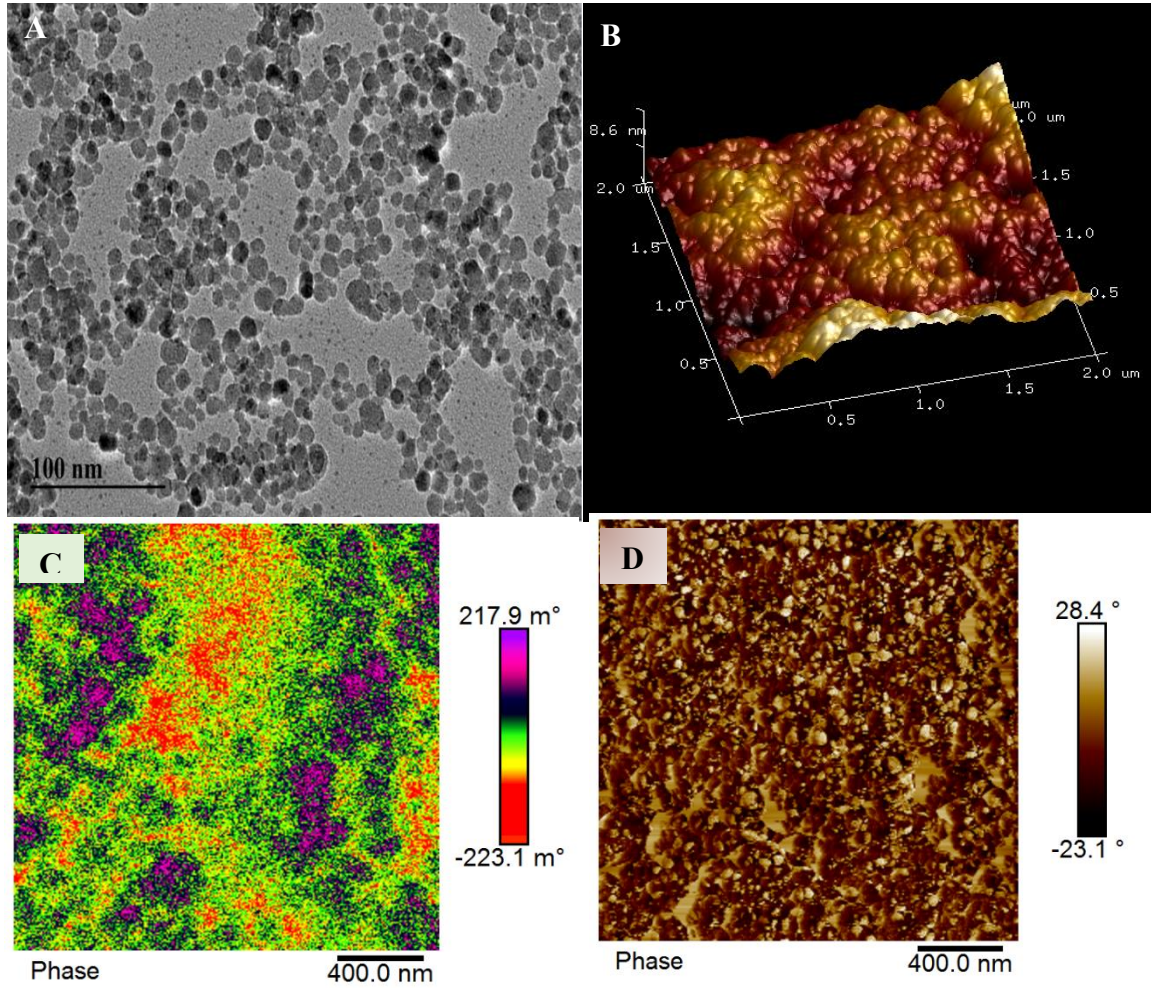


Figure 2.21 TEM (A), AFM topography (B), MFM phase (C), and AFM phase (D) images for FF-PEG

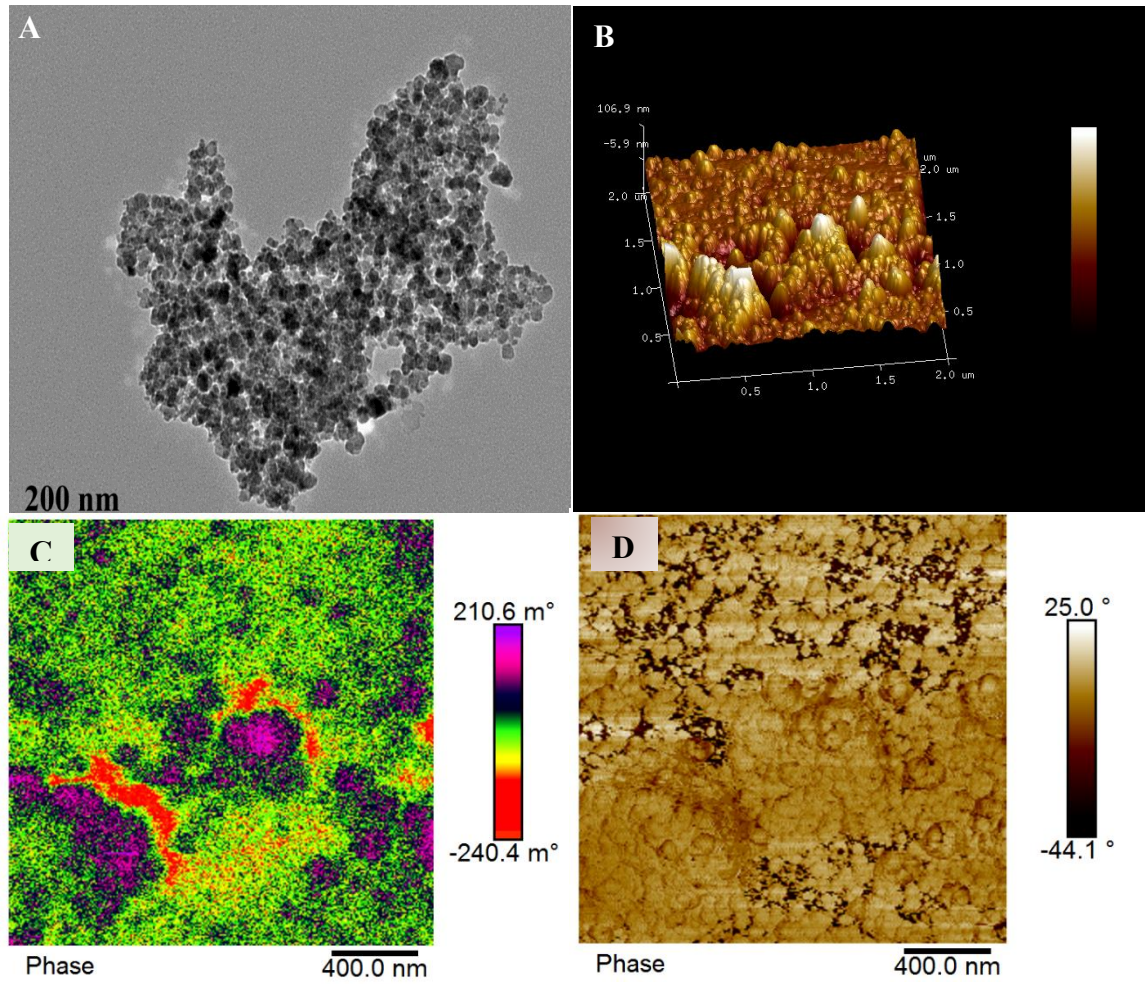


Figure 2.22 TEM (A), AFM topography (B), MFM phase (C), and AFM phase (D) images for FF-SDS

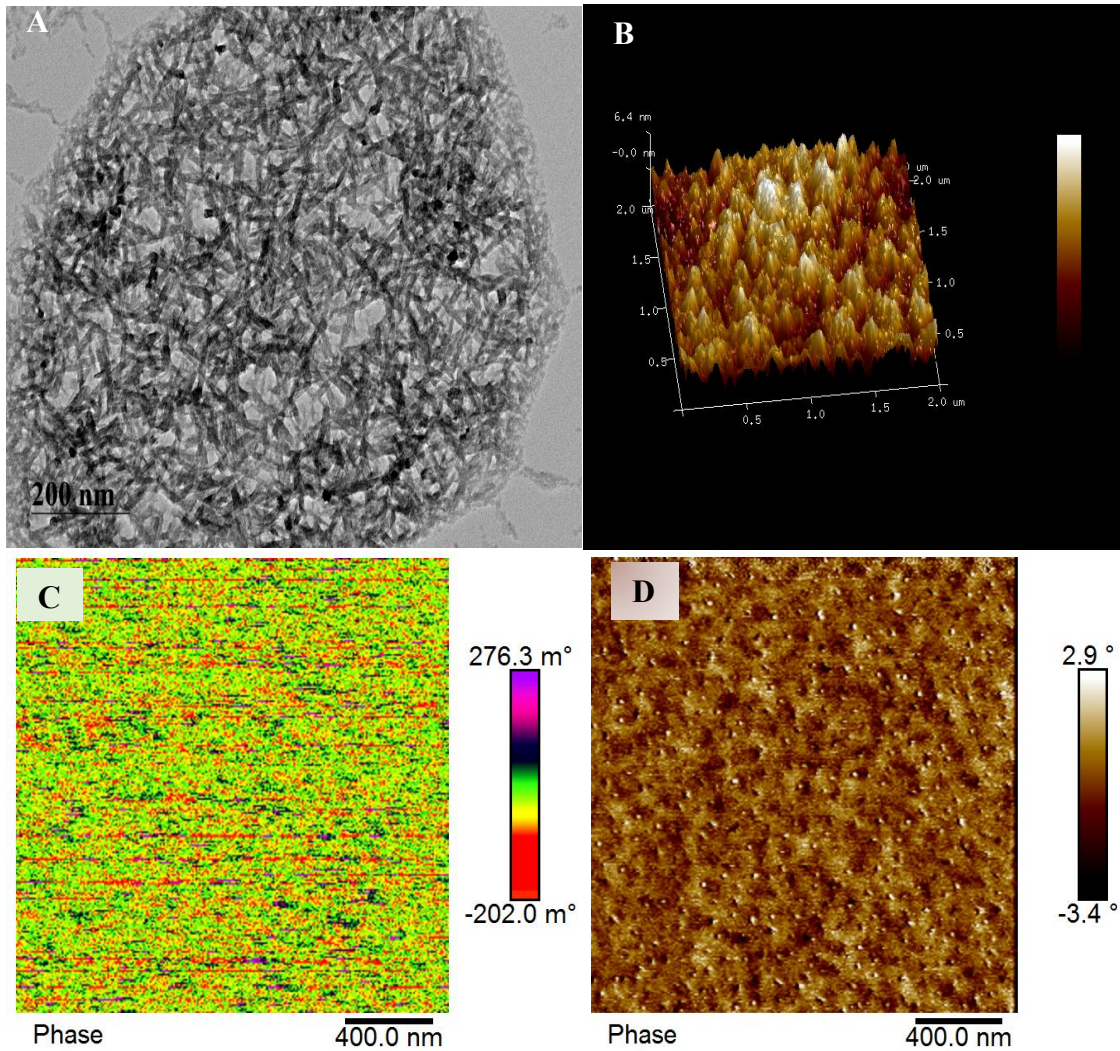


Figure 2.23 TEM (A), AFM topography (B), MFM phase (C), and AFM phase (D) images for FF-GLY

2.5 Conclusions

Seven different ligands were used for surface modification of bare cobalt-ferrite nanoparticles. ATR-FTIR confirmed the successful attachment of ligands to the FF-bare. The size and morphology was studied by TEM and DLS. The breakage of mosaic or multi-core nanoparticles leading to decrease in energy harvesting through OHP was

successfully eliminated by replacing it with in-house synthesized cobalt-ferrite nanoparticles. And moreover surface modifying for stability over a longer time. In this study, initial investigation of ferrofluid for voltage measurement was done in a peristaltic pump. After comparing with previous study, FF-CIT was charged to OHP and almost 200% more voltage was harvested.

2.6 Future Efforts

Future work will analyze other types of surface modifications that would lead to enhancement in MNPs for various heat transfer applications. In present work, cobalt ferrite nanoparticles were studied in incipient stage of investigation, and found with its possibility of potential heat transfer applications. Also, alternative synthesis methods, other than co-precipitation could be used to prepare ferrous based nanoparticles and to make it well dispersed. Water has been used as solvent for this study. In order to improve suspension of nanoparticles in fluid, other organic solvents such as ether, methanol or acetone can be implicated. Further, calcination of the bare nanoparticles before surface modification can also be done to enhance the magnetization of nanoparticles. In this work, we used concentration of the ferrofluid as 1mg/mL. We believe that an optimization of concentration, of ferrofluid will help to maximize energy output through OHP.

CHAPTER III
SYNTHESIS AND CHARACTERIZATION OF COBALT ZINC FERRITE
NANOCOMPOSITES

3.1 Abstract

Superparamagnetic cobalt-zinc ferrite (CZF) nanoparticles were synthesized from aqueous metal salt solutions by co-precipitation. In this study, 3-aminopropyltrimethoxysilane (APTES) hydrothermal approach was used to synthesize APTES modified CZF nanoparticles. Then temperature sensitive poly(N-isopropylacrylamide) (PNIPAM) was grown from the nanoparticle by surface-initiated atom transfer radical polymerization (Si-ATRP), a versatile synthesis to grow well-defined polymers from substrates. Chemical composition, size, and morphology of these polymer-grafted metal nanocomposites, CZF-APTES@PNIPAM, were examined using Fourier transform infrared spectroscopy, dynamic light scattering, and transmission electron microscopy. CZF magnetic nanoparticles—especially coupled with a thermo-responsive polymer—have significant potential in biomedical applications such as drug delivery and as a magnetic hyperthermia ferrofluid (MHF) for cancer cell eradication.

3.2 Introduction

Nanocomposites comprised of magnetic nanoparticles (MNP) and stimuli responsive polymers (SRP) have unique physical and chemical properties (in addition to those typical of nanoparticles). MNPs are increasingly being used for a large number of

biomedical applications ranging from drug delivery, energy immobilization, magnetic resonance imaging (MRI), magnetic fluid hyperthermia (MFH).^{195–201} Being superparamagnetic in nature boosts its usability than several other nanomaterials. Especially, it can be used for treatment of cancer modalities,^{202–204} in isolation or along-with existing methods such as chemotherapy and radiotherapy. Figure 2.1 illustrates the process of nanomaterial-based strategies for tumor diagnosis, imaging and therapy. The advantage of magnetic nanoparticles lies in their sensitivity to the magnetic field, they are strongly magnetized in magnetic field and likewise lose their magnetization on the removal of field. As a consequence, these nanoparticles have little tendency to aggregate due to magnetic dipole–dipole interactions (especially if their magnetic core is shell-protected), thus decreasing the risks of embolism, which is crucial in tumor formation.²⁰⁵ On exposure to oscillating magnetic fields, these MNPs dissipate magnetic energy into the form of thermal energy through distinct mechanisms (Brownian and Néel)²⁰⁶ as the particle returns to its equilibrium state. The dissipation process can be modeled by Brownian relation wherein heat is dissipated as frictional losses from the rotation of nanoparticles in the surrounding medium, while the Néel relaxation relates to the rotation of magnetic moments within nanoparticle magnetic core. However inside the biological tissues, the Brownian relaxation gets hindered by the relatively high viscosity of the medium surrounding the particle.^{206,207} As a result, designing of nanoparticles for hyperthermia applications should be tailored such that heat released through the Néel mechanism is maximized. Besides the strength and frequency of the external magnetic field applied to MNPs, parameters such as nanoparticle size, shape and material, as well as grain structure (which can affect hysteresis properties such as remanence and

coercivity) can influence in generation of heat.²⁰⁸ Magnetic nanoparticles (MNPs) are therefore injected locally into tumors because high concentration of the MNPs can critically cause the local temperature to increase from the magnetic heating.^{209,210} CZF(cobalt-zinc ferrous) magnetic nanoparticles is an example of magnetic nanoparticle that has been found to be very effective for breast cancer by eradication 80% of breast cancer cells (MCF7 cell line) when used as a MHF with an induced electromagnetic field.²¹¹ The cobalt ferrite MNPs are increasingly being used in other fields such as gene therapy and cellular function manipulation due to their very useful property.^{212,213}

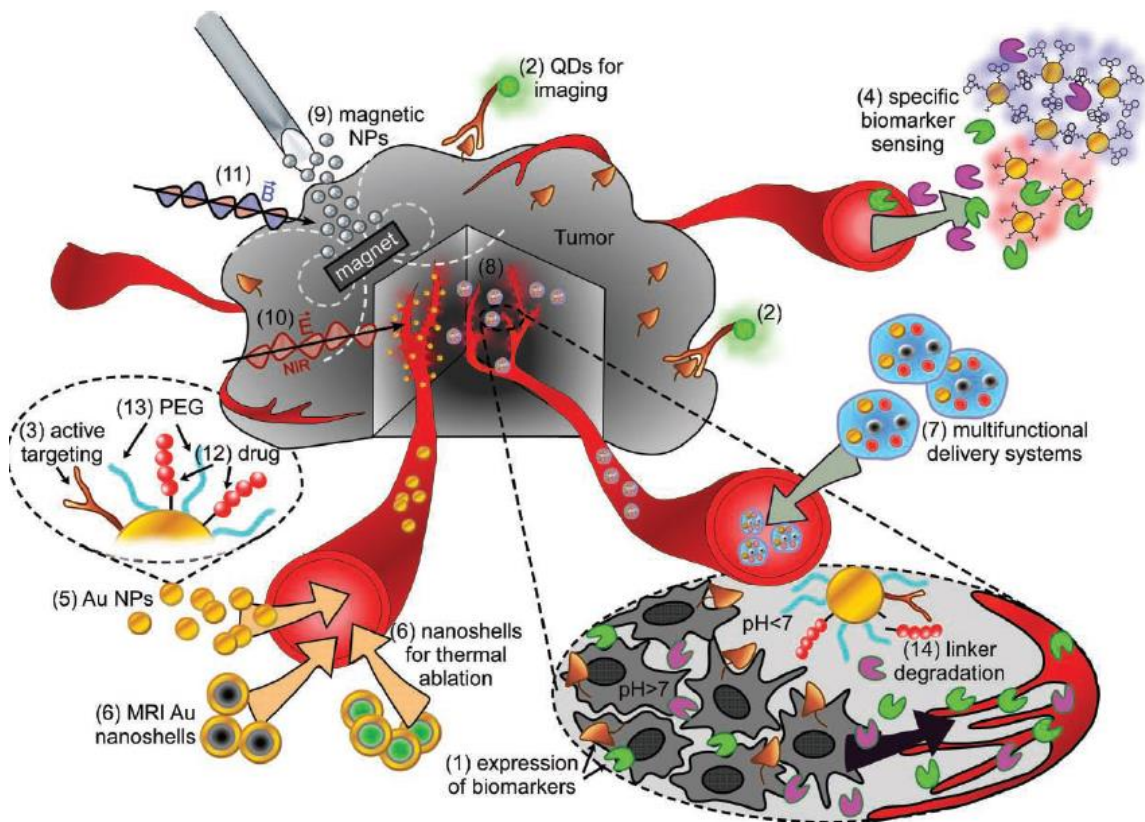


Figure 3.1 Nanomaterial-based strategies for tumor diagnosis, imaging and therapy.²⁰⁵

Cobalt ferrite (CoFe_2O_4) has exceptional physical and mechanical properties that makes it a promising material for future biomedical applications like magnetic resonance imaging, radio-frequency hyperthermia, drug delivery and medical diagnosis.^{214–217} We will see the elaboration of its application in hyperthermia in subsequent section. The main reason for using the Co-ferrite for medical applications is its high magneto-crystalline anisotropy which originates from L-S spin orbit coupling at crystal lattices.²¹⁸ Its physical properties consist of a paramagnetic material with a high curie temperature (520 °C), high coercivity of about 4.3 kOe at room temperature for the 40 nm size single domain, moderate saturation magnetization of about 80 emu/g for bulk at room temperature, high anisotropy constant (2.65×10^6 – 5.1×10^6 erg cm^{-3}) and high magnetostrictive (-225×10^{-6}).^{219–221} Furthermore, it shows excellent chemical stability, mechanical hardness, wear resistance, ease of synthesis, and electrical insulation. Therefore, besides medical application, it can also be used in electronics, biosensors, catalysis, magneto-optic devices, solar, data storage and microwave devices.²²² Also, its mechanical and magnetic properties can be tuned by controlling doping agent like Zn, Mn and Ni oxides. In this section we will confine ourselves to addition of Zn^{2+} as dopant. When the cobalt ferrite nanoparticle is doped with Zn^{2+} , it is called cobalt zinc ferrite (CZF).^{221,222} When Zn^{2+} ions are substituted for Co^{2+} at the tetrahedral sites, it increases the lattice parameter because Zn^{2+} has higher ionic radius (~ 0.880 Å), as compared to the Co^{2+} (0.838 Å). On contrary, if Fe^{3+} is replaced at octahedral site by Fe^{3+} , one can obtain small lattice parameter. Zn^{2+} ions in high amounts can reduce the Curie point, the coercivity and the saturation magnetization.^{218–220} Therefore, based on the application, desired properties can be tuned. The mechanism of reduction in saturation magnetization

due to presence of Zn^{2+} can be explained as: presence of Zn^{2+} with zero angular momentum in the ferrite lattice decreases the anisotropy of the cobalt ferrite. Thus, both saturation magnetostriction and coercivity decrease but the magnetostrictive sensitivity (MS) is improved.²²³⁻²²⁶ For comparison: the saturation magnetization of $CoFe_2O_4$, $Co_{0.8}Zn_{0.2}Fe_2O_4$ and $Co_{0.6}Zn_{0.4}Fe_2O_4$ are 72.1 emu/g, 89.7 emu/g and 99.7 emu/g respectively. The reason for the increase of MS is the presence of Zn^{2+} ions with the zero magnetic moment that replace Co^{2+} ions at the tetrahedral A-sites,²²⁷ The tetrahedral A-sites can be defined as the interstitial site in the center of a tetrahedron formed by four lattice atoms. Three atoms, touching each other, are in plane; the fourth atom sits in the symmetrical position on top can be referred to as A-site of tetrahedron as shown in the Figure 3.2. This substitution decreases the magnetic moment in this sub-lattice, resulting in an increase in the total magnetic moment. Therefore, increase in Zn substitution level at lower temperature increases the saturation magnetizations.

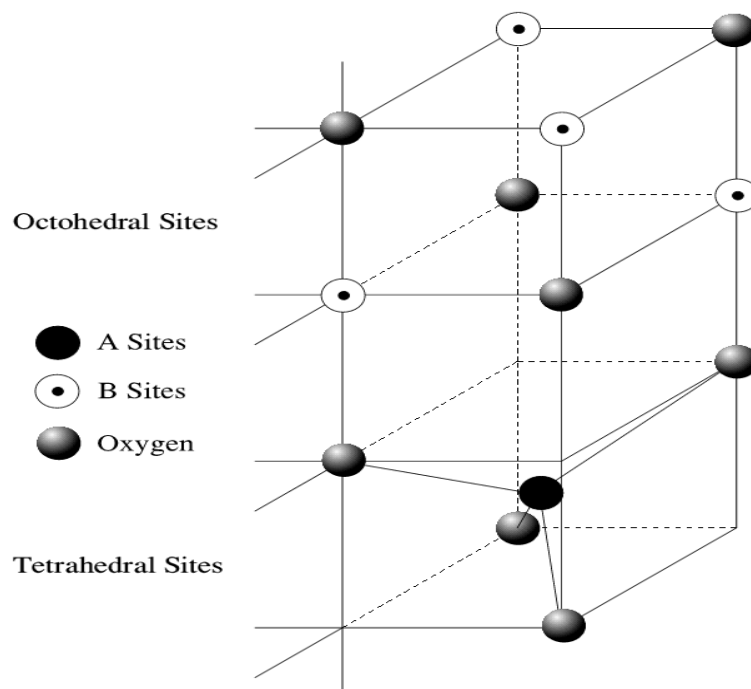


Figure 3.2 Two different lattice sites in magnetite ²²⁸

The CZF is prepared generally by thermal decomposition methods which involve decomposition of metal precursor in high boiling temperature solvent in the presence of stabilizing agents. Unfortunately, the product received at the end is reported to be highly organic solvent which prevents it from being used in biomedical applications. ²²⁹ Several techniques are evolving to make better products like amine functionalized ferrite is produced for MRI applications. ²³⁰ Recently, another advance in the same field is reported ²¹⁴ for monodispersed amine functionalized CZF magnetic nanoparticle and showed to be highly aqueous stable.

Hyperthermia: Co-ferrite nanoparticles with high magnetic crystalline anisotropy, moderate saturation magnetization and small super-paramagnetic size are suitable for the hyperthermia application. Also, effective and controlled heat generation

can be given by well-dispersed cobalt nanoparticles. The amount of heat generated by magnetic nanoparticles can be determined by the magnetic moment, field, frequency, and particle volume because the heat generation is described by power loss due to Brownian and Neel relaxation mechanisms.^{98,231} Thus magnetic field and frequency of CoFe_2O_4 can be adjusted to achieve desired heating to achieve the magneto-thermally triggered drug delivery and hyperthermia. Magnetic CoFe_2O_4 nanoparticles respond resonantly to a time-varying magnetic field related to the transfer of energy from the exciting field to nanoparticles. The specific absorption rate is an important parameter in the hyperthermia treatment, and is very high ($396 \text{ W/g}_{\text{Fe}}$) for CoFe_2O_4 .²³²

Polymers made from N-isopropylacrylamide (NIPAM) are one of the most studied thermo-sensitive hydrogel in last 50 years.^{233–237} It was first synthesized in 1950's via free radical mechanisms.^{238,239} NIPAM shows thermally induced de-swelling at temperatures over $32 \text{ }^\circ\text{C}$. At lower temperatures, water is a good solvent due to hydrogen bonding with NIPAM's amide groups. However, at temperatures above $32 \text{ }^\circ\text{C}$, the bonding is disrupted due to high temperature and leads to the collapse of the chains. Those collapsed chains tries to minimize interaction with the solvent and leads to the formation of microgel.^{240–244} Figure 3.3 shows the depiction of NIPAM in poor and good solvents, respectively. Thus, inter- and intra-polymer hydrogen bonding and polymer-polymer hydrophobic interactions becomes dominant above the LCST (low critical solution temperature).^{245–247} The Flory-Huggins theory of polymeric solutions is not able to define the system clearly. One of the most accepted swelling theory for this system is given by lattice fluid hydrogen bonding theory (LFHB),²⁴⁸ which shows how the hydrophilic and hydrophobic interactions could be used to control the transition

temperatures of gels within poly(NIPAM) water alcohol system.^{249–251} Further, it is shown that the swelling can be controlled by addition of alkanols^{252,253} which causes sol-to-globule transition.

Further, the structure of the micro-emulsions was also investigated by small angle neutron scattering (SANS). It is a technique widely used to characterize the shape and size of macromolecules and particles of order of nanometer to micrometer. The structure of micro-emulsions resembles spheres. The investigators used the combination of sphere form factor, which characterizes the size of the spherical particle, with Lorentz model. The Lorentz model is used to estimate the characteristic size particles by estimating the scattered neutron intensity with the scattering angle. For sphere, its intensity varies with the inverse fourth power of scattering angle.²⁵⁴

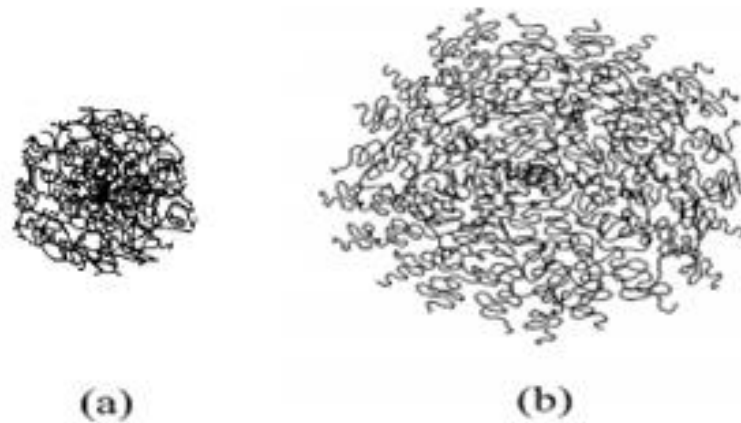


Figure 3.3 Schematic depicting a microgel particle in a poor (a) and good (b) solvent, respectively.

The properties of this system can be tuned by functionalizing the end groups shown vastly in literature. Other than the temperature sensitivity, the rheological properties are dependent on the volume fraction occupied by micro-emulsions. One of the rheology based applications is automotive surface coating due to its shear thinning property and thermal control over rheological property. Also, metallic flakes can be easily attached with coating parallel to the substrate. Besides, NIPAM shows promising applications in drug delivery using micro-encapsulation technique, pharmaceutical industries, printing offset plates and it can be functionalized for photo-cross linkable particles.

In literature following methods have been reported for microgel particles preparation: emulsion polymerization,^{253,255} anionic copolymerization,²⁵⁶ cross-linking of neighboring polymer chains²⁵⁷ and inverse micro-emulsion polymerization.²⁵⁸ Out of these, emulsion polymerization yields narrow particle size distributions. Emulsion polymerization can be performed in the presence of added surfactant (conventional emulsion polymerization) CEP, or in the absence of added surfactant (surfactant-free emulsion polymerization) SFEP. CEP also referred as macro-emulsion polymerization mechanism occurs into three intervals including the initial (particle formation or nucleation) stage, the particle growth stage and the completion stage.²⁵⁹ CEP enables the preparation of very small microgel particles (particle diameters < 150 nm); however, there remains a difficulty in complete removal of residual surfactant. However, in SFEP method, the continuous phase needs to have a high dielectric constant e.g. water and ionic initiators are employed (e.g. $K_2S_2O_8$). The charged polymer chains formed during polymerization act as surfactant molecules and stabilize the growing particles. Also,

SFEP does not suffer from residual surfactant contamination. Therefore, SFEP has been widely used for the preparation of PNIPAM, PS and PMMA. microgel systems.^{253,256,260} Additional applications of these MNPs are possible when they are combined with polymers such as PNIPAM which imparts a thermo-responsiveness due to the 32 °C lower critical solution temperature. In the present effort, CZF nanoparticles grafted with PNIPAM have been synthesized, physicochemical properties examined, and temperature response measured.

3.3 Experimental Section

3.3.1 Materials

Cobalt zinc ferrite nanoparticles were synthesized in the lab by co-precipitation in alkaline medium. Iron (III) chloride hexahydrate (Sigma-Aldrich, 97%), cobalt (II) chloride hexahydrate (Sigma-Aldrich, 98%), sodium hydroxide (Sigma-Aldrich, ≥98%, pellets, anhydrous), zinc chloride (ZnCl₂), N-isopropylacrylamide (NIPAM) (Aldrich, ≥99%), 2,2-bipyridyl (bpy) (Sigma-Aldrich, ≥99%), copper (I) bromide (Sigma-Aldrich, 98%), anhydrous 2-propanol (Sigma-Aldrich, 99.5%), were used as received without further purification. Water used in all experiments was purified using Millipore (Type I) with a resistivity of 18.2 MΩ·cm.

3.3.2 Synthesis of bare cobalt zinc ferrite (CZF) nanoparticles

Cobalt zinc ferrite nanoparticle were synthesized by high thermal decomposition method. Solution (100 mL) of FeCl₃·6H₂O, ZnCl₂, CoCl₂·H₂O, and NaOH were prepared in deionized water in molar ratio 2:0.5:0.5:8 respectively. All these solutions were heated to 80 °C in separate beakers. Sodium hydroxide was stirred properly in the reactor before

the above three solutions were entered and then stirred vigorously. Stirring was done for 4 hours at 768 rpm, 80 °C temperature and in nitrogen atmosphere, until a black precipitate was formed. The experimental schematic is shown in Figure 3.4.

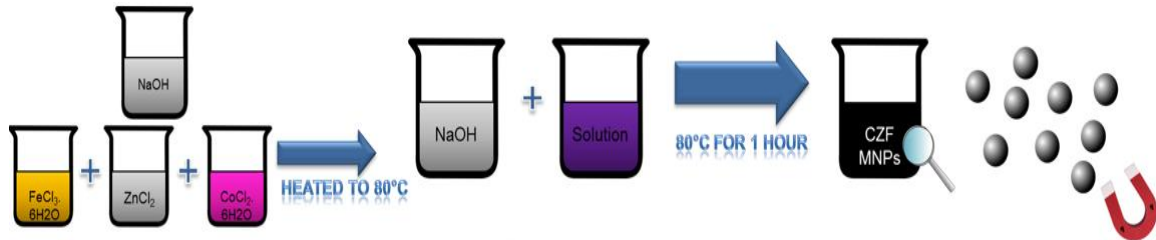


Figure 3.4 Experimental schematic for CZF synthesis

After the experimental time, solution was exposed to air and allowed to settle down under the influence of 2T magnet. After this, the nanoparticles were washed three times with deionized water to remove excess salt.

3.3.3 Synthesis of cobalt zinc ferrite (CZF) nanoparticles coated with APTES

CZF coated with APTES were synthesized by hydrothermal approach.

Synthesized bare nanoparticles (10 mL) and sodium hydroxide (6.25 mL) were mixed and stirred for 10 minutes on a magnetic stirrer, after which the solution was added to pressurized reaction vessel containing APTES (2.5 mL). The reaction vessel was then sealed and pressurized at 130 °C for 3 hours to avoid the solvent evaporation. At the end of the reaction period nanoparticles were cleaned three times with deionized water.



Figure 3.5 Surface modification of CZF nanoparticle to CZF-APTES

3.3.4 SI-ATRP polymerization of NIPAM on APTES coated cobalt zinc ferrite nanoparticles

APTES coated nanoparticles were Schlenk flask and allowed to dry in a vacuum oven at 60 °C. Anhydrous propanol and HPLC grade water in ratio 3:1 v/v along with 0.5436 g of NIPAM were then added to the flask. The solution was vortexed and sonicated for 1 minute before performing three freeze-pump-thaw cycles. 2,2-bipyridyl (16.2 mg) and copper(I) bromide (8.6 mg) were added quickly to the frozen flask containing solution, followed by two freeze-pump-thaw cycles and 10 minutes of sonication. The final solution was stirred for 2 hours at room temperature in the presence of nitrogen atmosphere. At the end of two hours, nitrogen supply was cut off and solution was exposed to air. The particles were then washed (3 times) with deionized water to obtain PNIPAM coated nanoparticles for further characterization purposes.

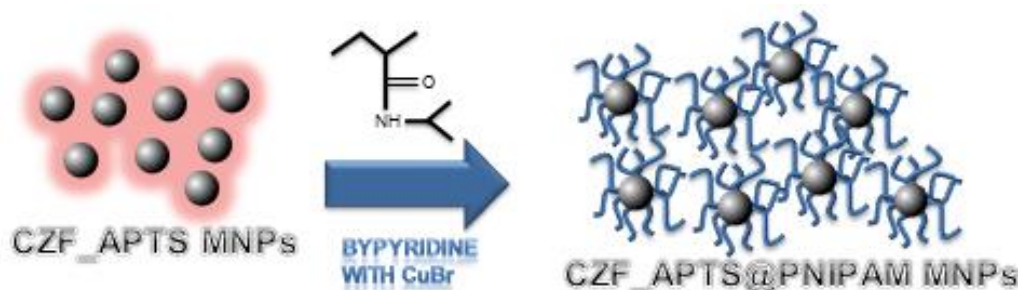


Figure 3.6 Polymerization of PNIPAM from the surface of CZF-APTES

3.3.5 Characterization

CZF, CZF-APTES and CZF-APTES@PNIPAM nanoparticles were characterized using different techniques like x-ray diffraction analysis (XRD), attenuated total reflection – Fourier transform infrared spectroscopy (ATR-FTIR), dynamic light

scattering (DLS), thermogravimetric analysis (TGA), transmission electron microscopy(TEM), and magnetic force microscopy (MFM).

Structure characterization of the CZF nanoparticles was performed by X-ray diffraction (XRD) technique using Rigaku X-ray diffractometer (model Ultima III). The radiation generated diffraction patterns from the samples over a 2θ range (10° to 90°) at ambient temperature.

ATR-FTIR spectroscopy was used to confirm the chemical transformations involved in adding the APTES modification to the surface of the CZF nanoparticles, as well as the polymerization of PNIPAM. To perform this analysis a Miracle-ATR accessory (Pike Technology) with a diamond-ZnSe crystal was used in a Nicolet 6700 FTIR spectrophotometer (ThermoElectron Corporation). Omnic software (v8.1.10, 1992-2009, ThermoFisher Scientific Inc.) configuration of deuterated triglycine sulfate (DTGS) detector, KBr beam was used to collect a minimum of 256 scans per sample. A droplet from the samples was placed on the crystal surface and allowed to dry in order to form a thin film of nanoparticles on the crystal.

To measure the size and distribution of the nanoparticles, dynamic light scattering analysis was done using a ZetaPALS analyzer (Brookhaven Instruments Corporation, BIC) with a laser wavelength of 659 nm at an angle of 90 degrees. Data analysis was done using the BIS software (v2.0). Sample preparation involved two steps, sonication for 2 minutes and stabilization in the cuvette for 3 minutes. Ten measurements (5 min per measurement) were taken to determine the particle size using the mean diameter and standard deviation.

A JEOL 2100 200 kV transmission electron microscope (TEM) was utilized to characterize the morphology and size of nanoparticles. Samples preparation included dispersion in deionized water, sonication in ultrasonic bath for 5 minutes, and deposition on a carbon Formvar Cu grid (Electron Microscopy Science). Samples were then dried before imaging.

Atomic and magnetic force microscopy (AFM / MFM) were conducted on the nanoparticle samples using a Dimension Icon Veeco-Bruker operated in tapping mode and ScanAsyst model was used to collect data. Samples were prepared by drying overnight on the glass slides. MESP probes from Veeco (77.69 kHz resonant constant, 60 kHz drive frequency) were utilized with a 100 nm lift scan height for all measurements to be consistent. Images were collected at a minimum of three different spots for each samples to make sure collected images with consistent across the sample.

3.4 Results and Discussion

To confirm the synthesis of cobalt-zinc ferrite nanoparticles, XRD pattern was observed at room temperature which is shown in the Figure 3.7. All the peaks were matched with reference files JCPDS card number 22-1086 of the CoFe_2O_4 and JCPDS card number 22-1012 of the ZnFe_2O_4 . Peaks at 311 cm^{-1} and 422 cm^{-1} indicate the spinel structure formed thus confirming the perfect match of XRD patterns.^{211,261}

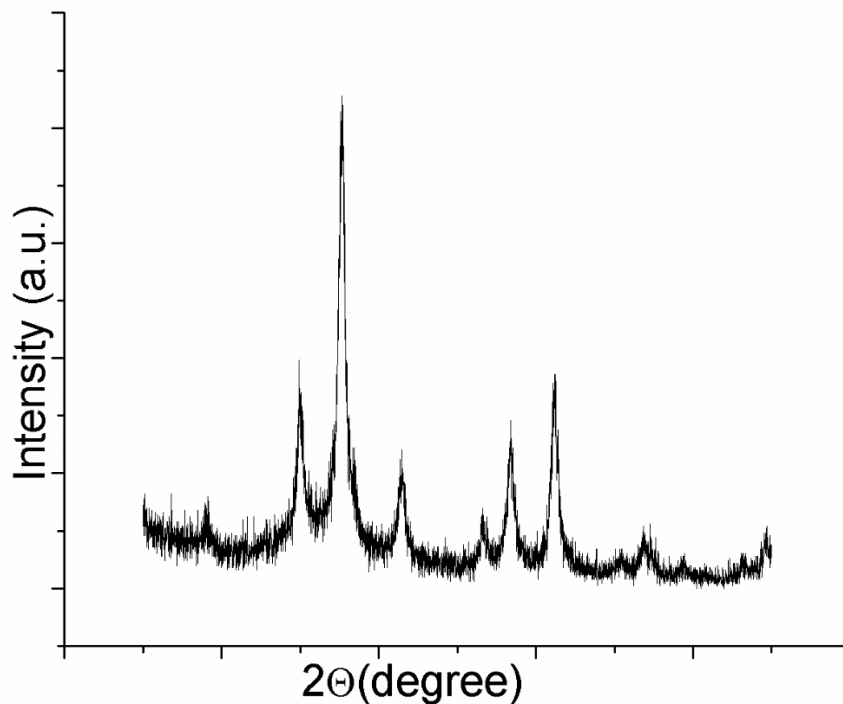


Figure 3.7 XRD pattern for CZF (bare) particles

The bare cobalt zinc ferrite (CZF) nanoparticles were modified twice. First, APTES was added as a monolayer in order to add amine functional groups to the surface of the CZF. Second, the amine groups provided by the addition of APTES allowed for the reaction of the polymerization initiator to the CZF surface such that PNIPAM could be grafted from the CZF. The chemical changes associated with the surface modification reactions were monitored and confirmed with ATR-FTIR analysis. The adsorption of silanol onto the surface of cobalt-zinc ferrite particles was confirmed by bands at 1110 cm^{-1} assigned to the stretching vibration of Si–O bond. The band at 1625 cm^{-1} can be ascribed to the NH_2 bending mode of free NH_2 group introduced from the APTES.²⁶² The presence of the anchored propyl group was confirmed by C–H stretching vibrations that appeared at 2927 and 2865 cm^{-1} . The grafting of PNIPAM was confirmed by the

characteristic peaks at 1647 cm^{-1} and 1558 cm^{-1} that correspond to C=O stretching of amide secondary and N-H stretching of amide secondary of PNIPAM,²⁶³ respectively as shown in Figure 3.8.

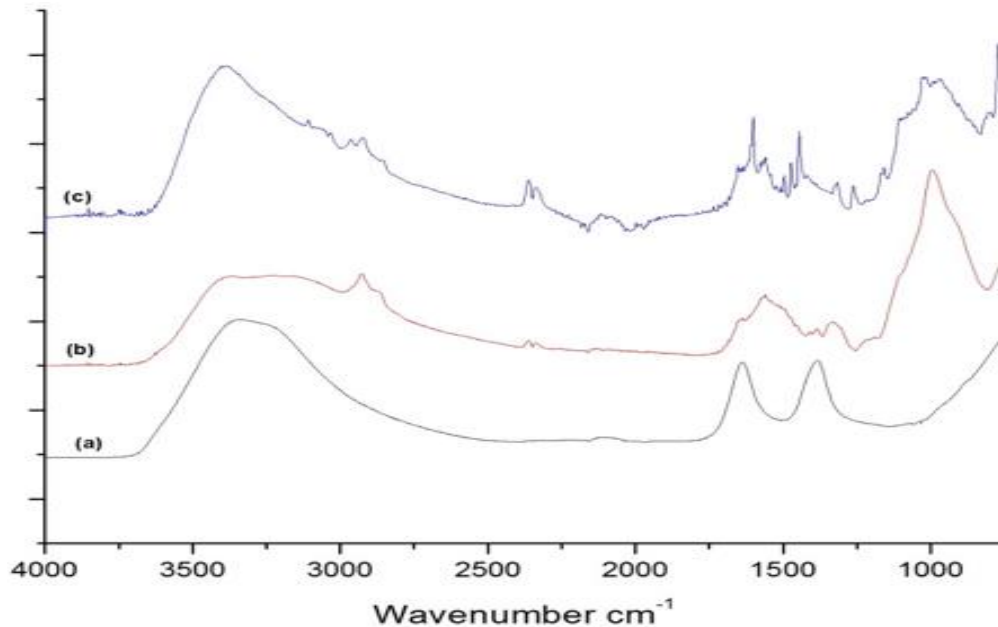


Figure 3.8 FTIR pattern for CZF (a), CZF-APTES (b), and CZF-APTES@PNIPAM (c)

Atomic and magnetic force microscopy (AFM/MFM) was done for all the samples to determine the phase and surface morphology of the samples. Figures 3.9-3.11 (b,c,d) show AFM/MFM the images for height sensor, normal phase and magnetic phase for each samples respectively. The morphology and particle size predicted by DLS testing is confirmed by the TEM images as shown in Figures 3.9 - 3.11a. It is being clearly seen from magnetic phase image of CZF and CZF-APTES has distinctive magnetic regions showing more magnetic properties compared to CZF-

APTES@PNIPAM which seems to be less magnetic. It can also be assumed from this behavior that the polymer coating of PNIPAM might have reduced the magnetic property of the composite particle due to which it shows the reduction in magnetization. Also, CZF and CZF-APTES shows globular height sensor image whereas the thermo-responsive coated CZF-APTES@PNIPAM has larger domains.

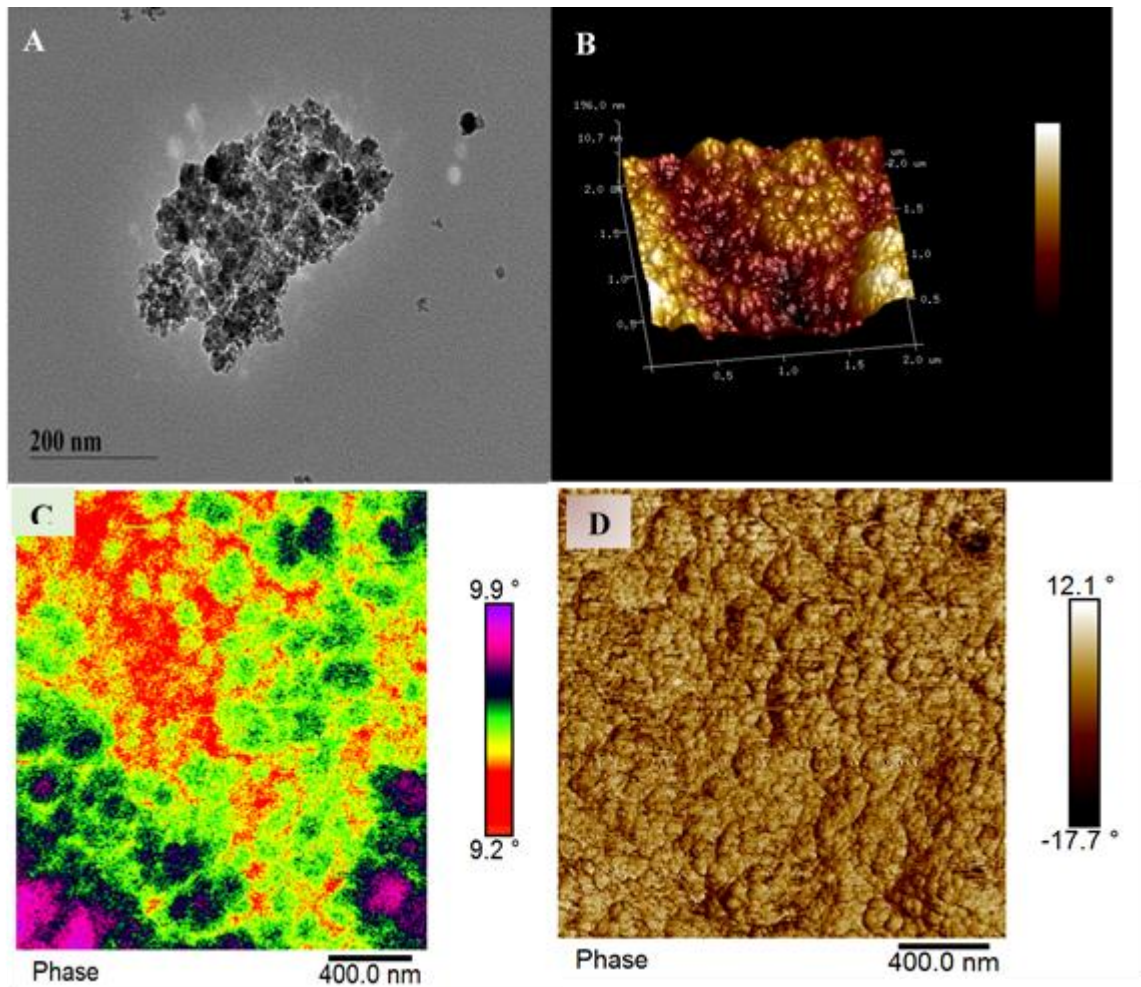


Figure 3.9 TEM (A), AFM topography (B), MFM phase (C), and AFM phase (D) images for neat (bare) cobalt zinc ferrite nanoparticles

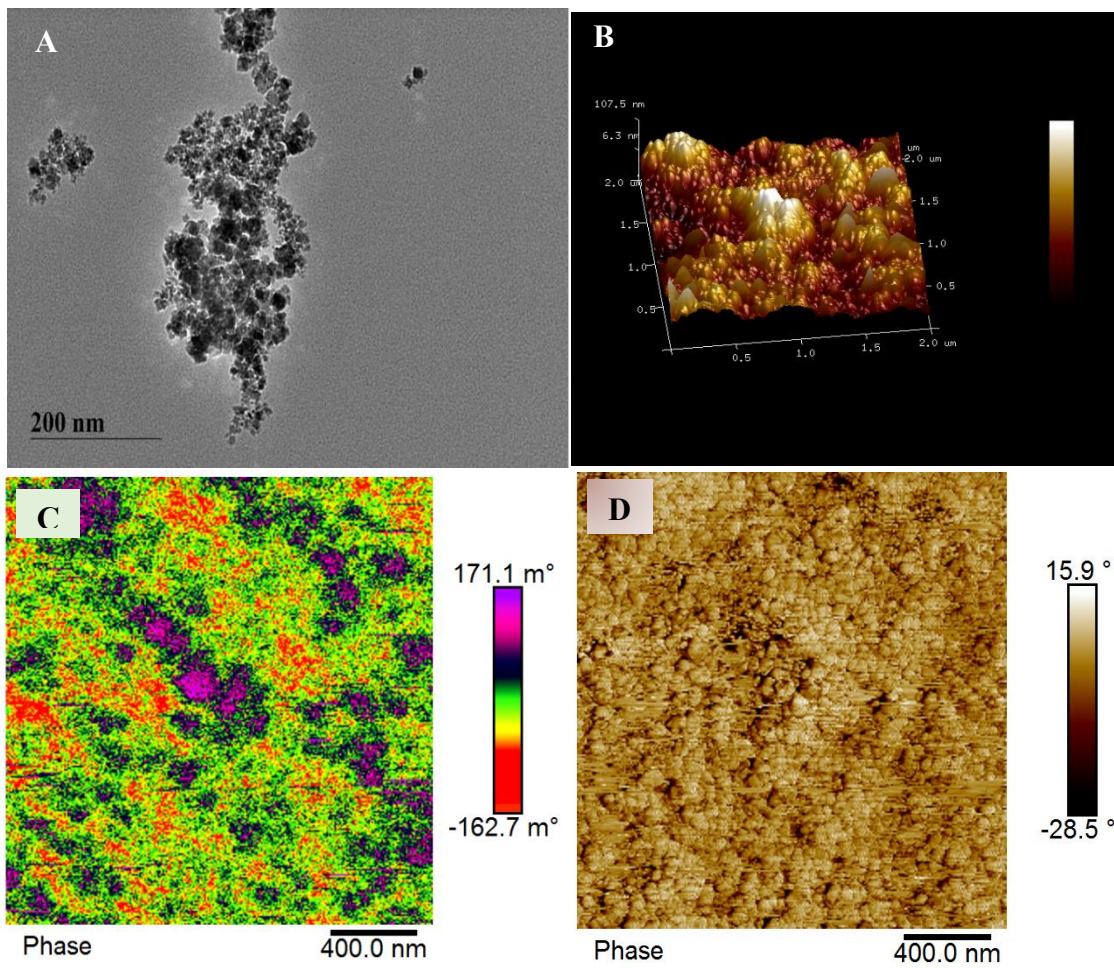


Figure 3.10 TEM (A), AFM topography (B), MFM phase (C), and AFM phase (D) images for CZF-APTES

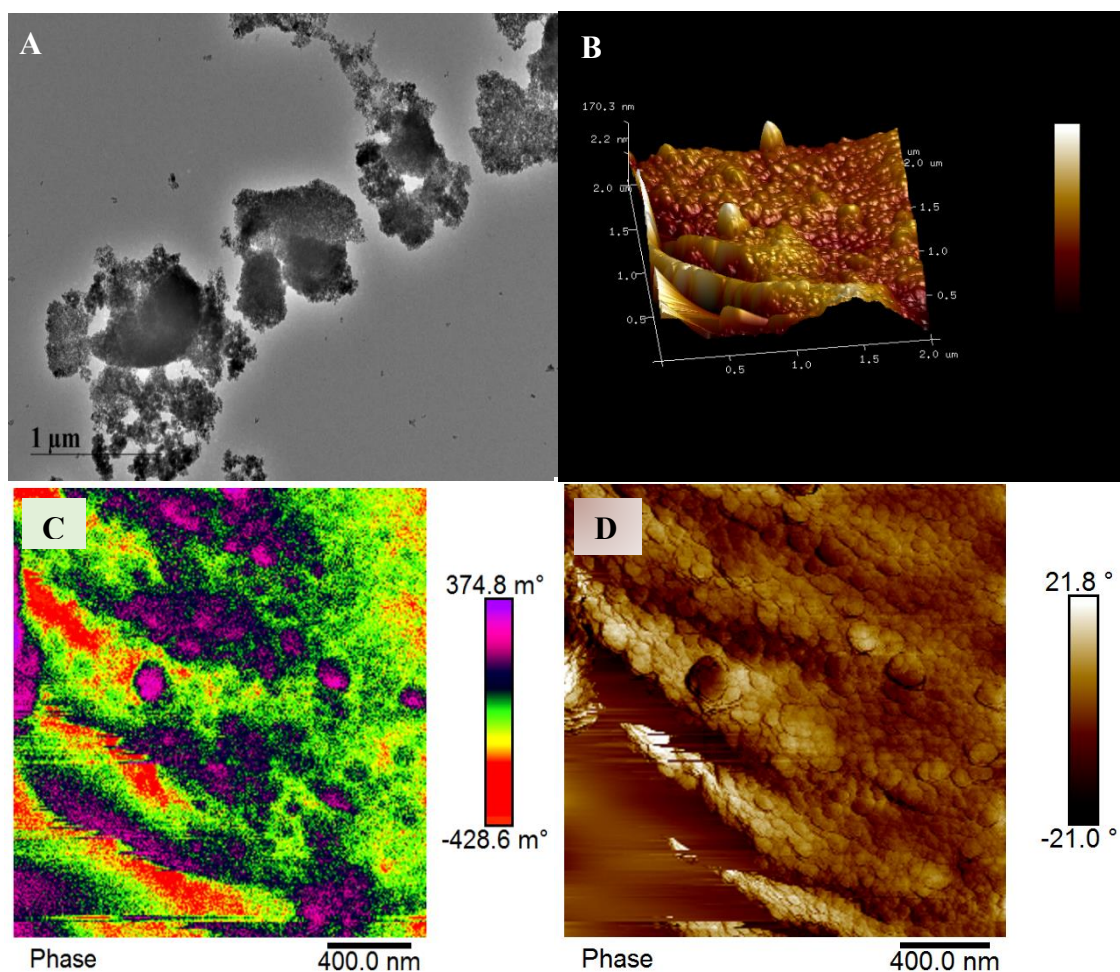


Figure 3.11 TEM (A), AFM topography (B), MFM phase (C), and AFM phase (D) images for CZF-APTES@PNIPAM

For evaluating the potential of cobalt-zinc ferrite nanoparticles as thermo responsive nano-composite and its use in biomedical applications, DLS measurements were collected at temperatures between 20-40 °C. Two phase transition was observed around 31 °C and at 39 °C, respectively, as can be seen in Figure 3.12. A ~29 % reduction in size was observed due to the tighter packing of PNIPAM blocks. The CZF-APTES@PNIPAM is swollen at lower temperatures and then collapses around lower

critical solution temperature (LCST). This LCST stimulus could be manipulated to allow for drug release and partitioning²⁶⁴ (due to change size) of the polymer-grafted MNPs. This rapid thermo responsive swelling and deswelling is due to changes in the hydrophilic/hydrophobic solubility of the polymer.

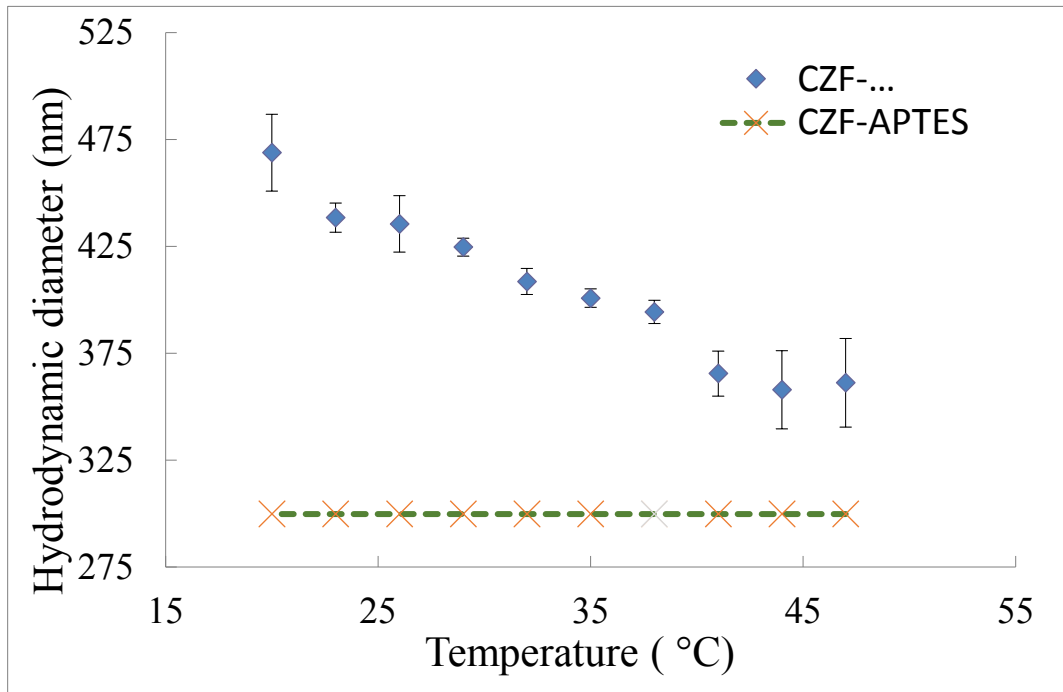


Figure 3.12 Hydrodynamic diameter temperature dependence of CZF-APTES and CZF-APTES@PNIPAM nanoparticles.

3.5 Conclusions

Thermo-responsive polymer PNIPAM was successfully grown from the surface of cobalt-zinc ferrite nanoparticles. The chemical composition was demonstrated by ATR-FTIR and size as well as morphology was observed by TEM. DLS was used to demonstrate a LCST of 32 °C for this composite which is close to expected value of PNIPAM. This composite having magnetic properties along with stimulus can be used in

applications such as controlled drug delivery and similar biomedical applications. Further study will reveal other thermo-responsive polymers having similar characteristics for other applications.

CHAPTER IV
SYNTHESIS AND CHARACTERIZATION OF TEMPERATURE AND PH
RESPONSIVE NANOCOMPOSITES PIA-*b*-PNIPAM@Fe₃O₄

4.1 Abstract

Stimuli responsive polymers (SRPs) have been of great interest in the last few decades because of their tremendous potential in biomedical and environmental applications. When SRPs are grafted from magnetic nanoparticles, these multi-functional nanocomposites can be utilized for complex applications such as targeted drug delivery, advanced separations and magnetic resonance imaging. In this study, a one-step 3-aminopropyltrimethoxysilane (APTES) hydrothermal approach was used to synthesize APTES modified Fe₃O₄ nanoparticles (APTES@Fe₃O₄) with reactive terminal amine groups. Via two successive surface initiated atom transfer radical polymerizations (SI-ATRP), pH and temperature responsive polymer blocks, PIA-*b*-PNIPAM@Fe₃O₄ were grown on the surface of poly(itaconic acid)-*b*-poly(N-isopropyl acrylamide). These polymers grafted nano-magnetic particles were characterized to confirm the chemical composition and determine how particle morphology, size distribution, and charge for these SRP-based nanocomposites change in response to ambient pH and temperature stimuli using transmission electron microscopy (TEM), light scattering, zeta potential, and Fourier transform infrared spectroscopy (FTIR). Results showed that the synthesis

was successful, with the $\text{Fe}_3\text{O}_4@ \text{PIA-}b\text{-PNIPAM}$ showing temperature and pH sensitivity.

4.2 Introduction

Polymers in today's world not only improve material properties, but also form smart and stimuli responsive material. Robust coating techniques which evolved from the growth of polymers carry immense potential for research and industrial applications ranging from nanotechnology to biomedical applications. These stimuli responsive polymer can be tailored to respond to environment changes like temperature, pH, magnetic & electric field and applied mechanics^{67,265–268} expanding their applications areas to fields like medicine, biosensors, drug delivery, image targeting, tunable catalysis, self-healing materials, and colloids.^{169,265,269–280} The stability of nanoparticles in solution is important to their successful use, as so surface modification methods are used to promote stability. One approach is the modification of the surface with a covalently bonded small molecule, such as 3-aminopropyltrimethoxysilane (APTES), which provides a terminal reactive site for further modification and can be applied with a hydrothermal approach that is advantageous due to the little time required.²⁸¹ Stimuli responsive polymers (SRPs) can then be grafted from these magnetic nanoparticles.

PNIPAM is a one of the most applicable stimuli responsive polymer useful for biomedical purposes due to its 32 °C lower critical solubility temperature (LCST),²⁸² which falls within the physiological human body temperature range. PNIPAM shows hydrophobic behavior (chains collapse) above LCST and hydrophilic (chain expansion) below LCST. One such other pH-responsive polymer is polyitaconic acid (PIA) which contains two carboxylic acid group, each with a different pKa value making it a weak

polyelectrolyte.²⁸³ The increased adhesion and latex stability of PIA are a result of the two carboxylic groups forming copolymer with effective acidity.²⁸⁴ System containing these smart polymers give a non-linear response to external signals, displaying a unique property which can be utilized by tuning the architecture, monomer sequence, and chemical composition for specific applications.

In this study, surface initiated ATRP was used to form SRPs with iron oxide magnetic nanoparticle grafted to pH- sensitive itaconic acid block thermally responsive poly(N-isopropylacrylamide) block with well controlled molecular weight, chemical composition, and architecture.^{285–288} To avoid overlapping of neighboring chains, one end of polymer chains stretches to increase the size of the polymers in solution whereas the other end is confined to the reactive site of the iron oxide nanoparticle. The SRP-based nanocomposites formed in this study are ideal for on-going drug delivery systems under investigation. This work is similar to the previous work except that instead of commercially available nanoparticles, iron oxide nanoparticles were synthesized in the lab to avoid breakage and aggregation as encountered before.²⁸⁹

4.3 Experimental Section

4.3.1 Synthesis of APTES modified magnetic nanoparticles

A solution containing 7.75 mL of deionized water along with 1.25 g of iron (II) chloride hydrate was stirred at 300 rpm for 10 min while slowly adding 6.25 mL of ammonium hydroxide. This solution along with 2.5 mL of APTES was added to a hydrothermal reactor and sealed. The reactor was inserted in an oven preheated at 134 °C and held for three hours. The solution was washed with deionized water (X 3) and ethanol (X 2) over a 2T magnet. After sonicating the cleaned solution, APTES-Fe₃O₄ was

dispersed in water at concentration of 1mg/mL. Dynamic light scattering was performed on APTES- Fe₃O₄ the final product to measure the particle size and size distribution.

4.3.2 Surface-initiated block copolymerization of itaconic acid (IA) and N-isopropylacrylamide (NIPAM)

An aliquot of amine functionalized iron oxide nanoparticles (APTES- Fe₃O₄) (0.25 mL) in aqueous solution was dried under vacuum in a Schlenk flask, to which 1 mL of trimethylamine (83.6 μL, 0.6 mmol) was added at ~ 0 °C. 5 mL of 2-bromopropionyl bromide (52.4 μL, 0.5 mmol) was then added dropwise to the solution and stirred overnight at room temperature. Bromine initiated nanoparticles were isolated using a 1.32 T magnet, washed with ethanol, sonicated three times and dried under vacuum at room temperature. A 1 M solution of itaconic acid (IA) (2.602 g, 20 mmol) and HPLC water (15 mL) was deprotonated with NaOH (1.64 g) to adjust pH to 7. This was followed by addition of 2,2-bipyridyl (bpy) (62.5 mg, 0.4 mmol) and anhydrous 2-propanol (5mL) and sonication for 10 min. Dissolved oxygen was extracted by implying three freeze-pump-thaw cycles. Two more freeze-pump-thaw cycles were done after adding Cu (I) Br (28.7 mg, 0.2 mmol) to the frozen state of the solution. The solution was then left for 13 hours to polymerize. The PIA-grafted nanoparticles were cleaned with water (3 times) and allowed to settle under the influence of a magnet. The nanoparticles were then dried under vacuum followed by addition of NIPAM (2.263 g, 20 mmol), and anhydrous 2-propanol/HPLC water (3:1. v/v, total volume 20mL). 2,2 bipyridyl (bpy) (62.5 mg, 0.4 mmol) and Cu(I) Br (28.7 mg, 0.2 mmol) were quickly added to the mixture after three freeze-pump-thaw cycles. Two additional freeze-pump-thaw cycles were done to degas the mixture before sonication (10 min). Polymerization was done for 6 hours, after which

the solution was exposed to air and PIA-b-PNIPAM- grafted nanoparticles were separated using a magnet. To remove remaining catalyst, unreacted monomer, and ungrafted polymers, the nanoparticles were washed three times by water and ethanol and dried under vacuum.

4.4 Characterization

The synthesized APTES nanoparticle and polymer modified-magnetic nanoparticles were characterized by ATR-FTIR spectroscopy using a dry air-purged Thermo Electron 6700 instrument with a mercury- cadmium-telluride (MCT-A*) detector and a KBr beam splitter using Omnic software (v8.1.10, Thermo Fisher Scientific Inc.). A MIRacle-ATR (Pike Technologies) with ZnSe/diamond crystal was used to collect spectra over the wavenumber range of 800-4000 cm^{-1} with the resolution of 4 cm^{-1} and 256 scans. The samples were deposited as a solution droplet, allowing it to dry on the crystal surface leaving a thin nanoparticle film.

A ZetaPALS analyzer (Brookhaven Instruments Corporation, BIC) with a laser wavelength of 659 nm was used to measure the mean particle size and size distributions of the polymeric nanoparticle in water. Particle size was measured at a 90° angle. Prior to measurements, the samples were sonicated for 5 min and then allowed to stabilize in the cuvette for 3 min prior to data collection. A total of 5 measurements (5 min per measurement) were carried out for particle size determination using the effective diameter. BIC Particle Solutions software (v2.0) was utilized for data collection and analysis.

Transmission electron microscopy (TEM) was performed using a JEOL 100CXII at 100 kV and high-resolution images were obtained using a JEOL 2100 at 200 kV.

Sample droplets were placed on a carbon Formvar Cu grid (Electron Microscopy Science), and the solvent evaporated at ambient temperature inside a ventilated hood. Nanoparticle was sonicated in an ultrasonic bath for 5 min and then one droplet was put on copper grid to air dry.

4.5 Results and Discussion

The APTES coating on the $\text{Fe}_3\text{O}_4@$ APTES NPs was confirmed by FTIR spectrometry (Figure 1). After the coating of APTES onto Fe_3O_4 NPs, the bands at 1084 and 1005 cm^{-1} correspond to the stretching vibration of the Si–O bond, and the band at 1129 cm^{-1} is due to the stretching vibration of the C–N bond. The presence of aminosilane on the surface of the as received $\text{Fe}_3\text{O}_4\text{-NH}_2$ nanoparticles was confirmed by the absorption bands at 3389 cm^{-1} and 1095 cm^{-1} that correspond to the N-H stretching of the -NH_2 group and Si-O-Si stretching vibrations. The peaks at 1635 cm^{-1} and 1513 cm^{-1} in the Fe_3O_4 -PNIPAM sample are characteristic for PNIPAM and correspond to the C=O stretching of amide secondary and N-H stretching of amide secondary, respectively.

The mean diameter size calculated by DLS is 208 ± 2 nm for $\text{Fe}_3\text{O}_4@$ APTES nanoparticles. After grafting from poly(itaconic acid) the size was shown to be 880.948 ± 8.18 nm and finally $\text{Fe}_3\text{O}_4@$ PIA-*b*-PNIPAM was 1164 ± 63 nm. All the DLS data are in good agreement with TEM images of nanoparticles before and after surface modification (Figure 4.1).

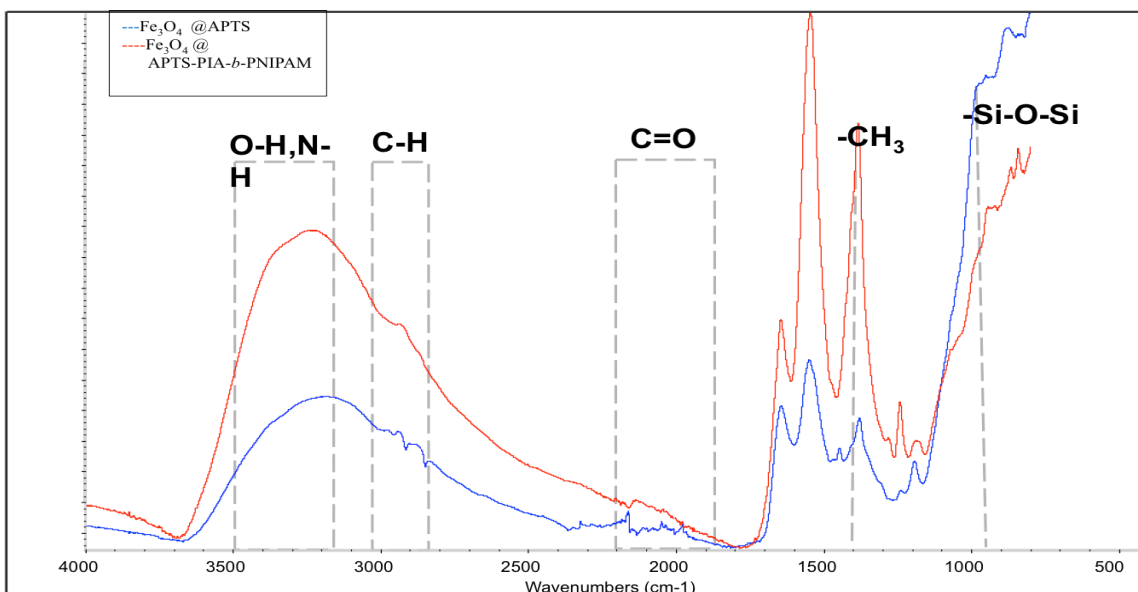


Figure 4.1 Representative FTIR spectra of APTES@Fe₃O₄ nanoparticles (blue spectrum) and PIA-b-PNIPAM@Fe₃O₄ (red spectrum)

The morphology of neat iron oxide particles and surface modified SRP were analyzed using TEM after two sequential SI-ATRP reactions. First, the itaconic acid homopolymerized on APTES@Fe₃O₄ was confirmed (Figure. 4.2b) as seen to be hazy around the magnetic iron oxide nanoparticles. Second, was the block copolymer formed as Fe₃O₄@PIA-b-PNIPAM after subsequent polymerization of NIPAM as shown at two magnifications (Figure. 4.2 c,d). The dark spherical core is iron oxide nanoparticle surrounded by light spherical copolymer with particle size of about 1100 nm.

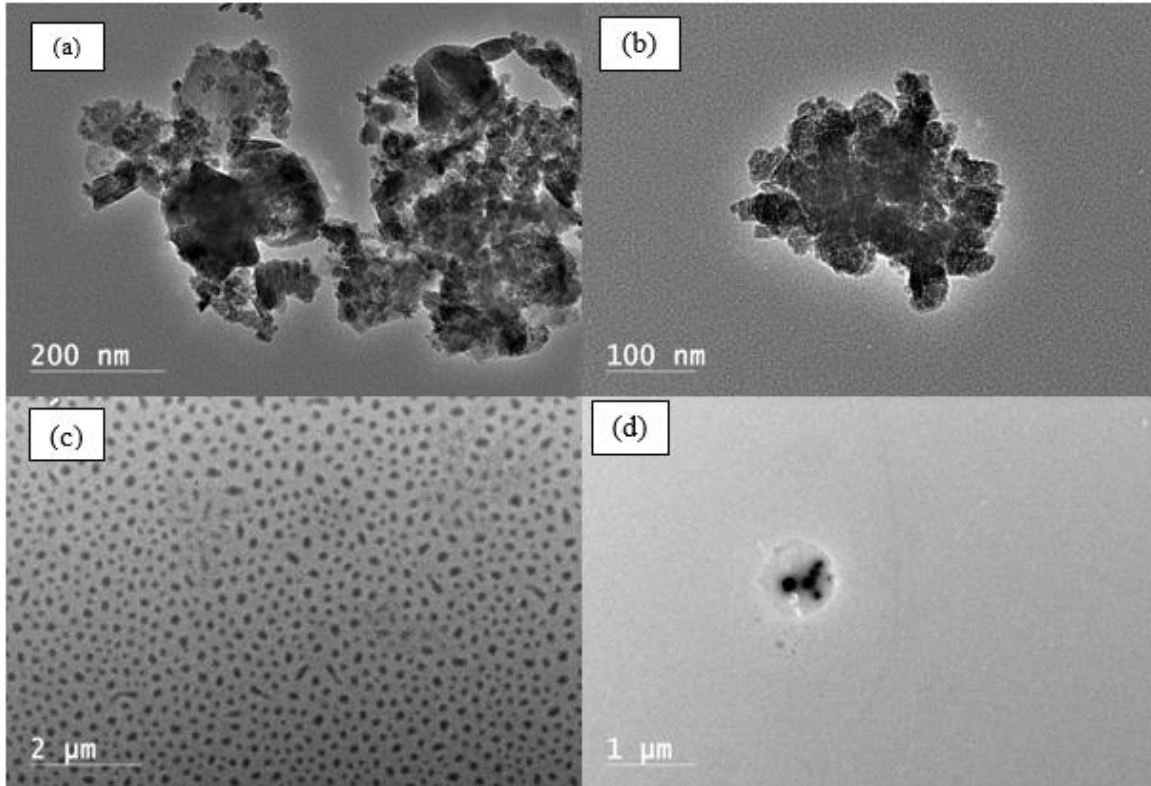


Figure 4.2 TEM image of $\text{Fe}_3\text{O}_4@\text{APTES}$ (a), $\text{Fe}_3\text{O}_4@\text{PIA}$ (b) and $\text{Fe}_3\text{O}_4@\text{PIA-b-PNIPAM}$ (c,d)

DLS measurements were performed to obtain the size distribution of modified nanoparticles in water and their thermo as well as pH responsive behavior. Since the LCST of PNIPAM is known to be $32\text{ }^\circ\text{C}$, the measurements were conducted from $25\text{ }^\circ\text{C}$ to $45\text{ }^\circ\text{C}$. Figure 4.3 shows the dependence of effective diameter of nanoparticle with polymer on pH solution and temperature. A high of 45% decrease in hydrodynamic diameter was observed in neutral pH solution over the measured temperature range, followed by 32.32% decrease in pH 2 solution, 14.35% decrease in pH 12 solution, a low of 1.49% decrease in pH 4 solution and an increase of 12.32% in pH 10 solution. It can be also seen that for constant pH less than 10, increasing the temperature brings about

reduction in the effective diameter. Value of pH=10 proved to be a critical point after which the effective diameter is not affected by temperature.

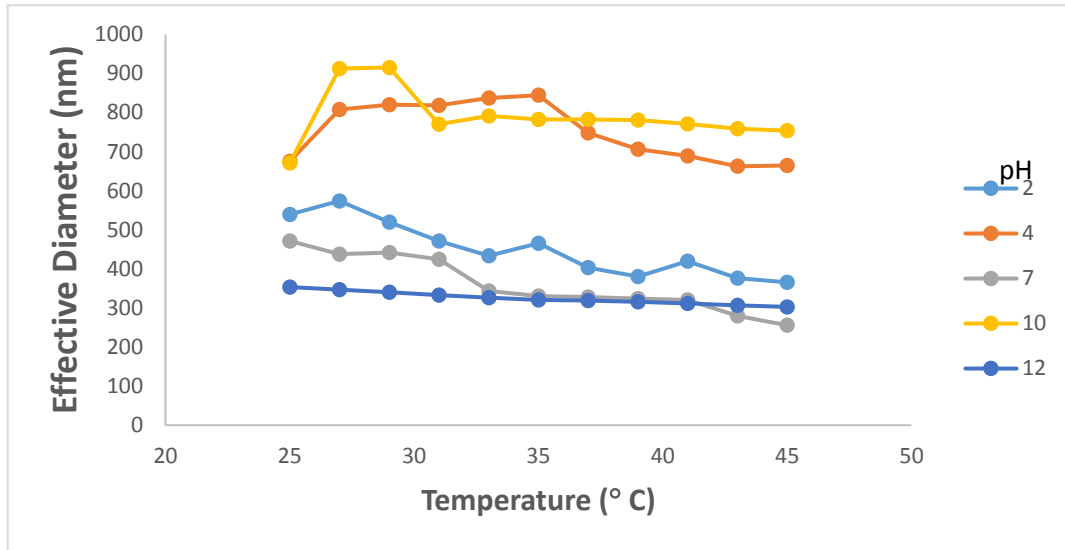


Figure 4.3 Effective diameter temperature and pH dependence of the Fe₃O₄@PIA-*b*-PNIPAM stimuli responsive polymer

4.6 Conclusions

We have synthesized APTES-coated Fe₃O₄ NPs with a mean diameter of 208.54 nm using a hydrothermal process. The structure, morphology, composition, and surface properties of the formed particles were characterized by TEM, FTIR, and dynamic light scattering measurements. A pH- and thermo-responsive block copolymer comprised of PIA and PNIPAM was successfully polymerized from the surface of nanoparticles. FTIR, TEM, and DLS was used to characterize the polymers. According to the DLS and TEM results, the modified MNPs were well dispersed and stable in water as well as some organic solvents. It was shown that temperature affected the effective diameter of

nanoparticle with polymer negatively at a constant pH value. For $\text{pH} \geq 10$, effective diameter remained relatively unaffected with an increase in temperature. In particular, these dual thermo and pH-responsive polymers can be used in smart drug delivery and other biomedical applications.

CHAPTER V

STUDY THE PARTICLE BREAKAGE OF MOSAIC NANOPARTICLES

5.1 Abstract

Knowledge of operational thermal boundaries for modified magnetic nanoparticles is vital to safe implementation. The stability of mosaic-type magnetic nanoparticles is important to determine processing and usage specifications; therefore, it is important to understand effects of thermal condition. Surface functionalized MNPs do not aggregate. The silicate coating surrounding the MNPs, like any coating, degrades with elevated temperature. Fracturing of the aggregation-inhibiting coating results in agglomeration of particles. This agglomeration is driven by the magnetic attraction between nanoparticle clusters and is definitively noted by a sharp increase in particle size. In this study, experiments to impose thermal fatigue were performed, such as reflux heating, hydrothermal heating, modulated differential scanning calorimetry (MDSC), and thermogravimetric analysis (TGA). Conditions yielding particle breakage were recorded for each thermal treatment, and these findings were supported by further testing with dynamic light scattering (DLS) and transmission electron microscopy.

5.2 Introduction

Magnetic nanoparticles are used for a wide number of applications, such as drug delivery, materials separations, energy harvesting, and electronic displays.²⁹⁰⁻²⁹² When these type of particles are surface-functionalized, a core-shell structure nanoparticle is

produced. Different inorganic/organic shells including silica, various polymers, oleic acid, and others are used to avoid aggregation, allow dispersion in polar/non-polar media, and produce stable particle size distributions. When various nanoparticles cores are used, including magnetic nanoparticles such as magnetite and maghemite, mosaic/multicore nanostructures are synthesized.²⁹³

While mosaic magnetic nanoparticle structures have shown promise for biomedical applications,²⁹⁴ fluorescence,²⁹⁵ MRI,²⁹⁶ and hyperthermia,²⁹⁷ little is known about their thermal stability and maximum operational parameters before these mosaic nanoparticles undergo breakage. Commercially available nanoparticles were initially used for stimuli responsive polymers and oscillating heat pipe experiment as done in previous chapters. The major benefit associated with commercial nanoparticles are they are monomers, have very low polydispersity and readily available for use whereas the major disadvantage is particle breakage during reaction process under conditions like sonication, reflux, and high temperature.²⁹⁸ This particle breakage results in nanoparticles coagulation and lump formation. This lump formulation hinders incorrectly interpreting the results of the polymerization process.

Magnetic nanoparticles (MNPs) are coated with different chemicals to avoid agglomeration. These groups of particles are surface-functionalized, resulting in a core-shell structure. Different inorganic/organic shells including silica, various polymers, oleic acid, and others are used to avoid aggregation, allow dispersion in polar/non-polar media, and produce stable particle size distributions.²⁹⁹ When various nanoparticle cores are used, including MNPs such as magnetite and maghemite, mosaic/multicore nanostructures are synthesized. In this study, modified nanoparticles are comprised of

multiple magnetite (Fe_3O_4) single-core nanoparticles encapsulated within a silicate shell that is then functionalized with amine, chitosan, or silanol functional groups. Little is known about the specific ranges of thermal stability before modified surface layers undergo breakage. The effects of elevated temperatures have been observed in order to accurately assess the structural and chemical stability of these core-shell magnetic nanostructures before, during, and after thermal treatments. This study evaluates limiting temperatures for modified MNPs to guide in their safe implementation in any area.

The utility of MNPs stem from their ability to flow, but rupture of the outer coating results in severe aggregation, thus limits the flow. For most biomedical uses, MNPs are inserted into the bloodstream which is known to vary due to hundreds of factors. Fracturing and aggregation of injected MNPs in a bloodstream would result in catastrophic blood clots and poisoning. Avoiding thermal fracture of magnetic nanoparticles is vital to safe implementation.

In this study, mosaic nanoparticles are comprised of multiple magnetite (Fe_3O_4) single-core nanoparticles encapsulated within a silicate shell that is then functionalized with amine, chitosan, or hydroxyl functional groups. Different temperatures, time at each temperature, and thermal cycling under different processes have been evaluated to assess the dimensional and chemical stability of these core-shell magnetic nanostructures before and after thermal treatments. This study evaluates optimum processing and usage conditions for magnetite mosaic-nanoparticles to guide in their application.

5.2 Experimental Section

5.2.1 Materials

Silanol 500 nm Dh (Chemicell, GmBH), Chitosan 200 nm Dh (Chemicell, GmBH), Amine 100 nm Dh (Chemicell, GmBH) were used as received without further modification. Water used in all experiments was purified using Millipore (Type I) with a resistivity of 18.2 MΩ cm.

5.2.2 Thermal fracture of magnetic nanoparticles with different coatings

For each nanoparticle sample, a 15 mL dilution was made, yielding a final concentration of 1 milligram nanoparticle solution per milliliter of deionized, high-purity water. Each 15 mL solution was placed in a reboiler set-up, consisting of a round bottom flask resting inside of a hot oil bath. The round bottom flask was connected to a reflux condensing pipe with a nitrogen line blanketing the system. The temperature inside the round bottom flask was measured, and aliquots were drawn. The first aliquot was drawn after the dilution had refluxed for one hour at 80 °C, and the second aliquot was drawn after the dilution had refluxed for one hour at 100 °C. Aliquots were similarly drawn after 1 h refluxing at 120 °C and 130 °C. The aliquots were allowed to cool prior to characterization.

5.2.3 Characterization

Fractured surface modified nanoparticles were characterized several techniques, including dynamic light scattering (DLS), modulated differential scanning calorimetry (MDSC), and transmission electron microscopy (TEM).

Dynamic light scattering analysis was performed to measure the size distribution of the nanoparticles. A ZetaPALS analyzer (Brookhaven Instruments Corporation, BIC) was used, with a laser wavelength of 659 nm at an angle of 90 degrees. Data analysis was done using the BIS software (v2.0). Sample preparation involved sonication for 30 seconds to avoid. Ten measurements (5 min per measurement) were taken to determine the particle size using the mean diameter.

Once a preliminary breakage point was determined, small samples (0.3 mg – 0.7 mg) of solution were placed into hermetically sealed alumina pans. These pans were then inserted into the MDSC unit, and the temperature slowly climbed through the suspected breaking range. Plots of each measurement were created using Universal Analysis.

A JEOL 2100 200 kV transmission electron microscope (TEM) was utilized to characterize the morphology and size of nanoparticles. Samples preparation included dispersion in DI water, sonication in ultrasonic bath for 5 minutes, and deposition on a carbon Formvar Cu grid (Electron Microscopy Science) followed by carbon coating to ensure no damage to the instrument. Samples were then dried before imaging.

5.3 Results and Discussion

Amine functionalized MNP clusters showed initial signs of shell-rupture around 110 °C, as an effect of high temperature. This is evidenced by a large increase in the mean effective diameter for amines post-treatment at 110 °C. A similar fracture point appears in chitosan functionalized MNPs, around 115 °C. In contrast, the silanol functionalized MNPs are incredibly stable from -80 °C to 700 °C, thus no breakage was observed. Figure 5.1 compares the changes in mean diameter for silanol, amine, and

chitosan MNPs, and Figure 5.2 shows a more detailed look at the difference between silanol and amine MNPs.

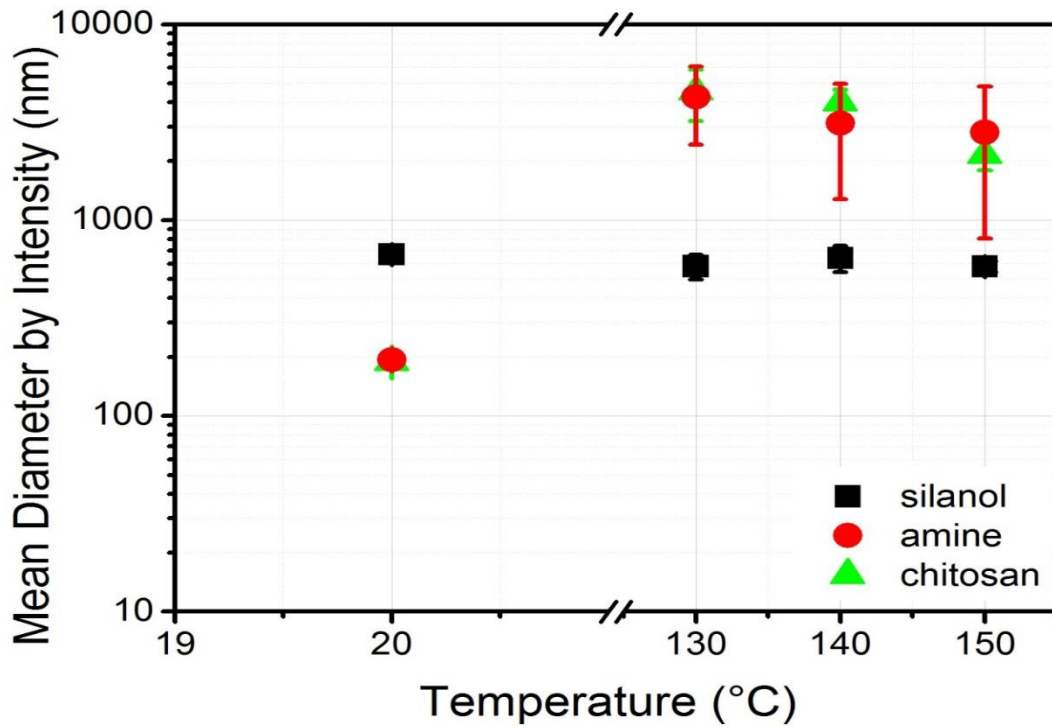


Figure 5.1 Mean diameter shift in amine and chitosan at sub -130 °C

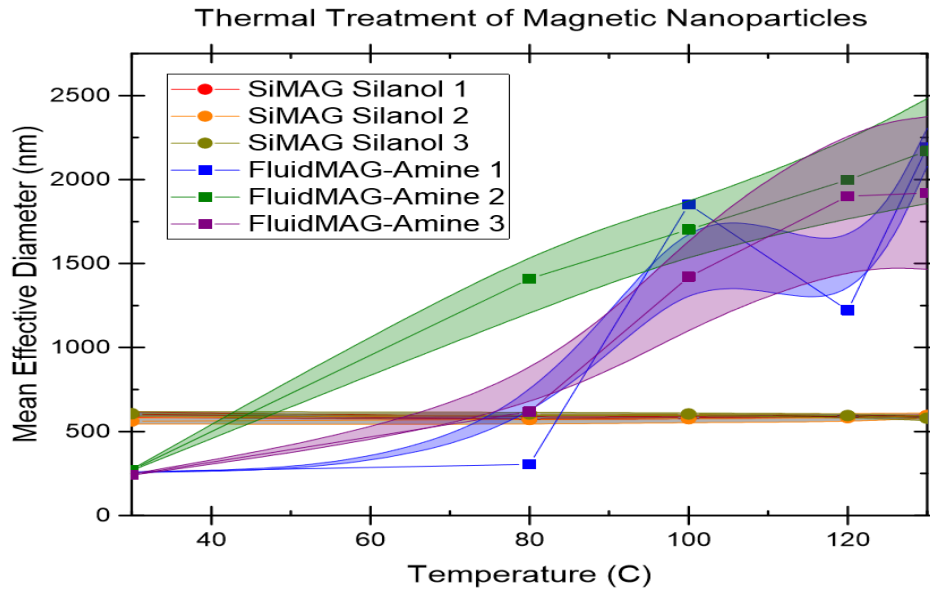


Figure 5.2 Shift in in mean diameter for amine at ≈ 100 °C. Line represents the corresponding mean effective diameter with shaded band as error with 95% confidence.

The proposed breakage point could be more closely analyzed using modulated differential scanning calorimetry. As the particle shells fracture, a significant change in heat flow through the particles should occur. Figure 5.3 depicts this shell rupture in amine functionalized MNPs beginning around 107 °C.

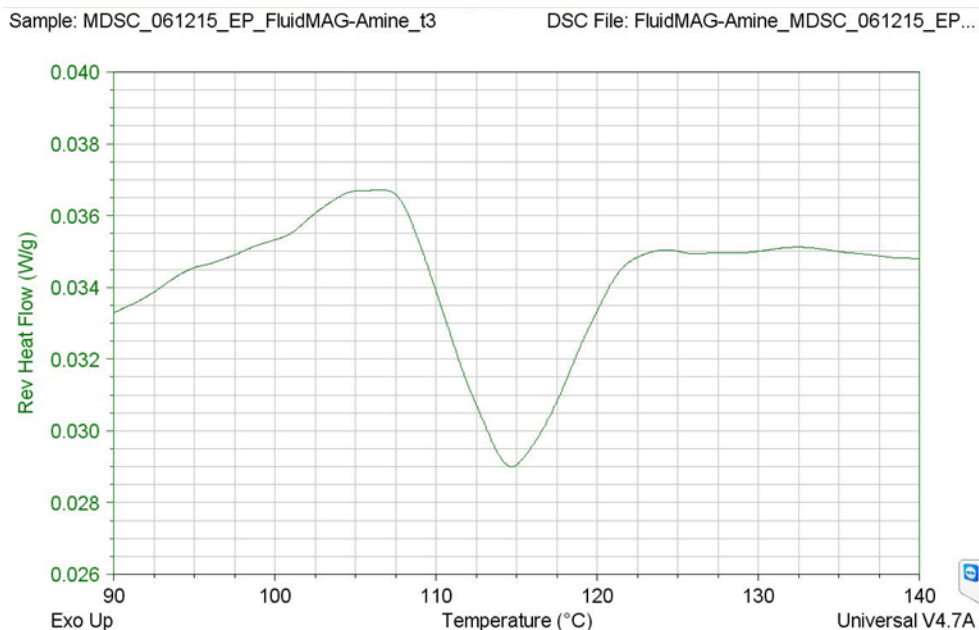


Figure 5.3 Shift in heat flow through amine at ≈ 107 °C

Particle aggregation is directly observed in solutions containing amine functionalized MNPs. Though pre-treatment and post-treatment both contain aggregation, the degree of aggregation, evidenced by particle density and aggregate thickness, is significantly higher in post-treatment samples. Figures 5.4 describe the change in particle density as a result of fractured shells.

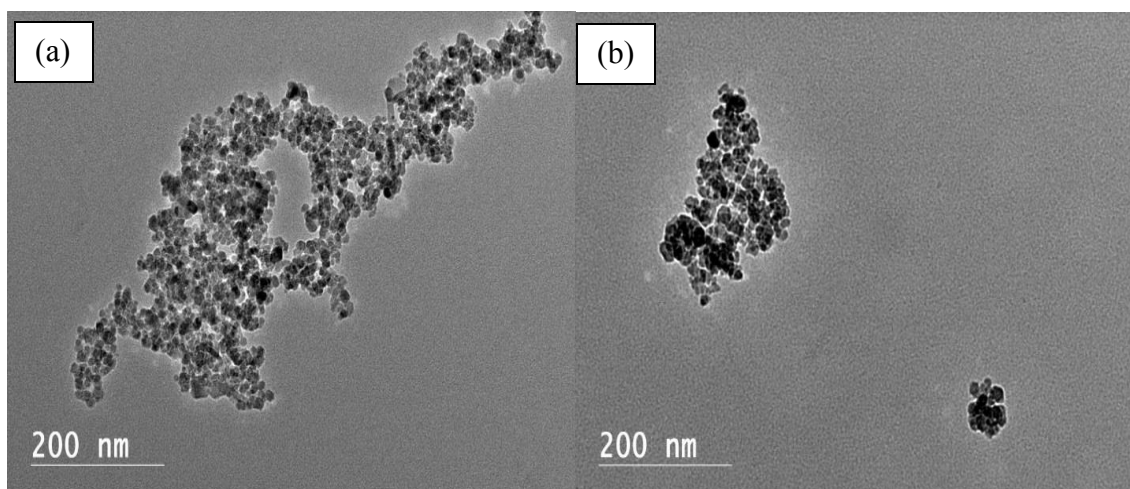


Figure 5.4 TEM image showing particle aggregation

The particles, though aggregated, are spread thin in the pre-treatment sample (a), while the post-treatment sample shows an increase in particle density (b).

5.4 Conclusions

Mosaic/multicore magnetic nanoparticle structures are unstable under different heating treatments. It has been shown that particles are released from the multi-core structure when they are submitted to long sonication periods, and long reflux processes. Single core silanol coated nanoparticles did not show significant changes when submitted to reflux or sonication; however, particle aggregation was observed possibly due to effects on surface stabilizers.

Silanol functionalized MNPs show incredible resistance to fracture due to thermal fatigue. This durability is most likely either due to the coating process for this type of MNP or possibly due to some synergistic effects between the silanol functionalization and the silicate base coating. Regardless of the cause, silanol functionalized MNPs are stable throughout any temperature possibly present in the human bloodstream.

Amine and chitosan functionalized MNPs fracture beginning at 107.5 °C. Though most humans would not naturally elevate blood this high, a very high fever or infection can produce these temperatures in localized region. Additionally, the supplementing of heat from outside the body (from a warm mug, for example, or a space heater) could easily exceed the threshold temperature of 107.5 °C. For this reason, amine and chitosan functionalized MNPs, in the current states and holding current properties, should not be used for any biological injection. As new developments in the production and functionalization of these MNPs emerge, however, retesting should be conducted.

CHAPTER VI

CONCLUSIONS

Seven different ligands were used for surface modification of bare cobalt-ferrite nanoparticles. ATR-FTIR confirmed the successful attachment of ligands to the FF-bare. The size and morphology was studied by TEM and DLS. The breakage of mosaic or multi-core nanoparticles leading to decrease in energy harvesting through OHP was successfully eliminated by replacing it with in-house synthesized cobalt-ferrite nanoparticles. And moreover surface modifying for stability over a longer time. In this study, initial investigation of ferrofluid for voltage measurement was done in a peristaltic pump. After comparing with previous study, FF-CIT was charged to OHP and almost 200% more voltage was harvested.

Thermo-responsive polymer PNIPAM was successfully grown from the surface of cobalt-zinc ferrite nanoparticles. The chemical composition was demonstrated by ATR-FTIR and size as well as morphology was observed by TEM. DLS was used to demonstrate a LCST of 32 °C for this composite, which is close to expected value of PNIPAM. This composite having magnetic properties along with stimulus can be used in applications such as controlled drug delivery and similar biomedical applications. Further study will reveal other thermo-responsive polymers having similar characteristics for other applications.

We have synthesized APTES-coated Fe₃O₄ NPs with a mean diameter of 208.54 nm using a hydrothermal process. The structure, morphology, composition, and surface properties of the formed particles were characterized by TEM, FTIR, and dynamic light scattering measurements. A pH- and thermo-responsive block copolymer comprised of PIA and PNIPAM was successfully polymerized from the surface of nanoparticles. FTIR, TEM, and DLS was used to characterize the polymers. According to the DLS and TEM results, the modified MNPs were well dispersed and stable in water as well as some organic solvents. It was shown that temperature affected the effective diameter of nanoparticle with polymer negatively at a constant pH value. For pH \geq 10, effective diameter remained relatively unaffected with an increase in temperature. In particular, these dual thermo and pH-responsive polymers can be used in smart drug delivery and other biomedical applications.

Mosaic/multicore magnetic nanoparticle structures are unstable under different heating treatments. It has been shown that particles are released from the multi-core structure when they are submitted to long sonication periods, and long reflux processes. Single core silanol coated nanoparticles did not show significant changes when submitted to reflux or sonication; however, particle aggregation was observed possibly due to effects on surface stabilizers.

Silanol functionalized MNPs show incredible resistance to fracture due to thermal fatigue. This durability is most likely either due to the coating process for this type of MNP or possibly due to some synergistic effects between the silanol functionalization and the silicate base coating. Regardless of the cause, silanol functionalized MNPs are stable throughout any temperature possibly present in the human bloodstream.

Amine and chitosan functionalized MNPs fracture beginning at 107.5 °C. Though most humans would not naturally elevate blood this high, a very high fever or infection can produce these temperatures in localized region. Additionally, the supplementing of heat from outside the body (from a warm mug, for example, or a space heater) could easily exceed the threshold temperature of 107.5 °C. For this reason, amine and chitosan functionalized MNPs, in the current states and holding current properties, should not be used for any biological injection. As new developments in the production and functionalization of these MNPs emerge, however, retesting should be conducted.

REFERENCES

- (1) Feynman, R. P. There's plenty of room at the bottom. *Eng. Sci.* **1960**, *23* (5), 22–36.
- (2) Drexler, K. E.; Peterson, C.; Pergamit, G. Unbounding the future. *William Morrow N. Y.* **1991**, 294.
- (3) Schummer, J.; Baird, D. *Nanotechnology challenges: implications for philosophy, ethics and society*; World Scientific, 2006.
- (4) Stix, G. Little big science. *Sci. Am.* **2001**, *285* (3), 26–31.
- (5) El-Sherbiny, I. M.; Smyth, H. D. Biodegradable nano-micro carrier systems for sustained pulmonary drug delivery:(I) self-assembled nanoparticles encapsulated in respirable/swellable semi-IPN microspheres. *Int. J. Pharm.* **2010**, *395* (1), 132–141.
- (6) Trzebicka, B.; Robak, B.; Trzcinska, R.; Szweda, D.; Suder, P.; Silberring, J.; Dworak, A. Thermosensitive PNIPAM-peptide conjugate – Synthesis and aggregation. *Eur. Polym. J.* **2013**, *49* (2), 499–509 DOI: 10.1016/j.eurpolymj.2012.11.005.
- (7) Ni, T.; Nagesha, D. K.; Robles, J.; Materer, N. F.; Müssig, S.; Kotov, N. A. CdS nanoparticles modified to chalcogen sites: new supramolecular complexes, butterfly bridging, and related optical effects. *J. Am. Chem. Soc.* **2002**, *124* (15), 3980–3992.
- (8) Pérez-Juste, J.; Pastoriza-Santos, I.; Liz-Marzán, L. M.; Mulvaney, P. Gold nanorods: synthesis, characterization and applications. *Coord. Chem. Rev.* **2005**, *249* (17), 1870–1901.
- (9) Jung, J.; Kim, K. W.; Na, K.; Kaholek, M.; Zauscher, S.; Hyun, J. Fabrication of Micropatterned Gold Nanoparticle Arrays as a Template for Surface-Initiated Polymerization of Stimuli-Responsive Polymers. *Macromol. Rapid Commun.* **2006**, *27* (10), 776–780.
- (10) Latham, A. H.; Williams, M. E. Controlling transport and chemical functionality of magnetic nanoparticles. *Acc. Chem. Res.* **2008**, *41* (3), 411–420.

- (11) Rangappa, D.; Ohara, S.; Umetsu, M.; Naka, T.; Adschiri, T. Synthesis, characterization and organic modification of copper manganese oxide nanocrystals under supercritical water. *J. Supercrit. Fluids* **2008**, *44* (3), 441–445.
- (12) Kumfer, B. M.; Shinoda, K.; Jeyadevan, B.; Kennedy, I. M. Gas-phase flame synthesis and properties of magnetic iron oxide nanoparticles with reduced oxidation state. *J. Aerosol Sci.* **2010**, *41* (3), 257–265.
- (13) Yuan, J.; Schacher, F.; Drechsler, M.; Hanisch, A.; Lu, Y.; Ballauff, M.; Müller, A. H. Stimuli-responsive organosilica hybrid nanowires decorated with metal nanoparticles. *Chem. Mater.* **2010**, *22* (8), 2626–2634.
- (14) Wang, Y.; Su, D.; Ung, A.; Ahn, J.; Wang, G. Hollow CoFe₂O₄ nanospheres as a high capacity anode material for lithium ion batteries. *Nanotechnology* **2012**, *23* (5), 55402.
- (15) Hunt, S. T.; Nimmanwudipong, T.; Román-Leshkov, Y. Engineering Non-sintered, Metal-Terminated Tungsten Carbide Nanoparticles for Catalysis. *Angew. Chem. Int. Ed.* **2014**, *53* (20), 5131–5136.
- (16) Wu, L.; Cai, X.; Nelson, K.; Xing, W.; Xia, J.; Zhang, R.; Stacy, A. J.; Luderer, M.; Lanza, G. M.; Wang, L. V. A green synthesis of carbon nanoparticles from honey and their use in real-time photoacoustic imaging. *Nano Res.* **2013**, *6* (5), 312–325.
- (17) Johnson, N. Batch Scale-Up Synthesis Of Pvp Coated Iron Oxide Nanoparticles For Oil Remediation. **2016**.
- (18) Sakarya, K.; Akyol, Ç.; Demirel, B. The Effect of Short-Term Exposure of Engineered Nanoparticles on Methane Production During Mesophilic Anaerobic Digestion of Primary Sludge. *Water. Air. Soil Pollut.* **2015**, *226* (4), 1–9.
- (19) Kumar, C. S.; Mohammad, F. Magnetic nanomaterials for hyperthermia-based therapy and controlled drug delivery. *Adv. Drug Deliv. Rev.* **2011**, *63* (9), 789–808.
- (20) Mahmoudi, M.; Sant, S.; Wang, B.; Laurent, S.; Sen, T. Superparamagnetic iron oxide nanoparticles (SPIONs): development, surface modification and applications in chemotherapy. *Adv. Drug Deliv. Rev.* **2011**, *63* (1), 24–46.
- (21) Rahman, M. M.; Aisiri, A. M.; Jamal, A.; Faisal, M.; Khan, S. B. *Iron oxide nanoparticles*; INTECH Open Access Publisher, 2011.
- (22) Koneracka, M.; Kopčanský, P.; Timko, M.; Ramchand, C. N.; De Sequeira, A.; Trevan, M. Direct binding procedure of proteins and enzymes to fine magnetic particles. *J. Mol. Catal. B Enzym.* **2002**, *18* (1), 13–18.

- (23) Mehta, R. V.; Upadhyay, R. V.; Charles, S. W.; Ramchand, C. N. Direct binding of protein to magnetic particles. *Biotechnol. Tech.* **1997**, *11* (7), 493–496.
- (24) Koneracká, M.; Kopčanský, P.; Antalík, M.; Timko, M.; Ramchand, C. N.; Lobo, D.; Mehta, R. V.; Upadhyay, R. V. Immobilization of proteins and enzymes to fine magnetic particles. *J. Magn. Magn. Mater.* **1999**, *201* (1), 427–430.
- (25) Ditsch, A.; Laibinis, P. E.; Wang, D. I.; Hatton, T. A. Controlled clustering and enhanced stability of polymer-coated magnetic nanoparticles. *Langmuir* **2005**, *21* (13), 6006–6018.
- (26) Mout, R.; Moyano, D. F.; Rana, S.; Rotello, V. M. Surface functionalization of nanoparticles for nanomedicine. *Chem. Soc. Rev.* **2012**, *41* (7), 2539–2544.
- (27) Onaca, O.; Enea, R.; Hughes, D. W.; Meier, W. Stimuli-Responsive Polymersomes as Nanocarriers for Drug and Gene Delivery. *Macromol. Biosci.* **2009**, *9* (2), 129–139.
- (28) LoPresti, C.; Lomas, H.; Massignani, M.; Smart, T.; Battaglia, G. Polymersomes: nature inspired nanometer sized compartments. *J. Mater. Chem.* **2009**, *19* (22), 3576–3590.
- (29) Manivasagam, G.; Dhinasekaran, D.; Rajamanickam, A. Biomedical implants: Corrosion and its prevention-a review. *Recent Pat. Corros. Sci.* **2010**, *2* (1), 40–54.
- (30) Ansari, R.; Alikhani, A. H. Application of polyaniline/nylon composites coating for corrosion protection of steel. *J. Coat. Technol. Res.* **2009**, *6* (2), 221–227.
- (31) Hager, M. D.; Greil, P.; Leyens, C.; van der Zwaag, S.; Schubert, U. S. Self-Healing Materials. *Adv. Mater.* **2010**, *22* (47), 5424–5430.
- (32) White, S. R.; Sottos, N. R.; Geubelle, P. H.; Moore, J. S.; Kessler, M.; Sriram, S. R.; Brown, E. N.; Viswanathan, S. Autonomic healing of polymer composites. *Nature* **2001**, *409* (6822), 794–797.
- (33) Blaiszik, B. J.; Kramer, S. L. B.; Olugebefola, S. C.; Moore, J. S.; Sottos, N. R.; White, S. R. Self-healing polymers and composites. *Annu. Rev. Mater. Res.* **2010**, *40*, 179–211.
- (34) Kim, K. J.; Tadokoro, S. Electroactive polymers for robotic applications. *Artif. Muscles Sens. 291 P Springer Lond. U. K.* **2007**.
- (35) Shahinpoor, M.; Bar-Cohen, Y.; Simpson, J. O.; Smith, J. Ionic polymer-metal composites (IPMCs) as biomimetic sensors, actuators and artificial muscles-a review. *Smart Mater. Struct.* **1998**, *7* (6), R15.

- (36) López-Serrano, A.; Olivas, R. M.; Landaluze, J. S.; Cámara, C. Nanoparticles: a global vision. Characterization, separation, and quantification methods. Potential environmental and health impact. *Anal. Methods* **2014**, *6* (1), 38–56.
- (37) Klaine, S. J.; Koelmans, A. A.; Horne, N.; Carley, S.; Handy, R. D.; Kapustka, L.; Nowack, B.; von der Kammer, F. Paradigms to assess the environmental impact of manufactured nanomaterials. *Environ. Toxicol. Chem.* **2012**, *31* (1), 3–14.
- (38) Lee, S.; Choi, S.-S.; Li, S.; Eastman, J. A. Measuring thermal conductivity of fluids containing oxide nanoparticles. *J. Heat Transf.* **1999**, *121* (2), 280–289.
- (39) Rodríguez-Arco, L.; Gómez-Ramírez, A.; Durán, J. D.; López-López, M. T.; Vertecky, R.; Vassura, G. *New perspectives for magnetic fluid-based devices using novel ionic liquids as carriers*; INTECH Open Access Publisher, 2012.
- (40) Rosensweig, R. E. Ferrohydrodynamics Cambridge University Press, Cambridge, 1985. *Ferrofluids Magn. Control. Fluids Their Appl.* **1997**.
- (41) Neouze, M.-A.; Schubert, U. Surface modification and functionalization of metal and metal oxide nanoparticles by organic ligands. *Monatshefte Für Chem.-Chem. Mon.* **2008**, *139* (3), 183–195.
- (42) Ganguly, R.; Zellmer, B.; Puri, I. K. Field-induced self-assembled ferrofluid aggregation in pulsatile flow. *Phys. Fluids 1994-Present* **2005**, *17* (9), 97104.
- (43) Thompson, S. M.; Ma, H. B. Effect of localized heating on three-dimensional flat-plate oscillating heat pipe. *Adv. Mech. Eng.* **2010**, *2*, 465153.
- (44) Thompson, S. M.; Lu, H.; Ma, H. Thermal spreading with flat-plate oscillating heat pipes. *J. Thermophys. Heat Transf.* **2014**, *29* (2), 338–345.
- (45) Akachi, H. *Structure of a heat pipe*; Google Patents, 1990.
- (46) Ma, H. B.; Wilson, C.; Borgmeyer, B.; Park, K.; Yu, Q.; Choi, S. U. S.; Tirumala, M. Effect of nanofluid on the heat transport capability in an oscillating heat pipe. *Appl. Phys. Lett.* **2006**, *88* (14), 143116.
- (47) Thompson, S. M.; Aspin, Z. S.; Shamsaei, N.; Elwany, A.; Bian, L. Additive manufacturing of heat exchangers: A case study on a multi-layered Ti–6Al–4V oscillating heat pipe. *Addit. Manuf.* **2015**, *8*, 163–174.
- (48) Zhang, Y.; Faghri, A. Advances and unsolved issues in pulsating heat pipes. *Heat Transf. Eng.* **2008**, *29* (1), 20–44.
- (49) Xu, J. L.; Zhang, X. M. Start-up and steady thermal oscillation of a pulsating heat pipe. *Heat Mass Transf.* **2005**, *41* (8), 685–694.

- (50) Qu, W.; Ma, H. B. Theoretical analysis of startup of a pulsating heat pipe. *Int. J. Heat Mass Transf.* **2007**, *50* (11), 2309–2316.
- (51) Suzuki, O. Heat-transport Characteristics of a Bubble-driven Non-looped Heat-transport Device (Japanese). *Trans. Jpn. Soc. Mech. Eng. Part B* **2003**, *69* (678), 430–436 DOI: 10.1248/cpb.37.3229.
- (52) Fairley, J. D.; Thompson, S. M.; Anderson, D. Time Frequency Analysis of Flat-Plate Oscillating Heat Pipes. *Int. J. Therm. Sci.* **2015**, *91*, 113–124 DOI: 10.1016/j.ijthermalsci.2015.01.001.
- (53) Ma, H. B.; Borgmeyer, B.; Cheng, P.; Zhang, Y. Heat Transport Capability in an Oscillating Heat Pipe. *J. Heat Transf.* **2008**, *130* (August 2008), 1–7 DOI: 10.1115/1.2909081.
- (54) Shafii, M. B.; Faghri, A.; Zhang, Y. Thermal modeling of unlooped and looped pulsating heat pipes. *J. Heat Transf.* **2001**, *123* (6), 1159–1172.
- (55) Groll, M.; Khandekar, S. Pulsating heat pipes: a challenge and still unsolved problem in heat pipe science. *Arch. Thermodyn.* **2002**, *23* (4), 17–28.
- (56) de las Heras Alarcón, C.; Pennadam, S.; Alexander, C. Stimuli responsive polymers for biomedical applications. *Chem. Soc. Rev.* **2005**, *34* (3), 276–285.
- (57) Mendes, P. M. Stimuli-responsive surfaces for bio-applications. *Chem. Soc. Rev.* **2008**, *37* (11), 2512–2529.
- (58) Lee, H.; Pietrasik, J.; Sheiko, S. S.; Matyjaszewski, K. Stimuli-responsive molecular brushes. *Prog. Polym. Sci.* **2010**, *35* (1), 24–44.
- (59) Hirokawa, Y.; Tanaka, T. Volume phase transition in a nonionic gel. *J. Chem. Phys.* **1984**, *81* (12), 6379–6380.
- (60) Hirotsu, S.; Hirokawa, Y.; Tanaka, T. Volume-phase transitions of ionized N-isopropylacrylamide gels. *J. Chem. Phys.* **1987**, *87* (2), 1392–1395.
- (61) Ilavsky, M. Phase transition in swollen gels. 2. Effect of charge concentration on the collapse and mechanical behavior of polyacrylamide networks. *Macromolecules* **1982**, *15* (3), 782–788.
- (62) Stauffer, D.; Coniglio, A.; Adam, M. Gelation and critical phenomena. In *Polymer networks*; Springer, 1982; pp 103–158.
- (63) Jeong, B.; Gutowska, A. Lessons from nature: stimuli-responsive polymers and their biomedical applications. *Trends Biotechnol.* **2002**, *20* (7), 305–311.

- (64) Nath, N.; Chilkoti, A. Creating “smart” surfaces using stimuli responsive polymers. *Adv. Mater.* **2002**, *14* (17), 1243–1247.
- (65) Granville, A. M.; Boyes, S. G.; Akgun, B.; Foster, M. D.; Brittain, W. J. Synthesis and characterization of stimuli-responsive semifluorinated polymer brushes prepared by atom transfer radical polymerization. *Macromolecules* **2004**, *37* (8), 2790–2796.
- (66) Brittain, W. J.; Boyes, S. G.; Granville, A. M.; Baum, M.; Mirous, B. K.; Akgun, B.; Zhao, B.; Blickle, C.; Foster, M. D. Surface rearrangement of diblock copolymer brushes—stimuli responsive films. In *Surface-Initiated Polymerization II*; Springer, 2006; pp 125–147.
- (67) Motornov, M.; Sheparovych, R.; Tokarev, I.; Roiter, Y.; Minko, S. Nonwetable Thin Films from Hybrid Polymer Brushes Can Be Hydrophilic. *Langmuir* **2007**, *23* (1), 13–19 DOI: 10.1021/la061737q.
- (68) Chandrawati, R. Enzyme-responsive polymer hydrogels for therapeutic delivery. *Exp. Biol. Med.* **2016**, *241* (9), 972–979.
- (69) Xia, H.; Zhao, Y.; Tong, R. Ultrasound-Mediated Polymeric Micelle Drug Delivery. In *Therapeutic Ultrasound*; Springer, 2016; pp 365–384.
- (70) Zheng, P.; Cao, Y.; Lissel, F.; Linder, C.; You, X.-Z.; Bao, Z. A highly stretchable autonomous self-healing elastomer. **2016**.
- (71) Rao, Y.-L.; Chortos, A.; Pfattner, R.; Lissel, F.; Chiu, Y.-C.; Feig, V.; Xu, J.; Kurosawa, T.; Gu, X.; Wang, C. Stretchable Self-Healing Polymeric Dielectrics Cross-Linked Through Metal–Ligand Coordination. *J. Am. Chem. Soc.* **2016**, *138* (18), 6020–6027.
- (72) Heinzmann, C.; Weder, C.; de Espinosa, L. M. Supramolecular polymer adhesives: advanced materials inspired by nature. *Chem. Soc. Rev.* **2016**, *45* (2), 342–358.
- (73) Michal, B. T.; Spencer, E. J.; Rowan, S. J. Stimuli-Responsive Reversible Two-Level Adhesion from a Structurally Dynamic Shape-Memory Polymer. *ACS Appl. Mater. Interfaces* **2016**, *8* (17), 11041–11049.
- (74) Holtz, J. H.; Asher, S. A. Polymerized colloidal crystal hydrogel films as intelligent chemical sensing materials. *Nature* **1997**, *389* (6653), 829–832.
- (75) Abu-Lail, N. I.; Kaholek, M.; LaMattina, B.; Clark, R. L.; Zauscher, S. Micro-cantilevers with end-grafted stimulus-responsive polymer brushes for actuation and sensing. *Sens. Actuators B Chem.* **2006**, *114* (1), 371–378.

- (76) Lai, C.-Y.; Trewyn, B. G.; Jeftinija, D. M.; Jeftinija, K.; Xu, S.; Jeftinija, S.; Lin, V. S.-Y. A mesoporous silica nanosphere-based carrier system with chemically removable CdS nanoparticle caps for stimuli-responsive controlled release of neurotransmitters and drug molecules. *J. Am. Chem. Soc.* **2003**, *125* (15), 4451–4459.
- (77) Lynn, D. M.; Amiji, M. M.; Langer, R. pH-responsive polymer microspheres: Rapid release of encapsulated material within the range of intracellular pH. *Angew. Chem. Int. Ed.* **2001**, *40* (9), 1707–1710.
- (78) Mishra, B.; Patel, B. B.; Tiwari, S. Colloidal nanocarriers: a review on formulation technology, types and applications toward targeted drug delivery. *Nanomedicine Nanotechnol. Biol. Med.* **2010**, *6* (1), 9–24.
- (79) Meng, H.; Li, G. A review of stimuli-responsive shape memory polymer composites. *Polymer* **2013**, *54* (9), 2199–2221.
- (80) Hu, J.; Meng, H.; Li, G.; Ibekwe, S. I. A review of stimuli-responsive polymers for smart textile applications. *Smart Mater. Struct.* **2012**, *21* (5), 53001.
- (81) Cobo, I.; Li, M.; Sumerlin, B. S.; Perrier, S. Smart hybrid materials by conjugation of responsive polymers to biomacromolecules. *Nat. Mater.* **2015**, *14* (2), 143–159.
- (82) Fusco, S.; Borzacchiello, A.; Netti, P. A. Perspectives on: PEO-PPO-PEO triblock copolymers and their biomedical applications. *J. Bioact. Compat. Polym.* **2006**, *21* (2), 149–164.
- (83) Rummeli, M. H.; Borowiak-Palen, E.; Gemming, T.; Pichler, T.; Knupfer, M.; Kalbác, M.; Dunsch, L.; Jost, O.; Silva, S. R. P.; Pompe, W. Novel catalysts, room temperature, and the importance of oxygen for the synthesis of single-walled carbon nanotubes. *Nano Lett.* **2005**, *5* (7), 1209–1215.
- (84) Chen, S.; Li, Y.; Guo, C.; Wang, J.; Ma, J.; Liang, X.; Yang, L.-R.; Liu, H.-Z. Temperature-responsive magnetite/PEO-PPO-PEO block copolymer nanoparticles for controlled drug targeting delivery. *Langmuir* **2007**, *23* (25), 12669–12676.
- (85) Fleige, E.; Quadir, M. A.; Haag, R. Stimuli-responsive polymeric nanocarriers for the controlled transport of active compounds: concepts and applications. *Adv. Drug Deliv. Rev.* **2012**, *64* (9), 866–884.
- (86) Erk, K. A.; Henderson, K. J.; Shull, K. R. Strain stiffening in synthetic and biopolymer networks. *Biomacromolecules* **2010**, *11* (5), 1358–1363.
- (87) Zabet, M.; Mishra, S.; Kundu, S. Effect of graphene on the self-assembly and rheological behavior of a triblock copolymer gel. *RSC Adv.* **2015**, *5* (102), 83936–83944.

- (88) Hashemnejad, S. M.; Kundu, S. Strain stiffening and negative normal stress in alginate hydrogels. *J. Polym. Sci. Part B Polym. Phys.* **2016**.
- (89) Gupta, P.; Vermani, K.; Garg, S. Hydrogels: from controlled release to pH-responsive drug delivery. *Drug Discov. Today* **2002**, 7 (10), 569–579.
- (90) Jiang, H. Y.; Kelch, S.; Lendlein, A. Polymers move in response to light. *Adv. Mater.* **2006**, 18 (11), 1471–1475.
- (91) Chung, J. E.; Yokoyama, M.; Yamato, M.; Aoyagi, T.; Sakurai, Y.; Okano, T. Thermo-responsive drug delivery from polymeric micelles constructed using block copolymers of poly (N-isopropylacrylamide) and poly (butylmethacrylate). *J. Controlled Release* **1999**, 62 (1), 115–127.
- (92) Schmaljohann, D. Thermo-and pH-responsive polymers in drug delivery. *Adv. Drug Deliv. Rev.* **2006**, 58 (15), 1655–1670.
- (93) Chen, G.; Hoffman, A. S. Graft copolymers that exhibit temperature-induced phase transitions over a wide range of pH. *Nature* **1995**, 373 (6509), 49–52.
- (94) Servant, A.; Leon, V.; Jasim, D.; Methven, L.; Limousin, P.; Fernandez-Pacheco, E. V.; Prato, M.; Kostarelos, K. Graphene-Based Electroresponsive Scaffolds as Polymeric Implants for On-Demand Drug Delivery. *Adv. Healthc. Mater.* **2014**, 3 (8), 1334–1343.
- (95) James, H. P.; John, R.; Alex, A.; Anoop, K. R. Smart polymers for the controlled delivery of drugs—a concise overview. *Acta Pharm. Sin. B* **2014**, 4 (2), 120–127.
- (96) Shim, M. S.; Xia, Y. A Reactive Oxygen Species (ROS)-Responsive Polymer for Safe, Efficient, and Targeted Gene Delivery in Cancer Cells. *Angew. Chem. Int. Ed.* **2013**, 52 (27), 6926–6929.
- (97) Fleige, E.; Quadir, M. A.; Haag, R. Stimuli-responsive polymeric nanocarriers for the controlled transport of active compounds: concepts and applications. *Adv. Drug Deliv. Rev.* **2012**, 64 (9), 866–884.
- (98) Pankhurst, Q. A.; Connolly, J.; Jones, S. K.; Dobson, J. J. Applications of magnetic nanoparticles in biomedicine. *J. Phys. Appl. Phys.* **2003**, 36 (13), R167.
- (99) McCarthy, J. R.; Weissleder, R. Multifunctional magnetic nanoparticles for targeted imaging and therapy. *Adv. Drug Deliv. Rev.* **2008**, 60 (11), 1241–1251.
- (100) Namdeo, M.; Saxena, S.; Tankhiwale, R.; Bajpai, M.; Mohan, Y. M.; Bajpai, S. K. Magnetic nanoparticles for drug delivery applications. *J. Nanosci. Nanotechnol.* **2008**, 8 (7), 3247–3271.

- (101) Ayres, N.; Boyes, S. G.; Brittain, W. J. Stimuli-responsive polyelectrolyte polymer brushes prepared via atom-transfer radical polymerization. *Langmuir* **2007**, *23* (1), 182–189.
- (102) Motornov, M.; Sheparovych, R.; Lupitskyy, R.; MacWilliams, E.; Hoy, O.; Luzinov, I.; Minko, S. Stimuli-Responsive Colloidal Systems from Mixed Brush-Coated Nanoparticles. *Adv. Funct. Mater.* **2007**, *17* (14), 2307–2314.
- (103) Robinson, I.; Alexander, C.; Lu, L. T.; Tung, L. D.; Fernig, D. G.; Thanh, N. T. One-step synthesis of monodisperse water-soluble “dual-responsive” magnetic nanoparticles. *Chem. Commun.* **2007**, No. 44, 4602–4604.
- (104) Chuang, C.-Y.; Don, T.-M.; Chiu, W.-Y. Synthesis and properties of chitosan-based thermo-and pH-responsive nanoparticles and application in drug release. *J. Polym. Sci. Part Polym. Chem.* **2009**, *47* (11), 2798–2810.
- (105) Marutani, E.; Yamamoto, S.; Ninjbadgar, T.; Tsujii, Y.; Fukuda, T.; Takano, M. Surface-initiated atom transfer radical polymerization of methyl methacrylate on magnetite nanoparticles. *Polymer* **2004**, *45* (7), 2231–2235 DOI: 10.1016/j.polymer.2004.02.005.
- (106) Rutnakornpituk, M.; Puangsin, N.; Theamdee, P.; Rutnakornpituk, B.; Wichai, U. Poly(acrylic acid)-grafted magnetic nanoparticle for conjugation with folic acid. *Polymer* **2011**, *52* (4), 987–995 DOI: 10.1016/j.polymer.2010.12.059.
- (107) Kang SM; Choi IS; Lee KB; Kim YS. Bioconjugation of Poly(poly(ethylene glycol) methacrylate)-Coated Iron Oxide Magnetic Nanoparticles for Magnetic Capture of Target Proteins. *Macromol. Res.* **2009**, *17* (4), 259–264.
- (108) García, I.; Tercjak, A.; Zafeiropoulos, N. E.; Stamm, M.; Mondragon, I. Self-Assembling Nanomaterials using Magnetic Nanoparticles Modified with Polystyrene Brushes. *Macromol. Rapid Commun.* **2007**, *28* (24), 2361–2365 DOI: 10.1002/marc.200700392.
- (109) Shim, M. S.; Kwon, Y. J. Stimuli-responsive polymers and nanomaterials for gene delivery and imaging applications. *Stimuli-Responsive Drug Deliv. Syst.* **2012**, *64* (11), 1046–1059 DOI: 10.1016/j.addr.2012.01.018.
- (110) da Rocha, S. R.; Johnston, K. P.; Rossky, P. J. Surfactant-modified CO₂-water interface: A molecular view. *J. Phys. Chem. B* **2002**, *106* (51), 13250–13261.
- (111) Sun, J.-T.; Hong, C.-Y.; Pan, C.-Y. Surface modification of carbon nanotubes with dendrimers or hyperbranched polymers. *Polym. Chem.* **2011**, *2* (5), 998–1007.
- (112) Zhang, H.-S.; Komvopoulos, K. Surface modification of magnetic recording media by filtered cathodic vacuum arc. *J. Appl. Phys.* **2009**, *106* (9), 93504.

- (113) Han, T.-H.; Kwon, S.-J.; Seo, H.-K.; Lee, T.-W. Controlled surface oxidation of multi-layered graphene anode to increase hole injection efficiency in organic electronic devices. *2D Mater.* **2016**, 3 (1), 14003.
- (114) Teichmann, J.; Nitschke, M.; Pette, D.; Valtink, M.; Gramm, S.; Härtel, F. V.; Noll, T.; Funk, R. H.; Engelmann, K.; Werner, C. Thermo-responsive cell culture carriers based on poly (vinyl methyl ether)—the effect of biomolecular ligands to balance cell adhesion and stimulated detachment. *Sci. Technol. Adv. Mater.* **2016**.
- (115) Potts, J. R.; Roy, S.; Johnson, M. H.; Sadana, A. K. *METHODS OF FORMING STRUCTURES FOR DOWNHOLE APPLICATIONS, AND RELATED DOWNHOLE STRUCTURES AND ASSEMBLIES*; US Patent 20,160,101,600, 2016.
- (116) Edmondson, S.; Huck, W. T. Controlled growth and subsequent chemical modification of poly (glycidyl methacrylate) brushes on silicon wafers. *J. Mater. Chem.* **2004**, 14 (4), 730–734.
- (117) Patten, T. E.; Matyjaszewski, K. Atom transfer radical polymerization and the synthesis of polymeric materials. *Adv. Mater.* **1998**, 10 (12), 901–915.
- (118) Pintauer, T.; Matyjaszewski, K. Atom transfer radical addition and polymerization reactions catalyzed by ppm amounts of copper complexes. *Chem. Soc. Rev.* **2008**, 37 (6), 1087–1097.
- (119) Huang, W.; Kim, J.-B.; Bruening, M. L.; Baker, G. L. Functionalization of surfaces by water-accelerated atom-transfer radical polymerization of hydroxyethyl methacrylate and subsequent derivatization. *Macromolecules* **2002**, 35 (4), 1175–1179.
- (120) Husseman, M.; Malmström, E. E.; McNamara, M.; Mate, M.; Mecerreyes, D.; Benoit, D. G.; Hedrick, J. L.; Mansky, P.; Huang, E.; Russell, T. P. Controlled synthesis of polymer brushes by “living” free radical polymerization techniques. *Macromolecules* **1999**, 32 (5), 1424–1431.
- (121) Mornet, S.; Vasseur, S.; Grasset, F.; Duguet, E. Magnetic nanoparticle design for medical diagnosis and therapy. *J Mater Chem* **2004**, 14 (14), 2161–2175 DOI: 10.1039/B402025A.
- (122) Berry, C. C.; Curtis, A. S. G. Functionalisation of magnetic nanoparticles for applications in biomedicine. *J. Phys. Appl. Phys.* **2003**, 36 (13), R198.
- (123) Shinkai, M. Functional magnetic particles for medical application. *J. Biosci. Bioeng.* **2002**, 94 (6), 606–613.

- (124) Suda, M.; Nakagawa, M.; Iyoda, T.; Einaga, Y. Reversible photoswitching of ferromagnetic FePt nanoparticles at room temperature. *J. Am. Chem. Soc.* **2007**, *129* (17), 5538–5543 DOI: 10.1021/ja0682374.
- (125) Rosensweig, R. E. *Ferrohydrodynamics*; Courier Corporation, 2013.
- (126) Raj, K.; Moskowitz, R. Commercial applications of ferrofluids. *J. Magn. Magn. Mater.* **1990**, *85* (1–3), 233–245.
- (127) Raj, K.; Moskowitz, R. A review of damping applications of ferrofluids. *Magn. IEEE Trans. On* **1980**, *16* (2), 358–363.
- (128) Bailey, R. L. Lesser known applications of ferrofluids. *J. Magn. Magn. Mater.* **1983**, *39* (1–2), 178–182.
- (129) Rosensweig, R. E. Fluid dynamics and science of magnetic liquids. *Adv. Electron. Electron Phys.* **1979**, *48*, 103–199.
- (130) Rosensweig, R. E. Magnetic fluids. *Sci. Am.* **1982**, *247* (4), 136–145.
- (131) Odenbach, S. Ferrofluids—magnetically controlled suspensions. *Colloids Surf. Physicochem. Eng. Asp.* **2003**, *217* (1), 171–178.
- (132) Fertman, V. E. *Magnetic fluids guidebook: properties and applications*; Hemisphere Publishing Corporation, 1990.
- (133) Baruwati, B.; Nadagouda, M. N.; Varma, R. S. Bulk Synthesis of Monodisperse Ferrite Nanoparticles at Water–Organic Interfaces under Conventional and Microwave Hydrothermal Treatment and Their Surface Functionalization. *J. Phys. Chem. C* **2008**, *112* (47), 18399–18404 DOI: 10.1021/jp807245g.
- (134) Synthesis of Magnetic Nanoparticles of Fe₃O₄ and CoFe₂O₄ and Their Surface Modification by Surfactant Adsorption. *Bull. Korean Chem. Soc.* **2006**, *27* (2), 237–242 DOI: 10.5012/bkcs.2006.27.2.237.
- (135) Thapa, D.; Kulkarni, N.; Mishra, S. N.; Paulose, P. L.; Ayyub, P. Enhanced magnetization in cubic ferrimagnetic CuFe₂O₄ nanoparticles synthesized from a citrate precursor: the role of Fe²⁺. *J. Phys. Appl. Phys.* **2010**, *43* (19), 195004.
- (136) Bhattacharyya, S.; Salvétat, J.-P.; Fleurier, R.; Husmann, A.; Cacciaguerra, T.; Saboungi, M.-L. One step synthesis of highly crystalline and high coercive cobalt-ferrite nanocrystals. *Chem Commun* **2005**, No. 38, 4818–4820 DOI: 10.1039/B509026A.
- (137) Sun, S.; Zeng, H.; Robinson, D. B.; Raoux, S.; Rice, P. M.; Wang, S. X.; Li, G. Monodisperse MFe₂O₄ (M = Fe, Co, Mn) Nanoparticles. *J. Am. Chem. Soc.* **2004**, *126* (1), 273–279 DOI: 10.1021/ja0380852.

- (138) Song, Q.; Zhang, Z. J. Shape Control and Associated Magnetic Properties of Spinel Cobalt Ferrite Nanocrystals. *J. Am. Chem. Soc.* **2004**, *126* (19), 6164–6168 DOI: 10.1021/ja049931r.
- (139) Bao, N.; Shen, L.; An, W.; Padhan, P.; Heath Turner, C.; Gupta, A. Formation Mechanism and Shape Control of Monodisperse Magnetic CoFe₂O₄ Nanocrystals. *Chem. Mater.* **2009**, *21* (14), 3458–3468 DOI: 10.1021/cm901033m.
- (140) Cullity, B. D.; Graham, C. D. *Introduction to magnetic materials*; John Wiley & Sons, 2011.
- (141) Morais, P. C.; Garg, V. K.; Oliveira, A. C.; Silva, L. P.; Azevedo, R. B.; Silva, A. M. L.; Lima, E. C. D. Synthesis and characterization of size-controlled cobalt-ferrite-based ionic ferrofluids. *J. Magn. Magn. Mater.* **2001**, *225* (1), 37–40.
- (142) Baldi, G.; Bonacchi, D.; Innocenti, C.; Lorenzi, G.; Sangregorio, C. Cobalt ferrite nanoparticles: The control of the particle size and surface state and their effects on magnetic properties. *J. Magn. Magn. Mater.* **2007**, *311* (1), 10–16.
- (143) Liu, C.; Zou, B.; Rondinone, A. J.; Zhang, Z. J. Chemical control of superparamagnetic properties of magnesium and cobalt spinel ferrite nanoparticles through atomic level magnetic couplings. *J. Am. Chem. Soc.* **2000**, *122* (26), 6263–6267.
- (144) Maaz, K.; Mumtaz, A.; Hasanain, S. K.; Ceylan, A. Synthesis and magnetic properties of cobalt ferrite (CoFe₂O₄) nanoparticles prepared by wet chemical route. *J. Magn. Magn. Mater.* **2007**, *308* (2), 289–295.
- (145) Sharifi, I.; Shokrollahi, H.; Amiri, S. Ferrite-based magnetic nanofluids used in hyperthermia applications. *J. Magn. Magn. Mater.* **2012**, *324* (6), 903–915.
- (146) Caltun, O.; Dumitru, I.; Feder, M.; Lupu, N.; Chiriac, H. Substituted cobalt ferrites for sensors applications. *J. Magn. Magn. Mater.* **2008**, *320* (20), e869–e873.
- (147) Ayyappan, S.; Philip, J.; Raj, B. A facile method to control the size and magnetic properties of CoFe₂O₄ nanoparticles. *Mater. Chem. Phys.* **2009**, *115* (2), 712–717.
- (148) Mamniashvili, G. I.; Mikeladze, S. V.; Gegechkori, T. O.; Surguladze, B. V.; Pichkhaia, G. N.; Akhalkatsi, A. M.; Daraselia, D. M.; Japaridze, D. L. Magnetometry and Hyperthermia Study of Magnetic Fluid Preparation UNIMAG. *World J. Condens. Matter Phys.* **2014**, *2014*.
- (149) Amiri, S.; Shokrollahi, H. The role of cobalt ferrite magnetic nanoparticles in medical science. *Mater. Sci. Eng. C* **2013**, *33* (1), 1–8.

- (150) Mohamed, R. M.; Rashad, M. M.; Haraz, F. A.; Sigmund, W. Structure and magnetic properties of nanocrystalline cobalt ferrite powders synthesized using organic acid precursor method. *J. Magn. Magn. Mater.* **2010**, *322* (14), 2058–2064.
- (151) Amiri, S.; Shokrollahi, H. The role of cobalt ferrite magnetic nanoparticles in medical science. *Mater. Sci. Eng. C* **2013**, *33* (1), 1–8.
- (152) Wu, H.; Liu, G.; Wang, X.; Zhang, J.; Chen, Y.; Shi, J.; Yang, H.; Hu, H.; Yang, S. Solvothermal synthesis of cobalt ferrite nanoparticles loaded on multiwalled carbon nanotubes for magnetic resonance imaging and drug delivery. *Acta Biomater.* **2011**, *7* (9), 3496–3504.
- (153) Joshi, H. M.; Lin, Y. P.; Aslam, M.; Prasad, P. V.; Schultz-Sikma, E. A.; Edelman, R.; Meade, T.; Dravid, V. P. Effects of shape and size of cobalt ferrite nanostructures on their MRI contrast and thermal activation. *J. Phys. Chem. C* **2009**, *113* (41), 17761–17767.
- (154) Ma, H. B.; Wilson, C.; Borgmeyer, B.; Park, K.; Yu, Q.; Choi, S. U. S.; Tirumala, M. Effect of nanofluid on the heat transport capability in an oscillating heat pipe. *Appl. Phys. Lett.* **2006**, *88* (14), 143116.
- (155) Ji, Y.; Ma, H.; Su, F.; Wang, G. Particle size effect on heat transfer performance in an oscillating heat pipe. *Exp. Therm. Fluid Sci.* **2011**, *35* (4), 724–727.
- (156) Sakulchangsattajai, P.; Terdtoon, P.; Wongratanaphisan, T.; Kamonpet, P.; Murakami, M. Operation modeling of closed-end and closed-loop oscillating heat pipes at normal operating condition. *Appl. Therm. Eng.* **2004**, *24* (7), 995–1008.
- (157) Lin, L.; Ponnappan, R.; Leland, J. Experimental investigation of oscillating heat pipes. *J. Thermophys. Heat Transf.* **2001**, *15* (4), 395–400.
- (158) Godson, L.; Raja, B.; Lal, D. M.; Wongwises, S. Enhancement of heat transfer using nanofluids—an overview. *Renew. Sustain. Energy Rev.* **2010**, *14* (2), 629–641.
- (159) Ma, H. B.; Borgmeyer, B.; Cheng, P.; Zhang, Y. Heat transport capability in an oscillating heat pipe. *J. Heat Transf.* **2008**, *130* (8), 81501.
- (160) Sureshkumar, R.; Mohideen, S. T.; Nethaji, N. Heat transfer characteristics of nanofluids in heat pipes: a review. *Renew. Sustain. Energy Rev.* **2013**, *20*, 397–410.
- (161) Qu, J.; Wu, H.; Cheng, P. Thermal performance of an oscillating heat pipe with Al₂O₃–water nanofluids. *Int. Commun. Heat Mass Transf.* **2010**, *37* (2), 111–115
DOI: 10.1016/j.icheatmasstransfer.2009.10.001.

- (162) Cheung, J. T.; Xin, H. *Magnetic transducer with ferrofluid end bearings*; Google Patents, 2007.
- (163) Guerrero, J. C.; Pabon, J. A.; Auzeais, F. M.; Chen, K. C.; Forbes, K. J. *Harvesting energy in remote locations*; Google Patents, 2011.
- (164) Wang, Y.; Zhang, Q.; Zhao, L.; Kim, E. S. Ferrofluid liquid spring for vibration energy harvesting. In *Micro Electro Mechanical Systems (MEMS), 2015 28th IEEE International Conference on*; IEEE, 2015; pp 122–125.
- (165) Breed, D. *Energy Harvesting Systems and Methods for Vehicles*; Google Patents, 2006.
- (166) Lee, D. Energy harvesting chip and the chip based power supply development for a wireless sensor network. *Sensors* **2008**, 8 (12), 7690–7714.
- (167) Brown, S. B.; Hendrickson, B. S. *Method and apparatus for energy harvesting using energy storage and release*; Google Patents, 2009.
- (168) Bibo, A.; Masana, R.; King, A.; Li, G.; Daqaq, M. F. Electromagnetic ferrofluid-based energy harvester. *Phys. Lett. A* **2012**, 376 (32), 2163–2166.
- (169) Ching-Yao Chen; Sheng-Yan Wang; Chi-Ming Wu; Chung-Hao Lin; Kuo-An Huang. CHARACTERISTICS OF ELECTROMAGNETIC INDUCTION BY MOVING FERROFLUIDS. *Magneto hydrodyn. 0024-998X* **2012**, 48 (3), 567–580.
- (170) Bibo, A.; Masana, R.; King, A.; Li, G.; Daqaq, M. F. Electromagnetic ferrofluid-based energy harvester. *Phys. Lett. A* **2012**, 376 (32), 2163–2166 DOI: 10.1016/j.physleta.2012.05.033.
- (171) Jagminas, A.; Kurtinaitienė, M.; Mažeika, K. Synthesis of cobalt ferrite nanoparticles by co-precipitation at ambient and hydrothermal conditions. *chemija* **2013**, 24 (2), 103–110.
- (172) Shao, H.; Dai, H.; Huang, J.; Huang, F.; Li, S. Synthesis of CoFe₂O₄ Nanoparticles by Coprecipitation Method and Its Magnetic Properties. *J.-Chin. Ceram. Soc.* **2005**, 33 (8), 959.
- (173) Zi, Z.; Sun, Y.; Zhu, X.; Yang, Z.; Dai, J.; Song, W. Synthesis and magnetic properties of CoFe₂O₄ ferrite nanoparticles. *J. Magn. Mater.* **2009**, 321 (9), 1251–1255 DOI: 10.1016/j.jmmm.2008.11.004.
- (174) Zhao, S. Y.; Lee, D.-G.; Kim, C.-W.; Cha, H.-G.; Kim, Y.-H.; Kang, Y.-S. Synthesis of magnetic nanoparticles of Fe₃O₄ and CoFe₂O₄ and their surface modification by surfactant adsorption. *Bull. Korean Chem. Soc.* **2006**, 27 (2), 237–242.

- (175) Adamson, A. W.; Gast, A. P. Physical chemistry of surfaces. **1967**.
- (176) Halsey, G. Physical adsorption on non-uniform surfaces. *J. Chem. Phys.* **1948**, *16* (10), 931–937.
- (177) Sahoo, S. K.; Panyam, J.; Prabha, S.; Labhasetwar, V. Residual polyvinyl alcohol associated with poly (D, L-lactide-co-glycolide) nanoparticles affects their physical properties and cellular uptake. *J. Controlled Release* **2002**, *82* (1), 105–114.
- (178) Ow, H.; Larson, D. R.; Srivastava, M.; Baird, B. A.; Webb, W. W.; Wiesner, U. Bright and stable core-shell fluorescent silica nanoparticles. *Nano Lett.* **2005**, *5* (1), 113–117.
- (179) Shenoy, D. B.; Amiji, M. M. Poly (ethylene oxide)-modified poly (ϵ -caprolactone) nanoparticles for targeted delivery of tamoxifen in breast cancer. *Int. J. Pharm.* **2005**, *293* (1), 261–270.
- (180) Monroe, J. G.; Vasquez, E. S.; Aspin, Z. S.; Fairley, J. D.; Walters, K. B.; Berg, M. J.; Thompson, S. M. Energy harvesting via ferrofluidic induction. In *SPIE Sensing Technology+ Applications*; International Society for Optics and Photonics, 2015; p 94930G–94930G–7.
- (181) Ai, L.; Huang, H.; Chen, Z.; Wei, X.; Jiang, J. Activated carbon/CoFe₂O₄ composites: Facile synthesis, magnetic performance and their potential application for the removal of malachite green from water. *Chem. Eng. J.* **2010**, *156* (2), 243–249 DOI: 10.1016/j.cej.2009.08.028.
- (182) Goh, S. C.; Chia, C. H.; Zakaria, S.; Yusoff, M.; Haw, C. Y.; Ahmadi, S.; Huang, N. M.; Lim, H. N. Hydrothermal preparation of high saturation magnetization and coercivity cobalt ferrite nanocrystals without subsequent calcination. *Mater. Chem. Phys.* **2010**, *120* (1), 31–35 DOI: 10.1016/j.matchemphys.2009.10.016.
- (183) Cheraghipour, E.; Javadpour, S.; Mehdizadeh, A. R. Citrate capped superparamagnetic iron oxide nanoparticles used for hyperthermia therapy. **2012**.
- (184) Indran, V. P.; Zuhaimi, N. A. S.; Deraman, M. A.; Maniam, G. P.; Yusoff, M. M.; Hin, T.-Y. Y.; Rahim, M. H. A. An accelerated route of glycerol carbonate formation from glycerol using waste boiler ash as catalyst. *RSC Adv.* **2014**, *4* (48), 25257–25267.
- (185) Yu, J.; Yang, J.; Liu, B.; Ma, X. Preparation and characterization of glycerol plasticized-pea starch/ZnO–carboxymethylcellulose sodium nanocomposites. *Bioresour. Technol.* **2009**, *100* (11), 2832–2841 DOI: <http://dx.doi.org/10.1016/j.biortech.2008.12.045>.

- (186) Zhang, L.; He, R.; Gu, H.-C. Oleic acid coating on the monodisperse magnetite nanoparticles. *Appl. Surf. Sci.* **2006**, *253* (5), 2611–2617 DOI: <http://dx.doi.org/10.1016/j.apsusc.2006.05.023>.
- (187) Marinca, T. F.; Chicinaş, H. F.; Neamţu, B. V.; Isnard, O.; Pascuta, P.; Lupu, N.; Stoian, G.; Chicinaş, I. Mechano-synthesis, structural, thermal and magnetic characteristics of oleic acid coated Fe₃O₄ nanoparticles. *Mater. Chem. Phys.* **2016**, *171*, 336–345 DOI: <http://dx.doi.org/10.1016/j.matchemphys.2016.01.025>.
- (188) Citric Acid—A Dispersant for Aqueous Alumina Suspensions. *J. Am. Ceram. Soc.* **1996**, *79* (7), 1857–1867 DOI: [10.1111/j.1151-2916.1996.tb08006.x](https://doi.org/10.1111/j.1151-2916.1996.tb08006.x).
- (189) Deygen, I. M.; Kudryashova, capital I. New versatile approach for analysis of PEG content in conjugates and complexes with biomacromolecules based on FTIR spectroscopy. *Colloids Surf. B Biointerfaces* **2016**, *141*, 36–43 DOI: [10.1016/j.colsurfb.2016.01.030](https://doi.org/10.1016/j.colsurfb.2016.01.030).
- (190) Wu, L.; Yin, X.; Guo, Z.; Tong, Y.; Feng, J.; York, P.; Xiao, T.; Chen, M.; Gu, J.; Zhang, J. Hydration induced material transfer in membranes of osmotic pump tablets measured by synchrotron radiation based {FTIR}. *Eur. J. Pharm. Sci.* **2016**, *84*, 132–138 DOI: <http://dx.doi.org/10.1016/j.ejps.2016.01.020>.
- (191) Vadivel, M.; Babu, R. R.; Arivanandhan, M.; Ramamurthi, K.; Hayakawa, Y. Role of SDS surfactant concentrations on the structural, morphological, dielectric and magnetic properties of CoFe₂O₄ nanoparticles. *RSC Adv* **2015**, *5* (34), 27060–27068 DOI: [10.1039/C5RA01162K](https://doi.org/10.1039/C5RA01162K).
- (192) Hussein, M. Z. B.; Zainal, Z.; Ming, C. Y. Microwave-assisted synthesis of Zn-Al-layered double hydroxide-sodium dodecyl sulfate nanocomposite. *J. Mater. Sci. Lett.* **19** (10), 879–883 DOI: [10.1023/A:1006745716997](https://doi.org/10.1023/A:1006745716997).
- (193) Ramaswamy, S.; Rajaram, R. K.; Ramakrishnan, V. Raman and IR spectral studies of D-phenylglycinium perchlorate. *J. Raman Spectrosc.* **2002**, *33* (9), 689–698 DOI: [10.1002/jrs.898](https://doi.org/10.1002/jrs.898).
- (194) Khan, T.; Siddiqui, Z. N. Perchloric acid modified-cellulose: a versatile, novel and biodegradable heterogeneous solid acid catalyst for single-pot synthesis of novel bis-pyran annulated heterocyclic scaffolds under solvent-free conditions. *New J. Chem.* **2014**, *38* (10), 4847–4858.
- (195) Sun, C.; Lee, J. S.; Zhang, M. Magnetic nanoparticles in MR imaging and drug delivery. *Adv. Drug Deliv. Rev.* **2008**, *60* (11), 1252–1265.
- (196) Mornet, S.; Vasseur, S.; Grasset, F.; Duguet, E. Magnetic nanoparticle design for medical diagnosis and therapy. *J. Mater. Chem.* **2004**, *14* (14), 2161–2175.

- (197) Na, H. B.; Song, I. C.; Hyeon, T. Inorganic nanoparticles for MRI contrast agents. *Adv. Mater.* **2009**, *21* (21), 2133–2148.
- (198) Dobson, J. Magnetic nanoparticles for drug delivery. *Drug Dev. Res.* **2006**, *67* (1), 55–60.
- (199) Arruebo, M.; Fernández-Pacheco, R.; Ibarra, M. R.; Santamaría, J. Magnetic nanoparticles for drug delivery. *Nano Today* **2007**, *2* (3), 22–32.
- (200) Hola, K.; Markova, Z.; Zoppellaro, G.; Tucek, J.; Zboril, R. Tailored functionalization of iron oxide nanoparticles for MRI, drug delivery, magnetic separation and immobilization of biosubstances. *Biotechnol. Adv.* **2015**, *33* (6), 1162–1176.
- (201) Sheng-Nan, S.; Chao, W.; Zan-Zan, Z.; Yang-Long, H.; Venkatraman, S. S.; Zhi-Chuan, X. Magnetic iron oxide nanoparticles: Synthesis and surface coating techniques for biomedical applications. *Chin. Phys. B* **2014**, *23* (3), 37503.
- (202) Johannsen, M.; Jordan, A.; Scholz, R.; Koch, M.; Lein, M.; Deger, S.; Roigas, J.; Jung, K.; Loening, S. Evaluation of magnetic fluid hyperthermia in a standard rat model of prostate cancer. *J. Endourol.* **2004**, *18* (5), 495–500.
- (203) Johannsen, M.; Thiesen, B.; Jordan, A.; Taymoorian, K.; Gneveckow, U.; Waldöfner, N.; Scholz, R.; Koch, M.; Lein, M.; Jung, K. Magnetic fluid hyperthermia (MFH) reduces prostate cancer growth in the orthotopic Dunning R3327 rat model. *The prostate* **2005**, *64* (3), 283–292.
- (204) Jordan, A.; Scholz, R.; Wust, P.; Fähling, H.; Felix, R. Magnetic fluid hyperthermia (MFH): Cancer treatment with AC magnetic field induced excitation of biocompatible superparamagnetic nanoparticles. *J. Magn. Magn. Mater.* **1999**, *201* (1), 413–419.
- (205) Minelli, C.; Lowe, S. B.; Stevens, M. M. Engineering nanocomposite materials for cancer therapy. *Small* **2010**, *6* (21), 2336–2357.
- (206) Fortin, J.-P.; Gazeau, F.; Wilhelm, C. Intracellular heating of living cells through Néel relaxation of magnetic nanoparticles. *Eur. Biophys. J.* **2008**, *37* (2), 223–228.
- (207) Fortin, J.-P.; Gazeau, F.; Wilhelm, C. Internal heating of living cells with magnetic nanomediators. *Eur. Biophys. J.* **2008**, *37*, 223–228.
- (208) Hergt, R.; Andra, W.; d'Ambly, C. G.; Hilger, I.; Kaiser, W. A.; Richter, U.; Schmidt, H.-G. Physical limits of hyperthermia using magnetite fine particles. *Magn. IEEE Trans. On* **1998**, *34* (5), 3745–3754.
- (209) Brannon-Peppas, L.; Blanchette, J. O. Nanoparticle and targeted systems for cancer therapy. *Adv. Drug Deliv. Rev.* **2004**, *56* (11), 1649–1659.

- (210) Qian, X.; Peng, X.-H.; Ansari, D. O.; Yin-Goen, Q.; Chen, G. Z.; Shin, D. M.; Yang, L.; Young, A. N.; Wang, M. D.; Nie, S. In vivo tumor targeting and spectroscopic detection with surface-enhanced Raman nanoparticle tags. *Nat. Biotechnol.* **2008**, *26* (1), 83–90.
- (211) Bohara, R. A.; Thorat, N. D.; Chaurasia, A. K.; Pawar, S. H. Cancer cell extinction through a magnetic fluid hyperthermia treatment produced by superparamagnetic Co–Zn ferrite nanoparticles. *RSC Adv* **2015**, *5* (58), 47225–47234.
- (212) Jayakumar, R.; Chennazhi, K. P.; Muzzarelli, R. A. A.; Tamura, H.; Nair, S. V.; Selvamurugan, N. Chitosan conjugated DNA nanoparticles in gene therapy. *Carbohydr. Polym.* **2010**, *79* (1), 1–8.
- (213) Mansouri, S.; Cuie, Y.; Winnik, F.; Shi, Q.; Lavigne, P.; Benderdour, M.; Beaumont, E.; Fernandes, J. C. Characterization of folate-chitosan-DNA nanoparticles for gene therapy. *Biomaterials* **2006**, *27* (9), 2060–2065.
- (214) Bohara, R. A.; Yadav, H. M.; Thorat, N. D.; Mali, S. S.; Hong, C. K.; Nanaware, S. G.; Pawar, S. H. Synthesis of functionalized Co_{0.5}Zn_{0.5}Fe₂O₄ nanoparticles for biomedical applications. *J. Magn. Magn. Mater.* **2015**, *378*, 397–401.
- (215) Amiri, S.; Shokrollahi, H. The role of cobalt ferrite magnetic nanoparticles in medical science. *Mater. Sci. Eng. C* **2013**, *33* (1), 1–8.
- (216) Ayyappan, S.; Philip, J.; Raj, B. A facile method to control the size and magnetic properties of CoFe₂O₄ nanoparticles. *Mater. Chem. Phys.* **2009**, *115* (2), 712–717.
- (217) Caltun, O.; Dumitru, I.; Feder, M.; Lupu, N.; Chiriac, H. Substituted cobalt ferrites for sensors applications. *J. Magn. Magn. Mater.* **2008**, *320* (20), e869–e873.
- (218) Smit, J. *Magnetic properties of materials*; McGraw-Hill, 1971; Vol. 13.
- (219) Abbas, Y. M.; Mansour, S. A.; Ibrahim, M. H.; Ali, S. E. Microstructure characterization and cation distribution of nanocrystalline cobalt ferrite. *J. Magn. Magn. Mater.* **2011**, *323* (22), 2748–2756.
- (220) Song, Q.; Zhang, Z. J. Correlation between spin-orbital coupling and the superparamagnetic properties in magnetite and cobalt ferrite spinel nanocrystals. *J. Phys. Chem. B* **2006**, *110* (23), 11205–11209.
- (221) Song, Q.; Ding, Y.; Wang, Z. L.; Zhang, Z. J. Formation of orientation-ordered superlattices of magnetite magnetic nanocrystals from shape-segregated self-assemblies. *J. Phys. Chem. B* **2006**, *110* (50), 25547–25550.

- (222) Coey, J. M. *Magnetism and magnetic materials*; Cambridge University Press, 2010.
- (223) Zhou, J.; Shi, Z.; He, H.; Nan, C.-W. Magnetic properties of ZnO-doped cobalt ferrite. *J. Electroceramics* **2008**, *21* (1–4), 681–685.
- (224) Chiu, W. S.; Radiman, S.; Abd-Shukur, R.; Abdullah, M. H.; Khiew, P. S. Tunable coercivity of CoFe₂O₄ nanoparticles via thermal annealing treatment. *J. Alloys Compd.* **2008**, *459* (1–2), 291–297 DOI: 10.1016/j.jallcom.2007.04.215.
- (225) Gul, I. H.; Maqsood, A. Structural, magnetic and electrical properties of cobalt ferrites prepared by the sol–gel route. *J. Alloys Compd.* **2008**, *465* (1–2), 227–231 DOI: 10.1016/j.jallcom.2007.11.006.
- (226) Iqbal, M. J.; Siddiquah, M. R. Electrical and magnetic properties of chromium-substituted cobalt ferrite nanomaterials. *J. Alloys Compd.* **2008**, *453* (1–2), 513–518 DOI: 10.1016/j.jallcom.2007.06.105.
- (227) Kim, J.-S.; Vaughey, J. T.; Johnson, C. S.; Thackeray, M. M. Significance of the Tetrahedral A Site on the Electrochemical Performance of Substituted Li_{1.05}Mn_{0.95}O₄ Spinel Electrodes (M= Li, Mg, Zn, Al) in Lithium Cells. *J. Electrochem. Soc.* **2003**, *150* (11), A1498–A1502.
- (228) Chapter 2 : Description of Magnetite Structure
<http://www.cmp.liv.ac.uk/shrike/mphys/chap2.html> (accessed Jun 19, 2016).
- (229) Kim, D.-H.; Nikles, D. E.; Johnson, D. T.; Brazel, C. S. Heat generation of aqueously dispersed CoFe₂O₄ nanoparticles as heating agents for magnetically activated drug delivery and hyperthermia. *J. Magn. Magn. Mater.* **2008**, *320* (19), 2390–2396.
- (230) Sharifi, I.; Shokrollahi, H.; Doroodmand, M. M.; Safi, R. Magnetic and structural studies on CoFe₂O₄ nanoparticles synthesized by co-precipitation, normal micelles and reverse micelles methods. *J. Magn. Magn. Mater.* **2012**, *324* (10), 1854–1861.
- (231) Rosensweig, R. E. Heating magnetic fluid with alternating magnetic field. *J. Magn. Magn. Mater.* **2002**, *252*, 370–374.
- (232) Sharifi, I.; Shokrollahi, H.; Amiri, S. Ferrite-based magnetic nanofluids used in hyperthermia applications. *J. Magn. Magn. Mater.* **2012**, *324* (6), 903–915.
- (233) Ueki, T.; Watanabe, M. Upper critical solution temperature behavior of poly (N-isopropylacrylamide) in an ionic liquid and preparation of thermo-sensitive nonvolatile gels. *Chem. Lett.* **2006**, *35* (8), 964–965.

- (234) Schmaljohann, D. Thermo-and pH-responsive polymers in drug delivery. *Adv. Drug Deliv. Rev.* **2006**, *58* (15), 1655–1670.
- (235) Wei, H.; Cheng, S.-X.; Zhang, X.-Z.; Zhuo, R.-X. Thermo-sensitive polymeric micelles based on poly (N-isopropylacrylamide) as drug carriers. *Prog. Polym. Sci.* **2009**, *34* (9), 893–910.
- (236) Liu, C.; Guo, J.; Yang, W.; Hu, J.; Wang, C.; Fu, S. Magnetic mesoporous silica microspheres with thermo-sensitive polymer shell for controlled drug release. *J. Mater. Chem.* **2009**, *19* (27), 4764–4770.
- (237) Lutz, J.-F.; Akdemir, Ö.; Hoth, A. Point by point comparison of two thermosensitive polymers exhibiting a similar LCST: is the age of poly (NIPAM) over? *J. Am. Chem. Soc.* **2006**, *128* (40), 13046–13047.
- (238) Baker, W. O. Microgel, A New Macromolecule. *Ind. Eng. Chem.* **1949**, *41* (3), 511–520 DOI: 10.1021/ie50471a016.
- (239) Staudinger, H.; Husemann, E. Über hochpolymere Verbindungen, 116. Mitteil.: Über das begrenzt quellbare Poly-styrol. *Berichte Dtsch. Chem. Ges. B Ser.* **1935**, *68* (8), 1618–1634 DOI: 10.1002/cber.19350680841.
- (240) Heskins, M.; Guillet, J. E. Solution Properties of Poly(N-isopropylacrylamide). *J. Macromol. Sci. Part - Chem.* **1968**, *2* (8), 1441–1455 DOI: 10.1080/10601326808051910.
- (241) Guan, Y.; Zhang, Y. PNIPAM microgels for biomedical applications: from dispersed particles to 3D assemblies. *Soft Matter* **2011**, *7* (14), 6375–6384.
- (242) Schmidt, S.; Motschmann, H.; Hellweg, T.; von Klitzing, R. Thermoresponsive surfaces by spin-coating of PNIPAM-co-PAA microgels: A combined AFM and ellipsometry study. *Polymer* **2008**, *49* (3), 749–756.
- (243) Rubio-Retama, J.; Zafeiropoulos, N. E.; Serafinelli, C.; Rojas-Reyna, R.; Voit, B.; Lopez Cabarcos, E.; Stamm, M. Synthesis and characterization of thermosensitive PNIPAM microgels covered with superparamagnetic γ -Fe₂O₃ nanoparticles. *Langmuir* **2007**, *23* (20), 10280–10285.
- (244) Karg, M.; Pastoriza-Santos, I.; Liz-Marzán, L. M.; Hellweg, T. A versatile approach for the preparation of thermosensitive PNIPAM core-shell microgels with nanoparticle cores. *ChemPhysChem* **2006**, *7* (11), 2298–2301.
- (245) Zhu, X.; Yan, C.; Winnik, F. M.; Leckband, D. End-grafted low-molecular-weight PNIPAM does not collapse above the LCST. *Langmuir* **2007**, *23* (1), 162–169.
- (246) Pelton, R. Poly (N-isopropylacrylamide)(PNIPAM) is never hydrophobic. *J. Colloid Interface Sci.* **2010**, *348* (2), 673–674.

- (247) Zhang, Y.; Furyk, S.; Bergbreiter, D. E.; Cremer, P. S. Specific ion effects on the water solubility of macromolecules: PNIPAM and the Hofmeister series. *J. Am. Chem. Soc.* **2005**, *127* (41), 14505–14510.
- (248) Lele, A. K.; Karode, S. K.; Badiger, M. V.; Mashelkar, R. A. Prediction of re-entrant swelling behavior of poly (N-isopropyl acrylamide) gel in a mixture of ethanol–water using lattice fluid hydrogen bond theory. *J. Chem. Phys.* **1997**, *107* (6), 2142–2148.
- (249) Lele, A. K.; Devotta, I.; Mashelkar, R. A. Predictions of thermoreversible volume phase transitions in copolymer gels by lattice-fluid-hydrogen-bond theory. *J. Chem. Phys.* **1997**, *106* (11), 4768–4772.
- (250) Lele, A. K.; Karode, S. K.; Badiger, M. V.; Mashelkar, R. A. Prediction of re-entrant swelling behavior of poly (N-isopropyl acrylamide) gel in a mixture of ethanol–water using lattice fluid hydrogen bond theory. *J. Chem. Phys.* **1997**, *107* (6), 2142–2148.
- (251) Badiger, M. V.; Lele, A. K.; Bhalerao, V. S.; Varghese, S.; Mashelkar, R. A. Molecular tailoring of thermoreversible copolymer gels: Some new mechanistic insights. *J. Chem. Phys.* **1998**, *109* (3), 1175–1184.
- (252) Winnik, F. M.; Ringsdorf, H.; Venzmer, J. Methanol-water as a co-nonsolvent system for poly(N-isopropylacrylamide). *Macromolecules* **1990**, *23* (8), 2415–2416 DOI: 10.1021/ma00210a048.
- (253) Pelton, R. H.; Chibante, P. Preparation of aqueous latices with N-isopropylacrylamide. *Colloids Surf.* **1986**, *20* (3), 247–256 DOI: 10.1016/0166-6622(86)80274-8.
- (254) Shimizu, H.; Wada, R.; Okabe, M. Preparation and Characterization of Micrometer-Sized Poly(N-isopropylacrylamide) Hydrogel Particles. *Polym J* **2009**, *41* (9), 771–777.
- (255) Clarke, J.; Vincent, B. Stability of non-aqueous microgel dispersions in the presence of free polymer. *J. Chem. Soc. Faraday Trans. 1 Phys. Chem. Condens. Phases* **1981**, *77* (8), 1831–1843 DOI: 10.1039/F19817701831.
- (256) Saunders, B. R.; Vincent, B. Microgel particles as model colloids: theory, properties and applications. *Adv. Colloid Interface Sci.* **1999**, *80* (1), 1–25.
- (257) Frank, M.; Burchard, W. Microgels by intramolecular crosslinking of poly(allylamine) single chains. *Makromol. Chem. Rapid Commun.* **1991**, *12* (11), 645–652 DOI: 10.1002/marc.1991.030121107.

- (258) Neyret, S.; Vincent, B. The properties of polyampholyte microgel particles prepared by microemulsion polymerization. *Polymer* **1997**, *38* (25), 6129–6134 DOI: 10.1016/S0032-3861(97)00173-0.
- (259) Yamak, H. B. *Emulsion Polymerization: Effects of Polymerization Variables on the Properties of Vinyl Acetate Based Emulsion Polymers*; INTECH Open Access Publisher, 2013.
- (260) Saunders, B. R.; Vincent, B. Osmotic de-swelling of polystyrene microgel particles. *Colloid Polym. Sci.* **1997**, *275* (1), 9–17 DOI: 10.1007/s003960050047.
- (261) Shahbazi-Gahrouei, D.; Ghasemian, Z.; Abdolahi, M.; Manouchehri, S.; haghjooy Javanmard, S.; Dana, N. In vitro evaluation of cobalt-zinc ferrite nanoparticles coated with DMSA on human prostate cancer cells. *J. Mol. Biomark. Diagn.* **2013**, *2013*.
- (262) White, L. D.; Tripp, C. P. Reaction of (3-Aminopropyl)dimethylethoxysilane with Amine Catalysts on Silica Surfaces. *J. Colloid Interface Sci.* **2000**, *232* (2), 400–407 DOI: 10.1006/jcis.2000.7224.
- (263) Eyiler, E.; Walters, K. B. Magnetic iron oxide nanoparticles grafted with poly (itaconic acid)-block-poly (N-isopropylacrylamide). *Colloids Surf. Physicochem. Eng. Asp.* **2014**, *444*, 321–325.
- (264) Nestorovich, E. M.; Karginov, V. A.; Bezrukov, S. M. Polymer partitioning and ion selectivity suggest asymmetrical shape for the membrane pore formed by epsilon toxin. *Biophys. J.* **2010**, *99* (3), 782–789.
- (265) Weir, M. P.; Parnell, A. J. Water Soluble Responsive Polymer Brushes. *Polymers* **2011**, *3* (4), 2107 DOI: 10.3390/polym3042107.
- (266) Uhlmann, P.; Merlitz, H.; Sommer, J.-U.; Stamm, M. Polymer Brushes for Surface Tuning. *Macromol. Rapid Commun.* **2009**, *30* (9–10), 732–740 DOI: 10.1002/marc.200900113.
- (267) Sheparovych, R.; Motornov, M.; Minko, S. Adapting Low-Adhesive Thin Films from Mixed Polymer Brushes. *Langmuir* **2008**, *24* (24), 13828–13832 DOI: 10.1021/la803117y.
- (268) Luzinov, I.; Minko, S.; Tsukruk, V. V. Responsive brush layers: from tailored gradients to reversibly assembled nanoparticles. *Soft Matter* **2008**, *4* (4), 714–725 DOI: 10.1039/B718999K.
- (269) Ayres, N. Polymer brushes: Applications in biomaterials and nanotechnology. *Polym Chem* **2010**, *1* (6), 769–777 DOI: 10.1039/B9PY00246D.

- (270) Mateescu, A.; Wang, Y.; Dostalek, J.; Jonas, U. Thin Hydrogel Films for Optical Biosensor Applications. *Membranes* **2012**, *2* (1), 40 DOI: 10.3390/membranes2010040.
- (271) Tokarev, I.; Minko, S. Multiresponsive, Hierarchically Structured Membranes: New, Challenging, Biomimetic Materials for Biosensors, Controlled Release, Biochemical Gates, and Nanoreactors. *Adv. Mater.* **2009**, *21* (2), 241–247 DOI: 10.1002/adma.200801408.
- (272) Galaev, I. Y. “Smart” polymers in biotechnology and medicine. *Russ. Chem. Rev.* **1995**, *64* (5), 471.
- (273) Chen, T.; Chang, D. P.; Jordan, R.; Zauscher, S. Colloidal lithography for fabricating patterned polymer-brush microstructures. *Beilstein J. Nanotechnol.* **2012**, *3*, 397–403 DOI: 10.3762/bjnano.3.46.
- (274) Matyjaszewski, K.; Spanswick, J. Controlled/living radical polymerization. *Mater. Today* **2005**, *8* (3), 26–33 DOI: 10.1016/S1369-7021(05)00745-5.
- (275) Motornov, M.; Tam, T. K.; Pita, M.; Tokarev, I.; Katz, E.; Minko, S. Switchable selectivity for gating ion transport with mixed polyelectrolyte brushes: approaching “smart” drug delivery systems. *Nanotechnology* **2009**, *20* (43), 434006.
- (276) Bawa, P.; Pillay, V.; Choonara, Y. E.; Toit, L. C. du. Stimuli-responsive polymers and their applications in drug delivery. *Biomed. Mater.* **2009**, *4* (2), 22001.
- (277) Karimi, M.; Zangabad, P. S.; Ghasemi, A.; Hamblin, M. R. Dual/multi-stimuli-sensitive nanocarriers. In *Smart Internal Stimulus-Responsive Nanocarriers for Drug and Gene Delivery*; 2053-2571; Morgan & Claypool Publishers, 2015; pp 6-1-23.
- (278) Poizot, P.; Laruelle, S.; Grugeon, S.; Dupont, L.; Tarascon, J.-M. Nano-sized transition-metal oxides as negative-electrode materials for lithium-ion batteries. *Nature* **2000**, *407* (6803), 496–499 DOI: 10.1038/35035045.
- (279) Tari, A.; Chantrell, R. W.; Charles, S. W.; Popplewell, J. The magnetic properties and stability of a ferrofluid containing Fe₃O₄ particles. *Phys. BC* **1979**, *97* (1), 57–64 DOI: 10.1016/0378-4363(79)90007-X.
- (280) Klouda, L.; Mikos, A. G. Thermoresponsive hydrogels in biomedical applications - a review. *Eur. J. Pharm. Biopharm. Off. J. Arbeitsgemeinschaft Pharm. Verfahrenstechnik EV* **2008**, *68* (1), 34–45 DOI: 10.1016/j.ejpb.2007.02.025.

- (281) Shen, M.; Cai, H.; Wang, X.; Cao, X.; Li, K.; Wang, S. H.; Guo, R.; Zheng, L.; Zhang, G.; Shi, X. Facile one-pot preparation, surface functionalization, and toxicity assay of. *Nanotechnology* **2012**, *23* (10), 105601 DOI: 10.1088/0957-4484/23/10/105601.
- (282) Pelton, R. Poly(N-isopropylacrylamide) (PNIPAM) is never hydrophobic. *J. Colloid Interface Sci.* **2010**, *348* (2), 673–674 DOI: 10.1016/j.jcis.2010.05.034.
- (283) MARVEL, C. S.; SHEPHERD, T. H. Polymerization Reactions of Itaconic Acid and Some of Its Derivatives. *J. Org. Chem.* **1959**, *24* (5), 599–605 DOI: 10.1021/jo01087a006.
- (284) Willke, T.; Vorlop, K.-D. Biotechnological production of itaconic acid. *Appl. Microbiol. Biotechnol.* *56* (3), 289–295 DOI: 10.1007/s002530100685.
- (285) Miura, Y.; Satoh, K.; Kamigaito, M.; Okamoto, Y. Well-Defined Graft Copolymers of Methacrylate, Acrylate, and Styrene via Ruthenium-Catalyzed Living Radical Polymerization. *Polym J* **2006**, *38* (9), 930–939.
- (286) Liu, P.; Guo, J. Polyacrylamide grafted attapulgite (PAM-ATP) via surface-initiated atom transfer radical polymerization (SI-ATRP) for removal of Hg(II) ion and dyes. *Collect. Pap. Honor Profr. Ivan B Ivanov Lab. Chem. Phys. Eng. Univ. Sofia Celebr. His Contrib. Colloid Surf. Sci. Occas. His 70th Birthd.* **2006**, 282–283, 498–503 DOI: 10.1016/j.colsurfa.2006.02.052.
- (287) Liu, P.; Su, Z. Surface-initiated atom transfer radical polymerization (SI-ATRP) of styrene from chitosan particles. *Mater. Lett.* **2006**, *60* (9–10), 1137–1139 DOI: 10.1016/j.matlet.2005.10.094.
- (288) Liu, Y.-L.; Chen, S.-C.; Liu, C.-S. Surface grafting of polyimide onto silicon surface: Preparation and characterization. *J. Polym. Sci. Part Polym. Chem.* **2007**, *45* (17), 4161–4167 DOI: 10.1002/pola.22255.
- (289) Eyiler, E.; Walters, K. B. Magnetic iron oxide nanoparticles grafted with poly (itaconic acid)-block-poly (N-isopropylacrylamide). *Colloids Surf. Physicochem. Eng. Asp.* **2014**, *444*, 321–325.
- (290) Barrera, C.; Herrera, A.; Zayas, Y.; Rinaldi, C. Surface modification of magnetite nanoparticles for biomedical applications. *J. Magn. Magn. Mater.* **2009**, *321* (10), 1397–1399.
- (291) Huang, Y.-F.; Wang, Y.-F.; Yan, X.-P. Amine-functionalized magnetic nanoparticles for rapid capture and removal of bacterial pathogens. *Environ. Sci. Technol.* **2010**, *44* (20), 7908–7913.

- (292) Dave, S. R.; Gao, X. Monodisperse magnetic nanoparticles for biodetection, imaging, and drug delivery: a versatile and evolving technology. *Wiley Interdiscip. Rev. Nanomed. Nanobiotechnol.* **2009**, *1* (6), 583–609.
- (293) Wu, W.; He, Q.; Jiang, C. Magnetic iron oxide nanoparticles: synthesis and surface functionalization strategies. *ChemInform* **2009**, *40* (24), i.
- (294) Dutz, S.; Clement, J. H.; Eberbeck, D.; Gelbrich, T.; Hergt, R.; Müller, R.; Wotschadlo, J.; Zeisberger, M. Ferrofluids of magnetic multicore nanoparticles for biomedical applications. *J. Magn. Magn. Mater.* **2009**, *321* (10), 1501–1504.
- (295) Wu, W.; Shen, J.; Banerjee, P.; Zhou, S. Chitosan-based responsive hybrid nanogels for integration of optical pH-sensing, tumor cell imaging and controlled drug delivery. *Biomaterials* **2010**, *31* (32), 8371–8381.
- (296) Roig, A.; Taboada, E.; Rodríguez, E. High transversal relaxivities of silica coated multicore iron oxide nanoparticles suitable for magnetic resonance imaging. In *MRS Proceedings*; Cambridge Univ Press, 2010; Vol. 1257, pp 1257-O05-6.
- (297) Dutz, S.; Kettering, M.; Hilger, I.; Müller, R.; Zeisberger, M. Magnetic multicore nanoparticles for hyperthermia—influence of particle immobilization in tumour tissue on magnetic properties. *Nanotechnology* **2011**, *22* (26), 265102.
- (298) Yoon, T.-J.; Lee, H.; Shao, H.; Hilderbrand, S. A.; Weissleder, R. Multicore assemblies potentiate magnetic properties of biomagnetic nanoparticles. *Adv. Mater.* **2011**, *23* (41), 4793–4797.
- (299) Bustamante, R.; Millán, A.; Piñol, R.; Palacio, F.; Carrey, J.; Respaud, M.; Fernandez-Pacheco, R.; Silva, N. J. O. Influence of structural and magnetic properties in the heating performance of multicore bioferrofluids. *Phys. Rev. B* **2013**, *88* (18), 184406.

APPENDIX A

PROCEDURE AND METHODS UTILIZED FOR CHARACTERIZATION

A.1 MIRacle-ATR FTIR procedure

On a Thermo Electron corporation Nicolet 6700 FT-IR with a helium-neon laser, a mercury-cadmium-telluride (MCT) detector or a deuterated triglycine sulfate (DTGS) detector, a MIRacle-ATR (Pike Technologies) with ZnSe/diamond crystal using Omnic 8.1.10 software (copyright 1992-2009, Thermo Fisher Scientific Inc.).

A.1.1 Clearing water from drip leg

1. Ensure the wash sink is clear of glassware.
2. Get ear plugs for everyone in the lab
3. Go the yellow handle valve above the GPC that is on the main compressed airline for the lab.
4. Close the yellow handle valve.
5. Slowly open on the red handle valve directly below it.
6. Compressed air, with any water that had pooled in the drip leg, will now flow into the wash sink.
7. When the compressed air shows no indication of water, close off the red handled valve and open on the yellow handled valve.

A.1.2 Filling liquid nitrogen dewar on MCT detector

1. On the left side of the instrument, open the front most circular lid above where the detectors are located in the instrument.
2. Remove the black plug.

3. Put in the funnel with a metal stem and expanded polystyrene spacer gently into where the black plug was located.
4. Carefully pour a small amount of liquid nitrogen into the funnel and allow the funnel and dewar to cool for 2 min.
5. Gently pour liquid nitrogen into the dewar until it over flows.
6. Let the funnel warm up while in the dewar to avoid breaking it when taking it out.
7. Remove the funnel, and carefully replace black plug.
8. Gently replace lid to original position, but do not push down on the lid until the rubber gasket has come to room temperature.
9. Once rubber gasket is up to room temperature, press lid into place.

A.1.3 MIRacle-attenuated total reflectance - FTIR

1. Put the MIRacle-ATR accessory into the accessory bay on the FTIR with the removable flanges on the instrument in place where the IR beam enters and exits the sample chamber.
2. Plug in the purge line for the accessory into the back of the sample compartment.
3. Purge the FTIR for at least 20 min.
4. While FTIR purges, open Omnic program on the FTIR computer.
5. Go to collect on the upper menu and experimental setup
6. Click “open” in the experiment setup window to open saved experimental files.

7. If there are no saved experimental files for current sample set, go to the “Collect” tab.
8. Input number of scans, resolution, and set format to absorbance on the left side of the window.
9. In the file handling area of the same window on the upper right side, input your initials and check both “save automatically” and “save interferograms”
10. In the background handling section below file handling area, click on either “Collect background before every sample” or “Collect background after every sample.”
11. Go to bench tab in the experimental setup window.
12. Set “Sample Compartment” to Main
13. Set “Detector” to either “DTGS TEC” or “MCT High D*.”
14. Set “Beam Splitter” to “XT-KBr.”
15. Select appropriate source for your samples under “Source.” The standard choice is “IR.” The “IR - Turbo” should be avoided because it can significantly reduce the He-Ne laser’s life span, the “IR – Rest” is for when the instrument is not in use for extended periods of time, and “White light” is for probing low wavelengths.
16. Set “Accessory” to match the accessory in the accessory compartment.
17. Set the range of wavenumbers to be scanned (usually left at default values).

18. Adjust gain (1 to 8) and aperture (32 to 74) to obtain a signal between 5 and 8. If the signal values cannot be reduced to appropriate levels, put in a physical screen (A-D) on the inside of the left side of the sample chamber where the beam exits the sample chamber.
19. Before taking data, always go to the “Diagnostic” tab in the experimental setup window and click on the “Align” button to maximize signal.
20. Save the experimental file.
21. Close the experimental setup window.
22. Take a background with no sample by hitting “Ctrl + B.”
23. If background has a low concentration of water, save the background by going to file menu and save. The background needs to be retaken every 30 min to 1 hr.
24. Open the experimental setup window again.
25. Go to the collect tab, and under “Background Handling” click “Use specific background file:” and load the previously taken background.
26. Click “Save” and then “Ok.”
27. Gently place solid sample (or droplet of solution and allow solvent to evaporate) onto the crystal.
28. Take the sample spectrum by hitting “Ctrl + S”
29. If the sample has noticeable water interference, at the end of taking the spectrum, click “More Scans” and not “Add to Window” when prompted. If the spectrum is satisfactory, click “Add to Window” when prompted.

A.2 Simultaneous thermogravimetric analysis and differential scanning calorimetry (SDT)

Analysis was performed on a TA Instruments SDT Q600 using Advantage for Q series (Version 2.8.0.394, Thermal Advantage Release 5.1.2, copyright 2001-2009, TA Instruments-Waters LLC) and analysis was performed on TA Instruments Universal Analysis 2000 software for Windows 2000/XP/Vista (version 4.7A, build 4.7.0.2, copyright 1998-2009, TA Instruments-Waters LLC).

1. Open furnace by going to control panel on SDT, press furnace button, set to open, and hit apply.
2. Take two Pt pans and, carefully, put on cantilever balance. The rear pan is a reference and front pan is for the sample.
3. Close the furnace using the SDT control panel.
4. Open Q600 SDT controller by clicking on the Q600 SDT icon in the TA Instrument Explorer window.
5. Tare the weight of the pans by clicking on the tare button that looks like an old fashion counter weight balance button on the top tool bar.
6. Open the furnace using the SDT control panel.
7. Remove the front Pt pan.
8. Put it on the balance and tare the weight.
9. Weigh out ~5 mg of sample into pan.
10. Put the sample Pt pan back onto cantilever balance.
11. Close the furnace.
12. In the middle section, click on the summary tab.

13. Under Procedure Summary, set mode to SDT Standard and Test to Ramp.
14. In Sample Information, enter a sample name, Pan type to PT, enter any additional comments, set the data file name, and check network drive.
15. Go to the Procedure tab.
16. Under method, check Use Current.
17. Set final temperature to 300 °C.
18. Next add Ramp at 5 °C/min.
19. Go to Notes tab
20. Set Mass Flow Control Settings to #1-Nitrogen and a flow rate of 50 mL/min.
21. Click run in the upper left hand corner.

A.3 Modulated differential scanning calorimetry (DSC)

Analysis was performed on a TA Instruments DSC Q2000 using Advantage for Q series (Version 2.8.0.394, Thermal Advantage Release 5.1.2, copyright 2001-2009, TA Instruments-Waters LLC) and analysis was performed on TA Instruments Universal Analysis 2000 software for Windows 2000/XP/Vista (version 4.7A, build 4.7.0.2, copyright 1998-2009, TA Instruments-Waters LLC).

1. Weigh a T-Zero pan and lid.
2. Weigh out 5 mg of sample.
3. Put sample into T-Zero pan and put lid on pan.
4. Put the Black T-Zero cupped die into the upper part of the press.
5. Put the pan with sample and lid into the Black T-Zero lower die.
6. Put die into press.

7. Press the pan to seal pan.
8. Put pan into auto sampler of DSC
9. Open Q2000 DSC controller by clicking on the Q2000 DSC icon in the TA Instrument Explorer window.
10. In the middle section, click on the summary tab.
11. Under Procedure Summary, set mode to Standard and Test to Custom.
12. In Sample Information, enter a sample name, enter the pan number (position in auto sampler), set Pan type to Tzero Aluminum, check pan mass, enter a sample size and pan mass, enter any additional comments, set the data file name, and check network drive.
13. Go to the Procedure tab.
14. Under method, click on editor.
15. Add equilibrate at -90 °C
16. Next add Data storage On.
17. Next add Ramp at 5 °C/min to 220 °C.
18. Finally add Data storage Off.
19. Go to Notes tab
20. Set Mass Flow Control Settings to #1-Nitrogen and a flow rate of 50 mL/min.
21. To add another sample repeat steps 1-8, then append a new run in the left most window, and repeat steps 12 – 18.
22. Click run in the upper left hand corner.

A.4 X-Ray photoelectron spectroscopy (XPS)

This procedure is to be used for PHI 1600 ESCA with Perkin-Elmer dual anode source x-ray source, 04-548, Perkin-Elmer Omni III lens, 72-366S, Perkin-Elmer ion pump, Perkin-Elmer specimen manipulator, 10-325, Perkin-Elmer instrument console, 40-710, Perkin-Elmer dual x-ray source control, 32-096, Perkin-Elmer x-ray supply, 20-040, Perkin-Elmer DGC III digital gauge controller, and Perkin-Elmer spherical capacitor energy analyzer, 10-360, with PHI Surface Analysis Software for windows version 3.0 copyright 1994 Physical electronics Inc.

A.4.1 Sample preparation

1. Sample needs to be put under vacuum for an extended period of time to remove all solvents and volatiles from the sample.
2. If the sample is a polymer film or Si wafer, mount sample on sample puck using copper hold downs.
3. If sample is a powder, compress sample into a small disk and use sample covers to hold sample in place.
4. If sample is too small to use sample covers or hold downs, copper or carbon tape can be use to hold sample in place, but this is not recommended.

A.4.2 Sample loading into XPS main chamber

1. On sample entry chamber, close red and black valves.
2. Open green valve to bring chamber to atmospheric pressure.
3. Remove cover from sample entry chamber.

4. Using puck tongs, place sample puck into sample holder.
5. Replace cover and ensure it is seated properly.
6. Close green valve.
7. Turn on main roughing pump that is connected to the black valve.
8. Open black valve.
9. Using the Varian Multi Gauge on the right side of the XPS, pump the entry chamber to 2×10^{-2} Torr.
10. Once 2×10^{-2} Torr is reached, close black valve and open red valve.
11. Pump down entry chamber to 1×10^{-4} Torr and then wait 1 h.
12. After pumping down entry chamber, open gate valve separating entry chamber and main chamber of the XPS.
13. If main chamber increases above 1×10^{-7} Torr (seen on the Perkin-Elmer Digital Gauge Control III), immediately close gate valve and continue to pump down entry chamber. Otherwise proceed with steps below.
14. Slide the sample over sample hold in main chamber.
15. Align main chamber sample holder using X and Y controls on the right side of XPS main chamber.
16. Raise main chamber sample holder using Z control on the right side of the XPS main chamber.
17. Remove sample holding arm from main chamber by sliding it out.
18. Close gate valve.
19. Allow pressure in main chamber to go below 9×10^{-9} Torr before attempting to turn on X-ray beam.

A.4.3 Starting the X-ray source

If at any time during the following procedure the pressure increases above 5×10^{-8} Torr, the XPS will interlock fault, and the procedure has to be restarted from the beginning.

1. Turn on the heat exchanger on the far right side of the XPS.
2. Turn on the power to the X-ray supply (bottom panel on right side of XPS).
3. Turn on the power to the X-ray source control (top panel on right side of XPS).
4. On the X-ray source control, select source 1 and switch to Int.
5. On the X-ray source control, under filament energize, push Mg button.
6. On the X-ray source control, under parameter display/control, push HV button.
7. Press large, red, high voltage button on X-ray source control panel.
8. On the X-ray supply panel, turn the high voltage control until the parameter display/control on the X-ray source control reads 0.5 kV.
9. Continue increasing voltage by 0.5 kV every 1 to 2 min until 8 kV is reached.
10. Once 8 kV is reached, increase voltage by 0.1 kV every 1 to 2 min until 8.5 kV is reached. At 8.3 kV, the instrument has reached a high enough voltage as to cause instant death if an electrical component is touched.
11. At 8.5 kV, increased voltage by 0.5 kV every 1 to 2 min until 12 kV is reached and stop increasing voltage.

12. On the X-ray source control panel, under parameter display/control, push the Mg button to bring display the current power.
13. Using the up and down arrows under the parameter display/control, increase the power by 1 W every 1 to 2 min until 8 W is achieved and the X-ray source is now active.
14. At 8 W, let the instrument rest for 5 min to allow the X-ray source to achieve equilibrium.
15. After 5 min, increase power by 1 W every 1 to 2 min until 12 W is achieved.
16. Once 12 W is achieved, increase power to 25 W and every 1 to 2 min increase by 25 W until 200 W is achieved.
17. Under parameter display/control on the X-ray source control panel, push the HV button.
18. Increase voltage by 0.5 kV until 15 kV is achieved, and the system is now at maximum working voltage.
19. Under parameter display/control on the X-ray source control panel, push the Mg button.
20. Increase power by 25 W every 1 to 2 min until 300 W is achieved.
21. X-ray source is now at working power and voltage, push the card rack power button the power control panel on the left side of the instrument.
22. Turn on Fostec light (white box on XPS desk).
23. Using the built in 10X microscope, using X, Y, and Z control bring the area of interest on the sample into focus.

24. Open PHI CMA XPS software on the computer.
25. Go to file menu and select dir.
26. Select directory and input a 5 character sample name.
27. Click ok.
28. Go to Acquire on the menu bar and select survey.
29. Specify upper binding energy and range (normally upper binding energy is 1100 eV and range is 1100 eV).
30. Set step size to 0.5 eV, time/step to 10 ms, and 10 repeats.
31. Got Execution on menu bar and select start acquisition.
32. Once data acquisition is complete, got to file menu and save file as ASCII.
33. Go to Acquire on the menu bar and select Multiplex.
34. Add regions such as C1, O1, and Si1 in reference to the chemical elements of interest from survey scan for high resolution scan. Adjust regions range as needed.
35. Set step size to 0.2 eV, time/step to 50 ms, and repeats to 15.
36. Got Execution on menu bar and select start acquisition.
37. Once data acquisition is complete, got to file menu and save file as ASCII.
38. Repeat steps 22-37 for additional spots and samples.
39. To turn off instrument, on the X-ray source control panel, switch Int switch to Ext.
40. Under parameter display/control on the X-ray source control panel, push HV button.

41. On the X-ray supply panel, turn the high voltage control left until 0 kV is read off of X-ray source control.
42. X-ray source is now off; push the card rack power button the power control panel on the left side of the instrument.
43. Turn off the X-ray source control, X-ray supply, and heat exchanger.
44. Open the gate valve between the entry chamber and the main chamber and remove the sample.
45. Using a Fat 16 formatted flash drive, transfer files to flash drive to analyze on CasaXPS.

A.5 Freeze-pump-thaw

1. Fill liquid nitrogen dewar connected to manifold for vacuum.
2. Place a big beaker containing water onto heater for thaw
3. Fill liquid nitrogen dewar completely for freeze.
4. Be careful that the flask is not full more than half of the volume.
5. Immerse the flask into the LN2 dewar to freeze. Allow it to freeze completely.
6. Take it out and open the stopcock to pump it out.
7. Close the stopcock, and immerse the flask into water bath to thaw.
8. Check for the gas bubbles coming out.

Repeat steps (5) – (7) as needed. A minimum of three cycles

A.6 Differential scanning calorimetry (DSC)

A TA Instruments Q-2000 modulated DSC (mDSC) was used for thermal analysis of PLA and PLA/PTM blend films with the TA Universal Analysis 2000 software (v4.7A). The blend film samples weighing 5 mg were first heated from 40 to 200 °C at a rate of 10 °C/min, and then held for 5 min to eliminate the thermal history. Subsequently, they were cooled to - 50 °C, and heated again from - 90 °C to 200 °C at a rate of 10 °C/min under 50 mL/min of nitrogen purge.

A.7 Procedure to run *in-situ* AFM measurements

A.7.1 Summary

This Experimental plan summarizes different steps that need to be followed using scanasyst mode in Dimension Icon AFM equipment as depicted in Figure A.1. Tips that are used for this experiment are: Scanasyst-fluid made of nitride tip and nitride lever. The cantilever has a T: 05-0.7 micrometer. And the frequency varies from 120-180 Khz. K: 0.7 N/m.

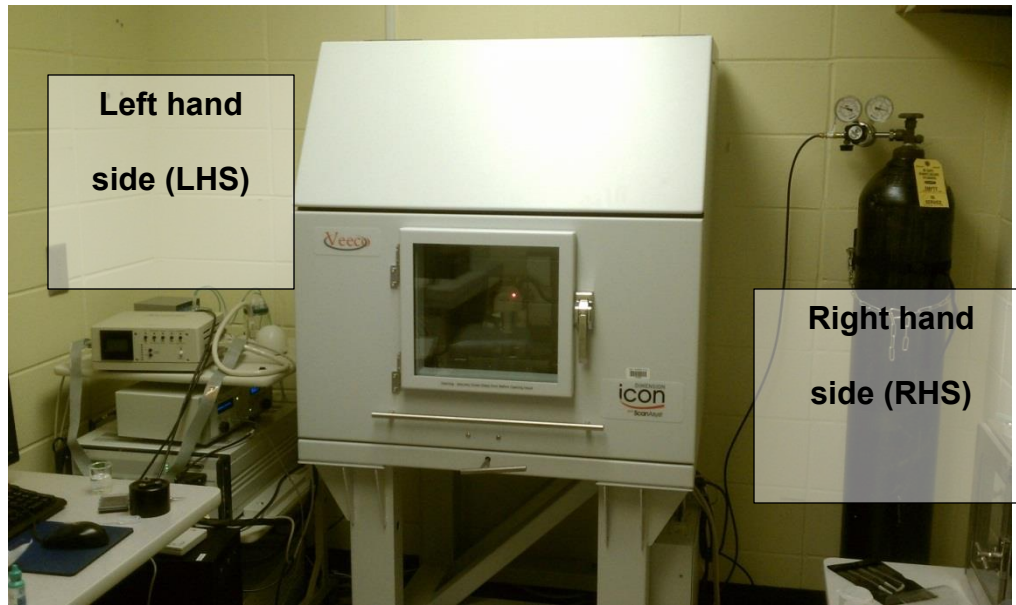


Figure A.1 AFM Icon instrument front view

A.7.1.1 Procedure

A.7.1.1.1 Equipment startup

Turn on the computer and monitor for the Dimension Icon Equipment
Hit Ctrl+Alt+Del as it prompts on the monitor and introduce the password for the
computer: emcenter

Connect the heater/cooler cable on the right hand side of the ICON instrument:
Turn on the equipment (using power strip on the left hand side of the instrument) and turn
on the heater/cooler accessory. Note the turn on/off button is at the left on the back of this
panel

A.7.1.1.2 Experimental setup

1. Use the fluid cell cantilever holder located in the cabinet on top of the
computer.

2. Place the cantilever holder on the special setup (the one that has a spring)
3. Then, place one of the scanasyst-fluid tips on the cantilever as the spring lift the small wire/clamp to hold in place the tip.
4. The tip can be seen using the optical microscope in the adjacent lab.
5. Check that the cantilever is not tilted or not vertically positioned with respect to the gray clamp. By experience, if the cantilever is a barely tilted, beam alignment will be complicated and/or unsuccessful.
6. Open Nanoscope v.8.15.
7. Initialize the equipment
8. Select New experiment: Scanasyst in fluid and change the microscope setup to H/C Temperature.
9. Hit OK
10. Place the cantilever holder with the tip on the Bruker scanning head
11. Place the Teflon gasket at the bottom of the cantilever holder. This is used to protect the scanning head from any spill that might occur as the scanning in liquid takes place. **Be Careful!. When setting up the plastic sleeve/gasket as it might damage your tip.**
12. Go to setup and align the beam on the tip by:
13. Adjusting the laser intensity on the tip. Multiple reflections are observed on this particular cantilever/tip holder. Thus, location of the real beam must be performed to obtain a good result. First locate the laser on the screen by moving the **top-screws** on the scanning head until you see the beam on the computer screen as shown below (Figure A.2).

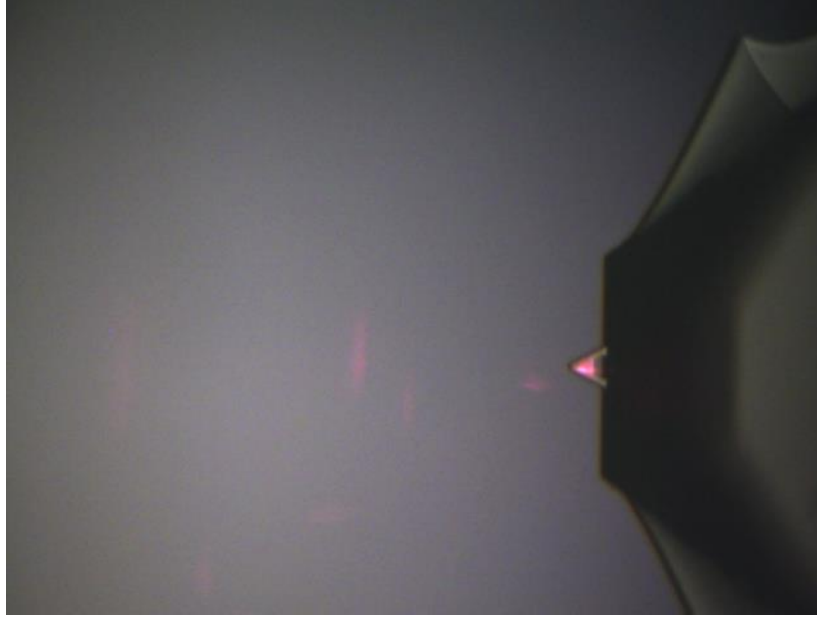


Figure A.2 Beam alignment while *in-situ* measurements are conducted

14. Adjust the side buttons of the scanning head, until the maximum intensity is obtained for the particular tip.
15. Typical values for intensity varies:
 - No liquid: $\sim 2.1 - 2.5$ V
 - Liquid: 3.1- 3.5 Va
16. Place your wafer on one magnetic holder (utilized for this particular samples). Use copper tape to guarantee no movement and to be able to release the wafer after you are done with the experiment. If you use double side tape or any other tape most likely the wafer won't be able to come out of the surface and your sample will be unusable if it breaks.

17. Place the wafer on the magnetic holder. Then add a drop of water (or the liquid you are trying to use on top of the wafer)
18. After correctly aligning the tip on the scanning head. Carefully, add 1-2 microdrops on the tip (This is extremely difficult and be aware/cautious of the laser).
19. Align the vertical position and red cross for the displacement due to the water refraction effect on the tip
20. Go to navigate and start lowering the scanning head until you see both drops (the one in the scanning head and the other one on the wafer) start coming closer. Reduce the speed to about 20%, then the two drops will crash and eventually the software will “suppose” that there is a misalignment.
21. Realign the tip with the laser. Also, make sure to “check” the box that says, alignment was performed on the fluid.
22. Go back to setup and check that the maximum intensity was reached
23. Go to navigate and detect a spot that you wish to scan by moving the side and top arrows on the computer screen.
24. Once you locate a spot, check your parameters. Mainly, scanning size and scans per line. It is suggested to use 512 scans/line. Additionally, at the beginning a very large area (15 -10 microns) should be scanned to setup a particular point , then you can move easily around your sample and/or point of interest.

25. Check parameters once again, and make sure that the maximum intensity has not changed. Go to scan and select the following screens:
Height sensor
peakforce error
inphase
quadrature
26. NOTE: This must be done before starting your scan. Otherwise, data will not be collected/saved.
27. Select the directory that you want to save your data by clicking on the folder with the camera on the rhs of the screen.
28. After selecting your folder, you can go to it by clicking on the small camera beside the directory on the top rhs of the screen
29. Type the name of your sample and hit enter
30. Hit engage
31. Wait until the sample data is starting to collect and hit the bottom arrow to start scanning from the top to the bottom
32. Select capture now for the image to save automatically
33. If by any reason your image is not saved. Stop the capture now and hit Capture last. This should save your file.
34. After the image has been collected click withdraw. Go back to the navigate button and select a new point of interest for your scan.
35. Once you are finished. Withdraw once again. Adjust the lifting speed to 20 % and slowly remove the tip from the water/liquid drop. The signal

- intensity should have decreased dramatically as the tip comes out of contact with the water. Here, try to realign to be able to move the stage.
36. Once realigned, move the sample stage to the front. Dry the drop that is located on your sample with a kimwipe, and remove/store the sample.
 37. Remove the scanning head (Be Careful with the laser). Now, remove the plastic gasket (Careful as it might break your tip). Then, remove the tip holder and place it on the special support. Place back the scanning head on the equipment. Use a kimwipe to dry any liquid. If a liquid different than water was used, make sure to use a couple of drops of water to clean the tip. Dry on a side with kimwipes. This can be done in the optical microscope in the adjacent lab.
 38. Once the tip has been cleaned, remove it with the tweezers and store in the box.
 39. Clean and dry the fluid cell cantilever holder and store it back in the bag and put it in the drawer located on top of the computer.
 40. Turn off the heater and go to the software and remove the heater/cooler H/C option.
 41. Turn off the equipment using the power strip on the LHS of the instrument
 42. Turn off the computer